

©2020 Peter Amos York

All rights reserved.

Dissertation Advisor:

Professor Robert J. Wood

Author:

Peter Amos York

Millimeter-scale robotics: fabrication, actuation, and medical devices

Abstract

Opportunities lie on the millimeter scale to develop robotic surgical tools that achieve greater access and give surgeons greater control deep inside the human body. The key challenge is that standard approaches to fabrication and motion generation do not scale well to the millimeter-scale. In my dissertation, I describe several projects that aim to fill this gap through the development of new fabrication, actuation, and design techniques: (1) a centimeter-scale surgical laser steering tool; (2) a millimeter-scale surgical laser steering tool; (3) a new method for fabricating nitinol living hinges; and (4) high-performance millimeter-sized piezoelectric flextensional actuators. These efforts draw from a common set of laminate-based manufacturing and laser micromachining techniques and are additionally cohered around the theme of millimeter-scale motion generation and control.

Contents

Title Page	i
Abstract	iii
Table of Contents	iv
Acknowledgments	vi
1 Introduction	1
2 Millimeter-scale Fabrication: Printed-circuit MEMs	8
2.1 Core tools	8
2.2 Materials	11
2.3 Design practices	13
2.4 Innovations	14
3 Nitinol Living Hinges	16
3.1 Introduction	16
3.2 Manufacturing	20
3.3 Modeling	21
3.4 Characterization	24
3.5 Prototype Devices	26
3.6 Discussion	27
3.7 Conclusion	29
4 Piezoelectric Flextensional Actuators	30
4.1 Introduction	30
4.2 Background	31
4.2.1 Displacement amplification techniques for piezoelectric actuators . .	31
4.2.2 Flextensional piezoelectric actuators	33
4.2.3 Applications	34
4.3 Gen I: FR4 Actuators	35
4.3.1 Composition	36
4.3.2 Fabrication	36
4.3.3 Design	39
4.4 Gen II: Carbon fiber actuators	45
4.4.1 Composition	45

4.4.2	Fabrication	46
4.4.3	Lumped parameter modeling	49
4.4.4	Finite element modeling	52
4.4.5	Design study	53
4.4.6	Results	56
4.4.7	Discussion	60
4.4.8	Summary	62
4.5	Gen III-V: Alumina-reinforced carbon fiber actuators	62
4.5.1	Composition	62
4.5.2	Fabrication	67
4.5.3	Modeling	71
4.5.4	Scaling analysis and design guideline derivation	76
4.5.5	Results	79
4.5.6	Discussion	81
4.6	Summary	84
5	Robotic Laser Steering: Centimeter-scale Device	86
5.1	Introduction	86
5.2	Clinical background: vocal fold surgery	87
5.3	State of the art	89
5.4	System concept	92
5.5	Modeling	92
5.6	Results	95
5.7	Discussion	97
6	Robotic Laser Steering: Millimeter-scale Device	98
6.1	Introduction	98
6.2	Results	99
6.3	Design	104
6.4	Fabrication	108
6.5	Hysteresis compensation	110
6.6	Experimental setup and procedures	115
6.7	Discussion	116
7	Conclusion	120
	Bibliography	121

Acknowledgments

It is a distinct joy to consider the many people who have assisted me in the production of this research, and, more broadly, in my educational journey. In roughly chronological order:

Janet, my wife, for her partnership with me in our PhD work and especially in these days of writing in quarantine.

Robert Wood, my dissertation advisor, for his steady, patient guidance and support throughout this work, and Robert Howe and Joost Vlassak, for their feedback and critique as members of my dissertation committee.

Noah Jafferis, for the accumulated wisdom he has shared with me over the years. Noah pushes the limits of what is possible with microrobotic systems and in doing so has inspired me to do the same. I have also gained much from his no-fuss approach to modeling and experiments. In all, I am very grateful to have Noah as an example, and his influence can be seen throughout this work, second only to Rob's in importance. Farrell Helbling, for her steady presence and friendship throughout the PhD experience. The many other Microrobotics Lab members, too numerous to each name, whose friendship and camaraderie have been invaluable to me. I do particularly think of the foosball and volleyball players.

Simon Bothner, Phillip Song, and Noah, collaborators who have expanded my view and contributed to the ideas described herein. Tom Hayes and David Abrams, who gave me a chance to teach Physics 123 and showed me different but effective ways to engage and communicate with students. James Harper and Kunle Adeyemo, whose perspective at the beginning of this work was much needed for calibrating my expectations. Leif Jentoft and Aaron Silva, whose friendship and care helped orient me in my first year in Cambridge.

Hunter Gilbert, Rich Hendricks, and Philip Swaney, who in my mind set the standard for what engineering graduate students ought to be: hard-working, curious, thoughtful, and kind. I am particularly grateful to Phil for investing in me when I was an undergradu-

Acknowledgments

ate. Robert Webster, my undergraduate research advisor, for giving me the chance to work in his lab and learn so much from him and his graduate students. My other undergraduate professors, especially Nabil Simaan, Eric Barth, and Tom Withrow. My undergraduate colleagues who pushed me to improve and opened my eyes to new knowledge; I think particularly of Dylan Losey, Eric Bramlett, and Jonathan Aldrich.

My family, who has supported and encouraged me in these educational endeavors, in deep and lasting ways, from my grandparents Carl, Clara, Peter, and Ann, to my parents Mark and Carol, to my siblings Elizabeth and David. Their love and support is of incalculable worth.

Last, I thank my Creator, who has blessed me beyond measure with the opportunity to learn and contribute to human knowledge and achievement in some small way through this work.

Chapter 1

Introduction

This thesis considers the confluence of three phenomena at the 1 to 10 mm scale: fabrication of mechanical components, actuation physics, and useful applications. It is in this dimensional range that standard approaches for each of these factors become murky, and their confluence triply so. Allow me to explain:

First, the creation and assembly of mechanical components on the 1 to 10 mm scale is a surprisingly challenging proposition. Typical processes for larger components such as milling, lathing, and drilling do not scale down well to the millimeter scale. The forces imparted in those processes are difficult to manage, both in terms of fixturing and in the cutting tools themselves. Feature size is limited by the size of the cutting tool, which is limited by the forces it can withstand before failure. On the much nano and micro scales, techniques such as photolithography, chemical etching, and vapor deposition achieve the precise, complex geometries found in micro-electromechanical systems (MEMs). These, however, are limited in the types of materials that can be used and the topologies that can be achieved.

Second, not only are the types of actuators used most frequently in larger scale

systems — fluidic pistons, AC and DC electromagnetic motors, combustion engines, etc — difficult to manufacture on the millimeter scale due to their complexity, they also are fundamentally limited by insidious scaling of forces. Specifically, as size decreases, the dissipative effect of friction comes to dominate the generative effects of standard actuation methods. This leads the engineer to seek out actuation sources that at least scale in the same way as friction, if not more favorably.

Third, it is not initially clear what is worth doing using robotic systems on the millimeter scale. If we allow that robotic systems are used for interacting with matter, then the question might be reframed as: what millimetric matter is worth interacting with? Once again, on the micron scale and smaller we care about manipulating cells, silicon chips, DNA, and the like, and on the centimeter scale and larger there is the entire human-scale world to interact with. In contrast, humans don't normally care about the millimeter. However, we do care when that millimeter is the difference between a successful surgery and hitting a nerve, or between removing a throat nodule to restore vocal function and damaging the vocal folds to impair vocalization permanently. Millimeters matter to surgical outcomes, and they also matter in the size of tools— the smaller that tools can be made, the more useful they become in terms of the confined spaces they can navigate and the access deep inside the body they can achieve. That is a long-winded way of saying that building millimeter-sized robots to assist with medical procedures is a worthwhile endeavor.

Hopefully the overlap between these themes is apparent: building millimeter-sized robotic surgical tools is made challenging by the difficulty of finding appropriate actuation physics and that of building and assembling complex devices. It is exactly at this intersection that my interests, and this dissertation, lies. This intersection is illustrated graphically in the concept figure below Figure 1.1. The introduction will proceed by examining each of these themes in more detail and describing how progress can be made:

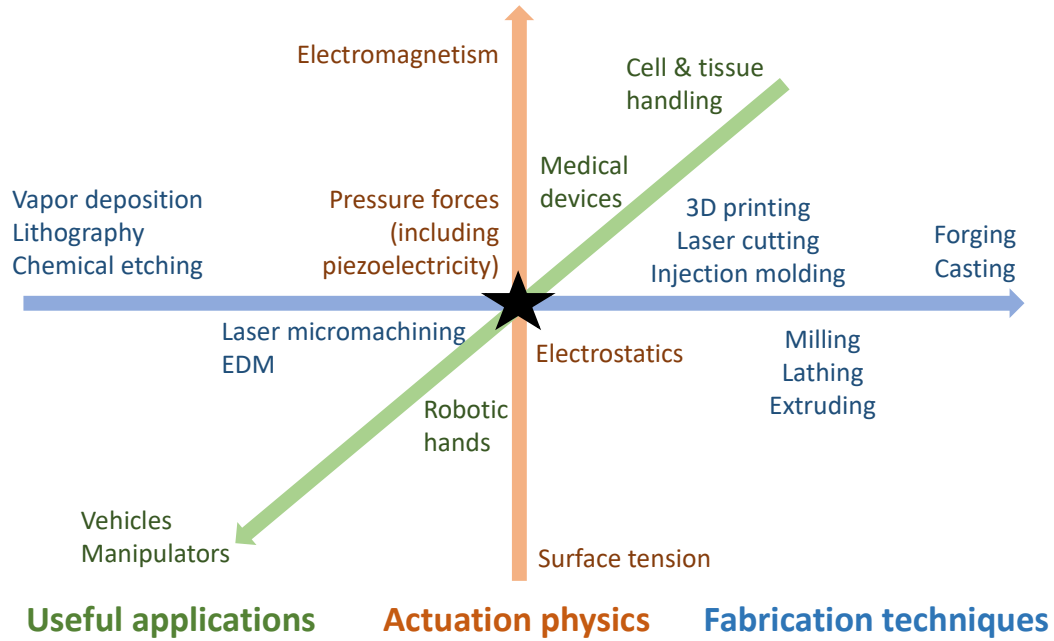


Figure 1.1: Three phenomena represented as functions of length scale: applications for robotic tools, actuation physics, and fabrication techniques. This thesis lies at the intersection of these factors on the 1 to 10 mm scale.

Fabrication With the challenges of millimeter-scale fabrication and assembly in context, a new suite of manufacturing tools has recently been developed that blends manufacturing methods from macroscopic techniques and silicon-based microfabrication, as well as integrating methods from printed-circuit board fabrication. These techniques, variously called “Pop-up MEMS” or “Printed circuit board MEMs” (PC-MEMs) concede that the fabrication of fully 3D millimeter-scale components is very difficult, so they refocus on so-called 2.5D components that begin flat and are assembled in pop-up book fashion into 3D structures. This remedies many problems. Repeatable assembly and joining of different components is very difficult in three dimensions, requiring the use of custom-fabricated assembly jigs. Two-dimensional assembly is comparably simple, because lamination, akin to the lamination of printed circuit boards, can be used. Lamination allows for the creation

of precisely placed, strong bonds between different components through the use of heat-curable adhesives and lamination. Another benefit of restricting the fabrication space to 2.5D structures is that 2D structures are trivially fixtured during subtractive machining. These techniques were developed by many researchers, particularly at UC Berkeley and at Harvard, and they crystallized into a complete practice with the work of [1] and [2]. I use these techniques throughout my work and have added my own innovations to them. Standard practices and my innovations are described in detail in Chapter 2.

Actuation physics Transducers are devices that convert energy from one form to another, and actuators are a specific class of transducers in which energy is converted into mechanical work. Different forms of energy, such as electric, fluidic, magnetic, gravitational, chemical fuels, and thermal can be used. Classic examples of actuators include hydraulic pistons and DC and AC electromagnetic motors. These types of devices work well for driving excavators, electric cars, air conditioners, and similarly-sized mechanical systems.

However, building the motor driving an air-conditioning fan in millimetric miniature is a fraught enterprise; the complexity and number of moving parts makes constructing such a device a dubious proposition. Moreover, it turns out that not only are some things difficult to do on certain length scales, it also might not be worth doing, even if you could build it, because of the way different forces scale.

To take a simple example, imagine skipping rocks: one does not reach for the round rocks, one looks for the flat ones. The flat rocks do not sink when thrown because the surface tension from the water balances out the pull of gravity. It turns out that surface tension scales directly with object length in contact with the fluid, i.e., symbolically: $F \sim L$. Gravitational force, on the other hand, scales with length cubed ($F \sim L^3$) because it depends on an object's mass. Thus, for the same mass, the flatter rock will experience greater surface

tension than the round one will.

We see other length scalings in engineered systems, as well elucidated by Trimmer [3]. For example, the force generated in pneumatic systems is proportional to the the piston head area, or $F \sim L^2$. Sometimes the situation is more complicated, and the scaling relationship becomes “it depends”. For example, electromagnetic force scales with L^4 if current density is held constant but L^3 if constant heat rejection is maintained and L^2 if constant temperature gradient with the environment is maintained. The caveat of these latter scalings is that significant energy is dissipated as heat and thus efficiency decreases dramatically.

It turns out, as Trimmer notes, that forces that scale with L^1 and L^2 work well on the millimeter scale. These include, most commonly in engineered systems, electrostatic and piezoelectric forces, under the assumption of constant electric field. Electrostatics are familiar— they are based on charge stored in a dielectric. Charge can be manipulated to draw two plates together or spread them apart. Piezoelectricity is slightly more complicated. Due to the crystal structure in piezoelectric materials, applied mechanical stress generates electric charge and vice versa. Thus, by applying some charge (or voltage), mechanical deformation of the material is produced.

Now, while the scaling of forces is central to the question of actuator selection, it is not the only consideration. Absolute force and displacement, bandwidth, lifetime, form factor, power consumption, and cost are the type of considerations and engineer might consider. On the centimeter or larger scale, the engineer might ask, “do I want a low-reduction gearhead or a standard one for my DC motor?” On the millimeter scale, the choice is decidedly more complex. In Chapter 4, I describe my work developing a particular type of piezoelectric actuator on the millimeter scale.

Millimetric medical robots One of the most challenging aspects of building millimeter-sized medical devices is also related to force generation; in surgical tools that reach into the human body, their ability to apply forces sufficient to interact with tissue is inhibited by (1) the stiffness of the cantilevered tool and (2) the difficulty of integrating miniaturized actuators directly at the ends of tools. For the latter reason, most robotic surgical tools are cable driven with remote actuation. However, cable-driven actuation is no panacea; the force that can be applied is limited by the allowable cable tension, which necessarily increases at small scales as the effects of friction increase. In my work, I look to sidestep these concerns by interacting with tissue — applying energy — in a way that does not require mechanical contact. In particular, I have developed a new robotic approach for controlling a laser in surgery that can deliver energy to tissue in a non-contact manner.

However, creating laser steering tools on the sub-centimeter scale required for robotic surgery is not a straightforward process of miniaturizing existing laser steering systems, such as the galvanometers used in refractive eye surgery. The bulky electromagnetic motors, encoders, and large field-flattening lenses used in those systems cannot be easily made on the millimeter scale. Rather, new materials, sensors, actuators, and assembly methods are needed to create and control miniature optical elements that can precisely steer surgical lasers. This, of course, ties back to challenges in millimeter-sized fabrication and scaling physics. This is the work that is described in Chapter 5 and Chapter 6.

The rest of the thesis will proceed as follows: first, with an overview of the PC-MEMs fabrication tools; second, with a recounting of my development of a new millimeter-scale fabrication method for fabricating compliant mechanisms; third, with a lengthy discourse on several iterations of development of a certain type of piezoelectric actuator on the millimeter scale; fourth, with a digression on a centimeter-scale laser steering tool and a description of some of the clinical realities motivating the need for robotic laser steering tools

in surgery; and last, I expound a millimeter-scale approach to laser steering incorporating all of the lessons previously learned in earlier work.

Chapter 2

Millimeter-scale Fabrication: Printed-circuit MEMs

Because my work draws heavily from the suite of PC-MEMs manufacturing techniques, I will briefly describe the core tools, materials, and design practices, before describing some of my innovations and extensions.

2.1 Core tools

Laser micromachining Laser ablation is an attractive millimeter-scale manufacturing technique because of the small feature sizes, large aspect ratios, and high-throughput that is achievable. It is also very versatile—different laser modalities and focusing optics can be chosen to tune processes for specific types of materials. We have found the nanosecond pulse length, 355-nm wavelength laser with F- θ focusing optics yielding $\sim 250\ \mu\text{m}$ depth of focus to provide a nice mix of properties—able to cut a large range of materials with minimal heat affected zone and acceptably small spot size (~ 10 to $20\ \mu\text{m}$ for most sets of processing parameters). An essential component of this system is a high-quality alignment

camera, ideally in color, with resolution on the order of $1\ \mu\text{m}/\text{px}$. This allows for accurate registration of workpieces to the laser micromachining system.

Pin-aligned heat press Different materials are accurately joined together through pin-aligned lamination. Precisely-drilled aluminum plates interface the pieces to be laminated and are themselves held by an outer set of plates that holds several cartridge heating elements. Temperature is controlled by standard Watlow temperature controllers. The stack is aligned vertically and weights are discretely added to match the pressure specifications for the given cure cycle. In this process, various support materials are typically added to facilitate rotational alignment of the laminated structure and prevent bonding between the structure and the pin-alignment jig.

Hydraulic platen press A hydraulic platen press is a useful tool for creating custom laminates that can then be laser-micromachined into individual components. It is most commonly used for creating custom carbon fiber laminates.

Sputter coater Sputter deposition is a physical vapor deposition process in which material is ejected from a target and deposited in a conformal thin film on a workpiece. Metals such as aluminum, gold, copper, and constantan are typically used. It is a common MEMs fabrication technique, but it is also quite useful on the millimeter scale. The films created through sputtering are typically very thin (100s of nm to 1s of μm), but they are useful for creating higher-quality conformal layers than possible through lamination.

Parylene coater Parylene coating is a chemical vapor deposition process in which a polymer is evaporated and allowed to coat and recombine on the surface of a workpiece to produce a conformal, chemical and moisture resistant surface coating. Within PC-MEMs,

it is most often used to create a dielectric layer to prevent electrical breakdown in small actuators and sensors. Typical layer thicknesses range from 5 to 50 μm . It is a somewhat cumbersome process that lends itself more to parallel prototyping rather than serial prototyping. Large batches can be processed simultaneously, but each process takes \sim one day and requires tedious cleaning and preparation of the chamber.

Ultrasonic cleaner Ultrasonic cleaning is a useful process for assisting with chip removal of complex laser-machined components.

Plasma cleaning Plasma cleaning can be used for removing organic contaminants from surfaces before lamination. It is also critical for processing PDMS— bonding it to glass slides or to other PDMS components. Non crosslinked PDMS is a semi-liquid that can be molded into high resolution networks of channels and UV cured into a solid device; these types of “microfluidic” devices are used widely in life sciences research [4, 5]

Ferric chloride etcher A ferric chloride bath is a useful tool for creating circuit boards and is used most often in conjunction with a spin coater, which creates uniform layers of photoresist.

Laser welding Laser welding can be used for joining small metallic components. It is a non-additive process, so intimate contact between the joined parts is necessary for a strong bond. It is a useful process for single prototypes but difficult to perform repeatably without the use of alignment scaffolding.

Hobbyist CO2 laser A CO2 laser is a good general-purpose tool for creating assembly jigs, lamination support materials, and other fixtures for interfacing workpieces with the above tools.

Microscope and tweezers There are certain artisanal aspects to PC-MEMs that rely on a human to manipulate components under a microscope. This most often involves assembling components to be laminated, removing chips from laser machined structures, and joining and fixturing components that cannot be easily laminated.

2.2 Materials

Metals Most metals absorb the 355 nm laser wavelength used in standard PC-MEMs processes. Stainless steel is commonly used because it does not oxidize during lamination, and spring steel is used when flexible components are needed. One of the challenges of laser machining these materials is thermal management; local heating induces strains that can deform the workpiece and result in misshapen components. This becomes a problem for thicker steels (>3 mil). To minimize these effects, the workpiece is held firmly in place by a non-marking, sticky-gel adhesive layer underneath it (GelPak, Delphon) and by a frame of duct-tape around its border. It is also preferable to acquire these metals as flat sheets rather than rolls, so as not to fight any precurvature while fixturing. Another thermal management issue is the generation of a heat affected zone (HAZ) along the edge of cut edges. At the nanosecond pulse length, most metals experience a mixture of ablation and melting, and the latter results in the recast HAZ. The HAZ is undesirable because it can inhibit bonding during lamination. To remove it, one typically uses a high grit sandpaper (600-1200 grit) and isopropyl alcohol (IPA). This, incidentally, also is a good way to loosen chips and prepare the surface for lamination. The last common metal used is copper, which is used as an electrode material in a variety of contexts. It is often sanded after lamination to remove oxides then tinned to protect against further oxidation. It also can be purchased in two-ply sheets that are loosely cohered, which allows for the copper to be laminated and

then the outer ply peeled off to reveal a clean copper surface beneath.

Polymers Polyimide is the workhorse polymer used in PC-MEMs processes. Its high glass transition temperature ensures that it is dimensionally stable during laser ablation and heat-press lamination. It is used most often as a flexible layer to provide revolute motion in composite structures, but it is also often used as a lightweight spacer layer. Polyimide is almost always used in conjunction with a heat curable acrylic adhesive which allows it to be bonded to other (often rigid) components. We use the DuPont Pyralux flame-retardant series of adhesives in 12.7 μm and 25 μm thicknesses. These adhesives have good dimensional stability during laser ablation, and their flow during lamination can be easily tuned by altering the lamination pressure. FEP is the final commonly-used polymer; its chemical resistance, high melting point, and low friction makes it an ideal release film during lamination.

Ceramics The two ceramics most commonly used are PZT-5H and alumina. PZT-5H is a polycrystalline piezoelectric ceramic commonly used in actuators and sensors due to its piezoelectric large coupling coefficients. The challenges and intricacies of laser processing PZT-5H are well documented by Noah Jafferis [6, 7]. Care must be taken to not alter the dielectric or mechanical properties of the piezoceramic in undesirable ways through the application of the laser energy. Alumina is a very stiff (300 GPa) ceramic used as a mechanically strong dielectric material used primarily in the formation of piezoelectric actuators.

Composites A variety of composites are commonly used from the carbon and glass fiber families: intermediate and high modulus carbon fibers, S2 glass, and E glass. They are typically used in microrobotic systems when weight is a concern and their large specific

moduli are thus needed for constructing light, stiff structures. They are generally acquired in pre-preg form, meaning that the fiber/resin matrix is uncured. They are then laminated together to form composite laminates, such as 0-90-0 carbon fiber laminates, or instead are directly used as adhesive materials in a laminate stack. This latter usage is important for creating the strong mechanical bonds needed for efficient force transfer. One caveat is that the bond quality depends on the quality of the pre-preg, which is somewhat variable (dependent on age, moisture, and temperature) and can be difficult to ascertain before bonding.

2.3 Design practices

For simple devices, most design can be done in 2D layout software, in a similar way to printed circuit board layout. Different drawing layers can be used to represent different layers of material. For more complex devices, 3D layout tools are needed for visualization and assembly. In that case, an intermediate step of migrating the 3D design into 2D drawings is needed. This is a somewhat arduous mechanical step, and it is not really reversible (it's difficult to generate a 3D model directly from 2D drawings). To mitigate this, I try to do as much design in 2D as possible and visualize 3D structures directly from 2D drawings. For 2D layout software, I prefer QCAD/CAM, an open source layout program from RibbonSoft, GmbH for its layout tools and built-in CAM module for generating G-code. Another approach is to use a set of software tools developed by Dan Aukes called “popupCAD” [8] which are intended to streamline some of the difficulties of those mechanical, manual processes.

2.4 Innovations

Throughout my dissertation research, I have developed many new techniques within the PC-MEMs manufacturing paradigm. They will be described throughout the chapters of my dissertation but I will highlight a few of them here:

Abrasive jet micromachining Abrasive jet micromachining is essentially a mechanical etching procedure. It can be used to subtractively process difficult-to-machine components, such as permanent magnets and ceramics. It is a non-thermal process, so thermal damage is minimized, and it works best on brittle materials. We acquired a powder blaster (Comco AccuFlo) for machining inductor cores, but I adapted it for other uses, most significantly for the mechanical etching of superelastic nitinol, which I describe in detail in Chapter 3.

Carbon fiber in-plane flexures In the process of developing new displacement-amplified piezoceramic actuators, I saw the need for thin, longitudinally stiff, in-plane flexible elements. I found that carbon fiber was a surprisingly attractive candidate because it can be machined with very little heat-affected zone, allowing for the creation of high aspect ratio flexible elements. The challenge of using carbon fiber flexures was mitigating the effects of the carbon dust generated during laser ablation. The carbon dust redeposits and can cause premature electrical breakdown in the piezoceramic material. The fabrication processes and carbon dust mitigation approaches are described in detail within the context of the design and deployment of those actuators, as described in Chapter 4.

Rail-and-disk modular assembly While developing the laser steering device described in Chapter 5, I saw the need for a new millimeter-scale assembly approach that allowed rapid, repeatable assembly of different components. Repeatable joining is particularly challenging—threaded components are difficult to use and adhesives are difficult to re-

verse without damaging the underlying structure (chemical and thermal approaches are used). Thus, I developed a new approach that employs a set of rigid rods and modular disk-mounted components that are slid like platters onto the rods. This allows for the integration of a wide variety of components— they just have to be able disk-mountable. Spacing between components is controlled by tubes on the rods and other empty disks. This is somewhat analogous to the pin-aligned assembly method used for PC-MEMs lamination. The components are held in place by a preload spring and retaining clip on the end of the device. I further expound on this technique in Chapter 6.

Chapter 3

Nitinol Living Hinges

3.1 Introduction

Nitinol has numerous properties that recommend it as a material for biomedical applications, including its superelasticity, biocompatibility, kink resistance, torquability, and fatigue resistance in strain-controlled environments. By exploiting these properties, passive devices such as stents, catheter tubes, guide wires, and stone baskets enable less invasive interventions and better surgical outcomes than would be possible with more rigid stainless steel tools [9, 10]. Incorporating nitinol in active robotic devices is an ongoing research interest, marked by the development of a variety of robotic systems [11, 12, 13] and mechanisms [14, 15] that leverage nitinol's unique properties to facilitate minimally invasive surgical interventions. Core to these efforts have been the development of new fabrication and processing techniques for machining the material while retaining its superelastic structure. This chapter represents one such advance.

The challenges of machining nitinol are well known: work hardening causes wear on mechanical cutting tools, laser processing results in a heat-affected zone (HAZ) and induces microcracks that must be removed in post processing, and wire electro-discharge machining

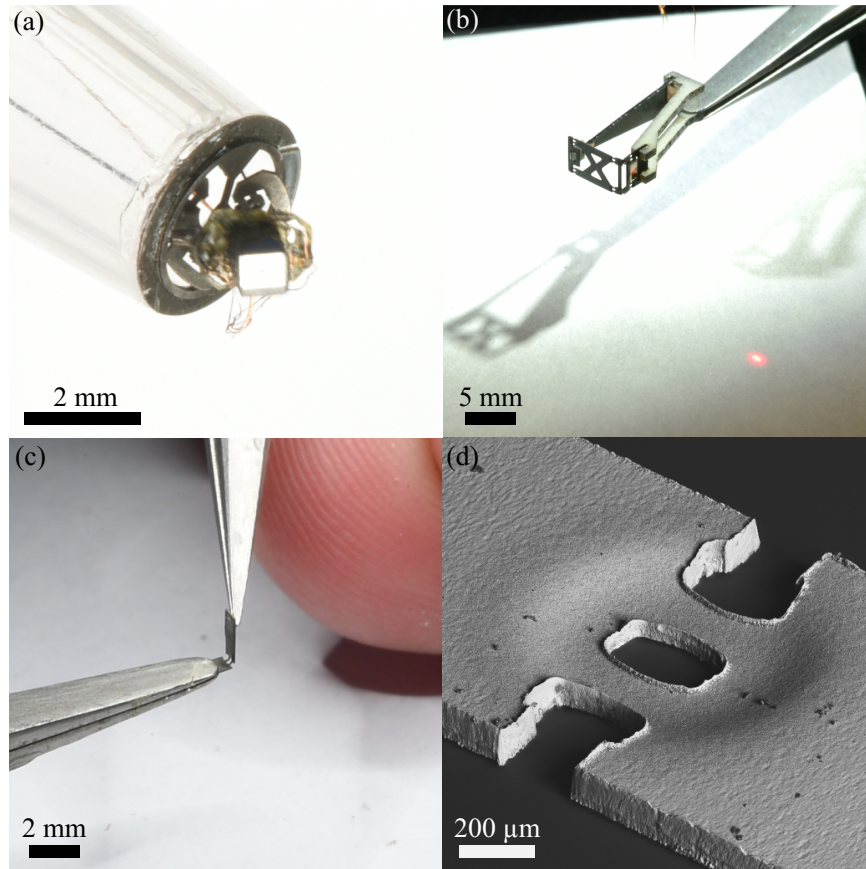


Figure 3.1: (a) Spherical five-bar linkage fabricated with nitinol living hinges, used as a camera-steering mechanism actuated by pull wires. (b) Four-bar nitinol linkage driven by a piezoelectric actuator, orienting a mirror to steer a laser beam. (c) 10 μm nitinol hinge bent to 90°, showing the large elastic range of these components. (d) Scanning electron microscope image of a typical nitinol hinge, showing the reduction in thickness accomplished through mechanical etching.

(EDM) similarly induces microcracks and can leave a recast layer from the oxidation of the electrode. Additional challenges arise for machining operations more complex than simple through cutting. Pocketing – the creation of blind cavities – is one such operation. Thin, fragile mechanical cutting tools cannot be easily plunged into the workpiece, sink EDM requires the creation of a specialized electrodes [16, 17], and laser rastering to selectively remove material creates a large HAZ that leads to the embrittlement of the workpiece and the loss of superelasticity.

Nevertheless, the ability to form blind cavities in nitinol is attractive because it would enable the creation of superelastic living hinges. Living hinges have well-defined rigid and flexible regions and are made from a single material. Superelastic hinges are of particular interest because of their large elastic limit (6-8%, typically, compared to 3% for polyimide, a commonly used flexure material, as described in Chapter 2). In general, living hinges facilitate the fabrication of complex mechanical systems while minimizing the number of parts needed, which simplifies assembly and joining processes. The latter benefit is potentially very relevant for nitinol, which is challenging to join to dissimilar metals and requires the use of intermediate layers [18]. Furthermore, living hinges allow devices to be made more compactly (especially in the thickness dimension), which is advantageous for microrobotic and biomedical devices, in which space and weight are at a premium [19, 20, 21]. Living hinges are a specific type of flexure, a compliant member that approximates the motion of a revolute joint. Within the context of millimeter-sized robots and medical devices, the primary appeal of compliant mechanisms based on flexures is that they allow the transmission of force and motion without bearing structures, which become inefficient, inaccurate, and challenging to fabricate as system size decreases.

The new fabrication approach described herein overcomes the manufacturing limitations posed by existing techniques by combining the meritorious features of two different methods: abrasive jet micromachining (AJM) and laser micromachining. Drawing inspiration from millimeter-scale fabrication of piezoceramics [22], I turned to AJM because it allows selective material removal through the thickness of a workpiece without a HAZ. In AJM, a fine powder consisting of hard particles is mixed with air and propelled in a fine jet to mechanically etch a solid surface. Blasting media size and type, pressure, nozzle distance, and other parameters can be tuned to achieve desired surface properties and etch rates [23]. Both masked and direct write methods can be used; I use a maskless method

here because of the low etch rates of nitinol. With the maskless approach, I use a horizontal x-y stage to control the nozzle location relative to the workpiece. After using AJM to modify a workpiece's thickness, I then use laser micromachining, which can make precise, high aspect ratio through-cuts, to define a part's final geometry in the lateral directions. Lastly, a low pressure AJM etch can be used to partially remove the HAZ generated by the laser (as employed during stent processing).

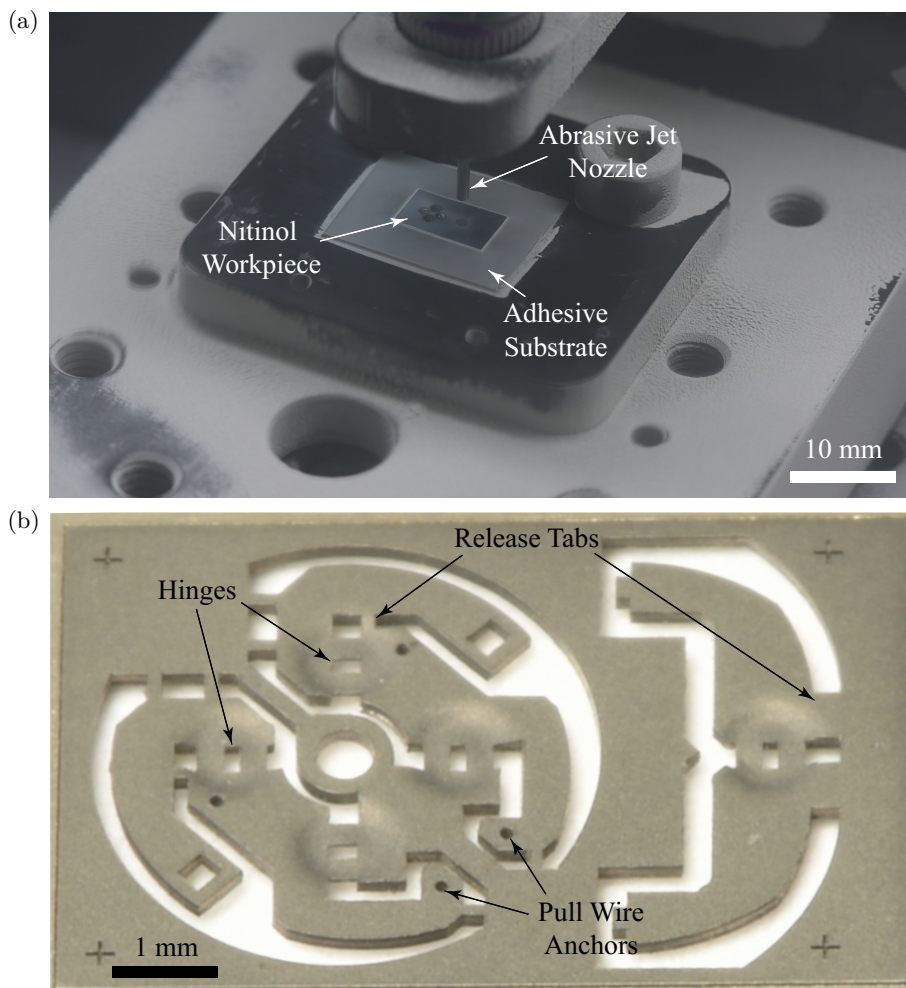


Figure 3.2: (a): Abrasive jet micromachining setup. The nitinol workpiece is held by an adhesive substrate and positioned beneath the nozzle using an x-y stage (not shown). (b): Example parts fabricated with nitinol hinges. The thin hinge regions are formed through abrasive jet machining and the outline of the structure is defined via laser micromachining.

This new fabrication approach allows for the fabrication of living hinges in nitinol that retain the superelasticity of the bulk material. A simple prototype device to demonstrate the use of this method is shown in Figure 3.1a; it consists of a single sheet of nitinol with rigid and flexible regions, with a single sheet of stainless steel bonded to the rigid regions to increase stiffness in those areas. The device, a spherical five-bar linkage, is shown controlling the orientation of a CMOS camera.

In this chapter, I fully describe the living hinge manufacturing process, including key relationships between processing parameters and etch rates. I show the selectivity of the fabrication method through the fabrication of hinges of a range of thicknesses. To allow hinges to be properly sized for particular applications, I provide a model for bending stiffness that accurately captures their full superelastic behavior. I then validate the model through a series of experiments, describe initial fatigue tests, and discuss avenues for further development. I anticipate the broad usefulness of this technique to enable new capabilities in millimeter-size robots and medical devices.

3.2 Manufacturing

The flexures are fabricated from a superelastic nitinol sheet (Johnson Matthey PLC). Square centimeter samples are mounted on a strong two-sided adhesive (Gel-Pak x8, Delphon Industries) and mounted on an x-y stage inside an AJM station (ProCenter Plus, Comco Inc). See Figure 3.2a. A controllable vertical stage rigidly holds the nozzle and controls its distance to the sample. Because I used a direct write method, the x-y stages are necessary to position the sample relative to the nozzle. This allows flexures to be precisely placed on a single sheet, which can then be incorporated as a flexible layer in a multi-material laminate or directly used in a device. Samples can also be post-processed using

other micromachining tools, such as tabletop mills, wire EDM, or laser cutters to make through-cuts and define the margins of the flexible regions. For example, to define the geometry shown in Figure 3.2b, I used an Nd:YAG laser (Coherent Avia 355-7) integrated in a laser micromachining center (Oxford Lasers, E Series). The center is removed from each flexure because it was seen that slightly more material remained at the center of the etch areas than the edges, likely due to the particle ejection dynamics.

In order to create flexures of predictable thickness, I characterized the vertical and lateral etch rates for two key processing parameters that are easily varied: pressure and nozzle distance (Figure 3.3). Both vertical and lateral etch rates initially increase with increasing nozzle distance before falling rapidly off. The vertical etch rate is very sensitive to pressure while the lateral etch rate is largely agnostic to it. For all tests I held nozzle diameter (450 μm) and blasting media type (10 μm alumina) constant. Those parameters were chosen with a view toward minimizing feature size. The etch profiles were measured on a confocal microscope (Olympus LEXT OLS4000), and then the etch rates were calculated based on the time of each etch.

3.3 Modeling

With a view towards designing flexures for particular applications, I created a model for predicting bending stiffness as a function of geometry; geometric parameters are shown in Figure 3.4. Bending stiffness is nonlinear with the flexure angle due to nitinol's

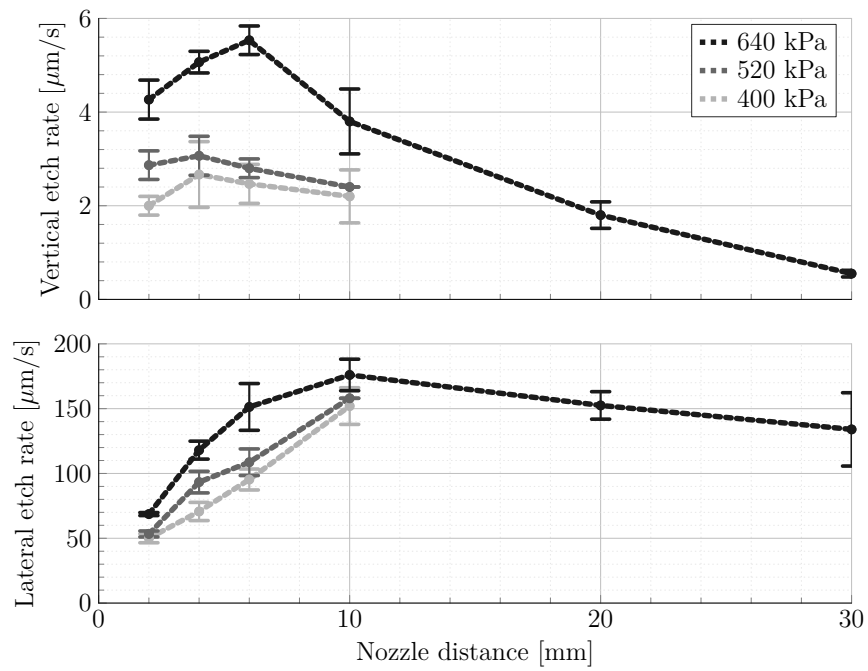


Figure 3.3: Vertical and lateral etch rates for nitinol at various pressures and standoff distances. The same blasting media ($10\mu\text{m}$ alumina) and nozzle diameter ($450\mu\text{m}$) were used for all tests.

superelasticity, which can be described in the simplified “bilinear” model:

$$\sigma(\epsilon) = \begin{cases} -E\epsilon_\ell + E_n(\epsilon + \epsilon_\ell) & \epsilon < -\epsilon_\ell \\ E\epsilon & -\epsilon_\ell \leq \epsilon \leq \epsilon_\ell \\ E\epsilon_\ell + E_n(\epsilon - \epsilon_\ell) & \epsilon > \epsilon_\ell \end{cases} \quad (3.1)$$

Where $\epsilon_\ell = \sigma_{cr}/E$ is the elastic limit of the austenitic phase, σ_{cr} is the stress just before stress-induced martensite begins to form (nucleation), and E is the elastic modulus of the austenitic phase. The elastic modulus of the mixed austenitic/martensitic phase, E_n , is much lower than E .

I assume that the assumptions of constant curvature bending apply and note that it will begin to fail as the ratio t/ℓ increases. Under those assumptions, pure bending about the x -axis (Figure 3.4) will result in strain linearly distributed about the bending plane, and given by:

$$\epsilon(y, \theta) = \frac{y\theta}{\ell} \quad (3.2)$$

The moment-angle relationship can be calculated first by defining the strain energy density at a single strain state as:

$$W(\epsilon) = \int_0^\epsilon \sigma(e) de \quad (3.3)$$

Where e is the dummy variable of integration. Then, by integrating the strain energy density with respect to the flexure volume, the total strain energy density can be calculated.

$$U(\theta) = \int_V W(\epsilon(y, \theta)) dV \quad (3.4)$$

Lastly, Castigliano’s first theorem can be directly applied to compute the moment generated

by the hinge for a given angle of rotation:

$$M = \frac{\partial U(\theta)}{\partial \theta} \quad (3.5)$$

Material Properties		Geometric Parameters	
E	50 GPa	w	400 μm
E_n	7 GPa	ℓ	200 μm
σ_{cr}	750 MPa	t	15 to 50 μm
ϵ_ℓ	1.5 %		

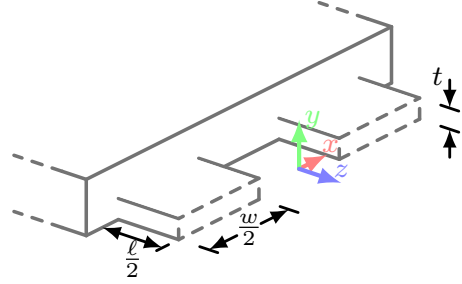


Figure 3.4: Material properties and geometric parameters for the fabricated flexure hinges, with a schematic representation for reference.

3.4 Characterization

To validate the model and demonstrate the versatility of the manufacturing process for producing flexures with particular stiffness, I fabricated flexures of varying thicknesses and characterized them using the test setup shown in Figure 3.5a. A flexure is held vertically between two rigid pieces of a thick fiber reinforced composite (FR4, 450 μm). One side of the flexure is rigidly attached to a servo and the other side is allowed to slide against an arm that is rigidly attached to a high-resolution six-axis force/torque sensor (ATI Nano-17 Titanium, SI-8-0.05, ATI Industrial Automation). The bending moment generated by the flexure is measured about the z-axis of the sensor, which has suitable resolution (<1 N μm after filtering) for resolving the generated moments, which range from 20 to 200 N μm .

For each test, the servo was driven with a cyclic motion profile with frequency ~ 1 Hz and magnitude appropriate to not plastically deform the flexure under test. Data was collected from the force/torque sensor at 1 kHz, processed with a 100-order median

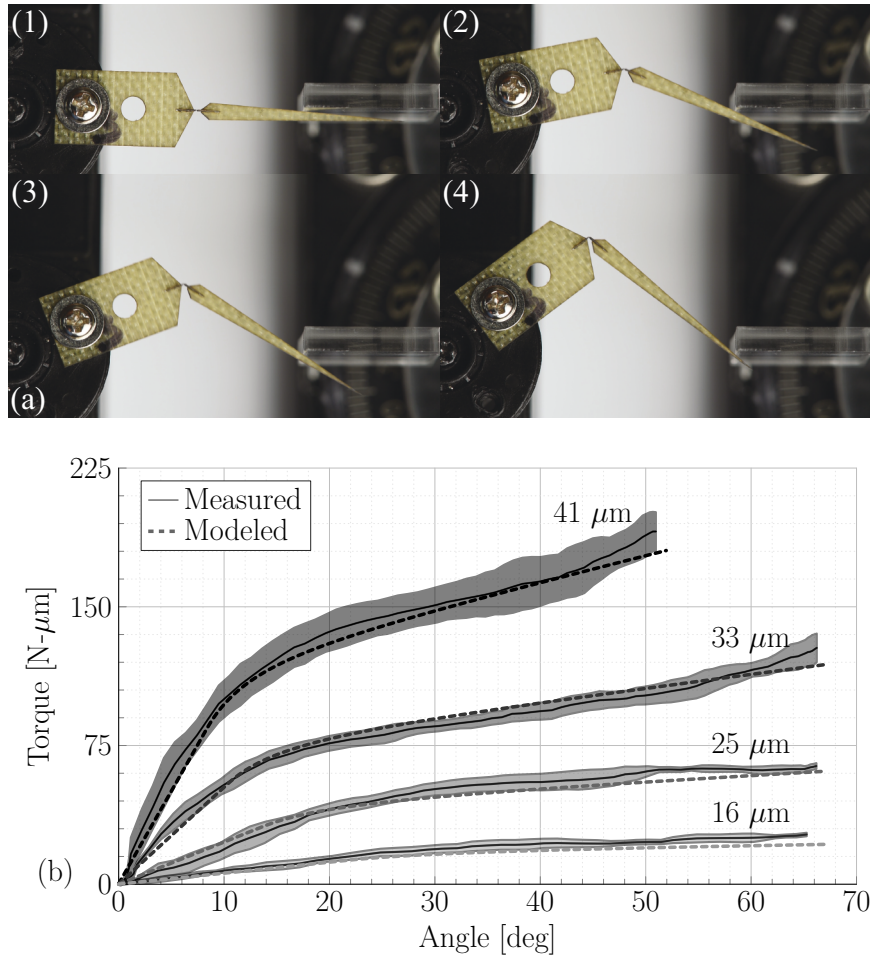


Figure 3.5: (a): Experimental setup for measuring the torque profiles of the flexure hinges. The servo (at left) controlled the angle of the flexure hinge (center) relative to the force/torque sensor (out of page, right). All tests were conducted quasi-statically at a loading frequency of ~ 1 Hz. The sequence shows elastic deformation of the flexure under test from 0 to 70° . (b): Experimentally measured and modeled torque vs. angle profiles for a range of hinge thicknesses. Experimental data was gathered under displacement control and averaged over five cycles. The mean and standard deviation of the measured data are shown for each flexure. The model captures the flexures' nonlinear behavior and reasonably predicts their torque vs. angle profiles.

filter (chosen to reduce signal noise while preserving the signal edges), and averaged over the loading cycles. Five cycles were used for each flexure, which was sufficient to reduce the standard deviation for each measurement to within 10% of its mean value. I assumed that the servo followed a constant velocity profile except for short ramping periods at the extreme points of its trajectory. The flexure angle was then calculated from the servo angle as a function of the link lengths of the test setup.

The results, presented in Figure 3.5b, demonstrate the model’s ability to predict both the absolute stiffness of different sized flexures as well as the nonlinear loading path that each takes. The initial loading regions correspond to the predominance of austenite and the plateau regions that follow correspond to the nucleation of stress-induced martensite. The critical torque that marks the transition between the two regimes for each flexure is seen to be roughly quadratic with thickness, as expected from classic beam theory.

3.5 Prototype Devices

The first prototype device, shown in Figure 3.1a, incorporates four living hinges in a spherical five-bar mechanism. Its constituent parts are shown in Figure 3.2b: a flat piece with the four hinges arranged radially symmetric about the device center and a second piece that connects across the top of the device to constrain the linkage to spherical motion. Release tabs are used to limit off-axis forces on the flexures during assembly. The linkage is actuated by four pull wires that anchor to the structure through micro holes drilled using laser micromachining. Each wire corresponds to bending in one quarter of the hemispherical workspace of the spherical five bar. Because of the small size of the device, the effective moment arms between the pull wire anchors and the flexures are quite short, and thus the amount of shearing in the flexures and the force required to generate bending is significant.

To ameliorate this effect to some degree, I added a stainless steel backing to enhance the stiffness of the rigid regions of the nitinol workpiece and thus better define the joint centers.

In the second prototype device, shown in Figure 3.1b and Figure 3.6, a laser beam is steered using a mirror attached to the pivot link of a four-bar mechanism formed from contiguous nitinol with well-defined hinge and structural regions. The linkage was made from two separate nitinol pieces, joined together via laser welding. The slider of the mechanism is driven by a piezoelectric bending actuator. This device well-illustrates the value of the living hinge approach: a minimum of components and materials are need to achieve the motion transmission from the quasi-linear motion of the piezoceramic to the rotational motion of the mirror. These types of transmissions will be developed in more detail in Chapter 5 and Chapter 6

3.6 Discussion

Though the direct write etching method described herein allows for the fabrication of simple hinges, it cannot produce the complex geometries that would be possible with a masked process. I conducted initial experiments in this direction using a commercially available dry film photoresist specifically formulated for sandcarving (4 mil RapidMask High Tack, Ikonics Corp), but I was unable to find suitable processing parameters that resulted in faster etching through nitinol than the resist. I expect that a suitable mask will be hard to find because of the relatively slow etch rate of nitinol. This can be seen by comparing it to a material more suitable for abrasive jet etching, such as glass or the piezoceramic described in [22]. The reported etch rates for the piezoceramic were $\sim 50x$ higher for similar processing conditions and required standoff distances on the order of centimeters instead of millimeters. Though masking seems like an implausible path for to achieve greater etch

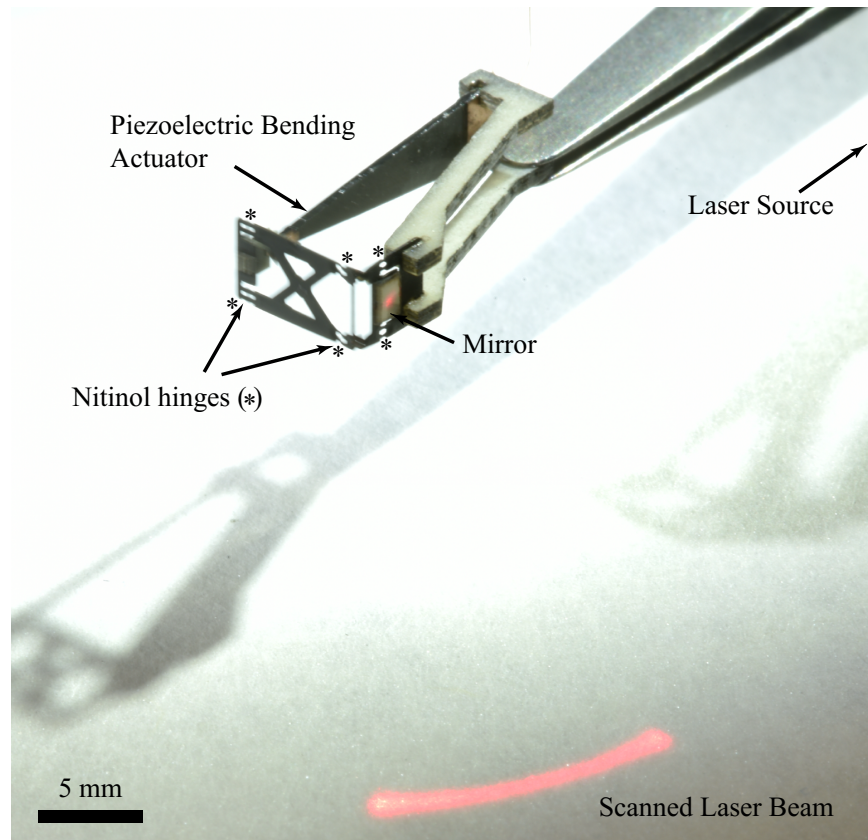


Figure 3.6: Laser scanning device fabricated using the procedure described in this chapter. A piezoelectric bending actuator provides a linear input to a four-bar linkage consisting of rigid and flexible regions of nitinol. A mirror on the pivot link of the linkage steers the laser beam along an arc as shown. The image was captured with a long exposure to show the range of motion of the linkage.

complexity, CNC tooling seems like a natural next step in the development of this technique. The abrasive jet stream could be continuously moved relative to the workpiece in order to create complex 2.5D etch patterns.

I conducted initial experiments into the living hinges' fatigue life and found that they failed at around 2000 cycles when cycled at 1 Hz from unloaded to 6% strain. Nitinol fatigue life is governed by crack initiation rather than crack propagation [24], and thus preventing or limiting microcrack formation during fabrication is a primary concern. Fatigue properties can be improved by electropolishing and thermal treatment [25], and thus I expect

an exploration of the techniques to be a natural extension of the work described herein.

3.7 Conclusion

A new method was proposed for fabricating living hinges out of nitinol, such that the superelasticity of the bulk material is retained after fabrication. Two prototype devices were presented that demonstrate the motion transmission capabilities enabled by this process. Using the model and processing parameters described, these hinges can be properly sized for given loading and displacement conditions, and I anticipate that they will be broadly useful in a variety of millimeter-sized robotic and medical device contexts, in which large ranges of motion are needed in compact spaces.

Chapter 4

Piezoelectric Flexensional Actuators

4.1 Introduction

The central idea behind this chapter is simple: piezoelectric actuators have small intrinsic displacement and generate large forces; how does one build a converter to trade off force for displacement? And how does one do this with the fabrication tools and materials available on the millimeter scale? These questions are contextualized in the challenges laid out in Chapter 1.

One small shift in thinking that was very important to me was reframing the design problem away from energy density (the work output normalized to mass) and into mechanical efficiency (the quotient of actuator work output and active element work output). Energy density is a slightly more abstract quantity and is important for comparing the performance of different types of actuators. However, because it embeds information superfluous to the mechanical design of the device, it is difficult to use as a metric around

which to frame one’s thinking with regards to mechanical design. By contrast, mechanical efficiency simply describes the quality of a mechanical design. Moreover, it is a bounded metric, so it provides upper and lower limits on the achievable quality of design. This is very helpful for quantifying, understanding, and framing the impact of different design choices. The upshot, as I learned through this work, is that choosing the right metrics around which to frame one’s thinking is important and can accelerate or impede one’s progress in engineering design.

4.2 Background

4.2.1 Displacement amplification techniques for piezoelectric actuators

First, I will examine different techniques exist for amplifying intrinsically small piezoelectric displacements and consider their merits and demerits. The most common technique is internal leveraging, in which longitudinal strain is converted to bending through the addition of passive layers of material that shift the neutral bending plane. Such actuators include bimorphs and unimorphs on the macro [26, 6, 27], meso [7], and micro scales [28]. On the micro scale, internal leveraging has also been used to create pseudo in-plane motion with cascaded antagonistic unimorphs [29]. A key advantage of these devices is that they typically require little passive material to achieve amplification, which serves to increase energy density. Moreover, the lack of additional serial compliance in transmission elements generally serves to increase output impedance. However, the material is not strained uniformly through its thickness during bending, which is a material inefficiency and can lead to short lifetimes, due to elevated stress on the outer surfaces. Furthermore, the tip of a bending actuator traces out an arc that only approximates linear motion, which is a limitation in some applications.

The second most common technique for amplifying piezoceramic displacements is external leveraging, in which additional passive elements are added in a transmission to trade off force for displacement. These have been predominately produced on the macro scale [30, 31, 32] but have also been explored on the micro scale [33, 34] and to a limited extent on the millimeter scale [35]. Variations on this approach include using buckling to amplify motion [36, 37] and nesting actuators to further amplify motion [38, 39]. With the exception of [33], each of these designs has used piezoceramic stacks as their active elements. Advantages include truly linear motion and uniform straining of the active material, which should result in higher efficiency and longer lifetimes. A key disadvantage is that the addition of passive elements to an actuator inherently reduces its energy density. More subtly, it is challenging to not introduce unwanted serial or parallel compliances while introducing passive elements.

A third common technique for amplifying displacements is frequency leveraging. Actuators that use this principle typically have a vibrating stator that incrementally moves a rotor. Due to this construction, these devices are typically termed “motors”. Overviews of these devices can be found in [40, 41, 42]. On the macro scale, these devices typically use a ratcheting and locking principle [43], but on the meso and micro scale, stick-slip (i.e., inchworm) drives [44] or friction couplings driven by standing or traveling waves [45] are more common.

Lastly, one can amplify piezoelectric displacements using clever tricks with device geometry. A prime example is a macro scale spiral actuator [46] fabricated through fused ceramic deposition (nozzle deposited and sintered) and radially polarized, such that a large effective actuator length is packed inside a small area. The transverse displacements produced are thus much larger than if the actuator was a simple beam within the same area. A similar device [47] uses a meander-line geometry to increase the effective actuation length

for a given area.

4.2.2 Flexensional piezoelectric actuators

In this chapter, I will focus on one interesting type of externally leveraged piezoelectric actuator: the so-called “flexensional” actuator. In these actuators, the large tensile stresses generated via the converse piezoelectric effect ($\sim 25 \text{ Pa m/V}$) induce small displacements ($\sim 0.1\%$ strain) which are transformed through a flexible linkage into a larger displacement at the expense of output force. Ideally, the piezoelectric element would be able to deliver all of its energy to the output, but in practice this is difficult to achieve due to the compliance of rigid portions and stiffness of flexible portions of the amplification structure. The quality of this conversion is termed “mechanical efficiency”. Similarly, the ideal flexible linkage would have negligible mass relative to the active material. In practice, the non-negligible mass of the linkage is dead weight that doesn’t contribute to energy conversion. This suggests another quality metric, “mass efficiency”.

Mechanical and mass efficiency are useful concepts because together they describe the quality of an actuator design as a function of the geometry and material selection. They are more fundamental than quantities such as absolute output force, displacement, or bandwidth, which represent the performance of a specific design configuration (e.g., dimensions). For an ideal design, quality would be insensitive to configuration, but in reality, some dependence of quality on configuration will likely occur.

Together, mass and mechanical efficiency describe the reduction in energy density from that of the active material. A key goal of actuator design is often to maximize energy density [26]. Microrobotic systems such as those of Jafferis, et al. [48] and Yang, et al. [49] have severe mass and energy budgets— in those examples, every micro Joule of actuation energy counts toward greater in-flight capabilities, and every additional milligram of

weight counts against longer flight times and sensory payload. Energy density is similarly important in aerospace and satellite deployments and in active-damping applications, in which minimal passive inertia is desired. Considering actuator energy density in terms of mass and mechanical efficiency makes plain the options to increase it: reduce passive mass, better match active element and amplification frame stiffnesses, or use a more energetic active material. It also makes clear the upper bound on actuator energy density for which to aim – the full energy density of the active material.

4.2.3 Applications

The central contribution of this chapter is to demonstrate the design and fabrication of flexensional piezoelectric actuators on the millimeter scale with similar mechanical and mass efficiency at high transmission ratios to their centimeter-scale counterparts. In doing so, we aim to both enable new millimeter-scale systems and to facilitate the down-scaling of existing centimeter-sized devices. The potential applications for these devices on the millimeter scale are numerous, as judged by existing deployments in centimeter-sized systems. Claeysen, et al. [50], describe a host of device applications: micro-scanning and shutter control for high-speed optical systems, active damping and shape control in aerodynamic systems, and acoustic sourcing for mapping underwater pipe networks and structural health monitoring. Janker, et al. [51] describe a wing morphing mechanism and vibration absorbers for helicopters and automobiles. Zubir, et al. [52] incorporate a modified flexensional actuator into a microgripping tool. Feenstra, et al. [53] demonstrate a proof of concept device using the flexible frame to couple a piezoelectric stack to the vibrations of a backpack. Liu, et al. [54] and Lee, et al. [55] use flexensional actuators as the basis for in-plane and out-of-plane micropositioning stages, respectively.

The central reason for the current dearth of piezoelectric actuators on the mil-

limeter scale is the dual challenge of manufacturing and assembly. On the micro scale, well-developed MEMs techniques (i.e., metal-organic chemical vapor deposition and sol-gel deposition [56]) can be used. An overview of the development of processing techniques for thin-film PZT deposition and integration can be found in [57]. Similarly, on the macro scale, standard manufacturing processes such as milling, molding, 3D-printing, and machine assembly can be used. Challenges arise, however, on the millimeter scale, on which the most suitable manufacturing techniques are laser micromachining, micro wire electron discharge machining, and micro powder blasting (Chapter 1), all of which are subtractive techniques; the difficulty of manufacturing on the millimeter scale is due in part to the lack of viable additive techniques. Related to this is the larger challenge of accurately assembling constituent parts on the millimeter scale.

I overcome these challenges through the use of the PC-MEMs manufacturing tools (Chapter 2). This chapter describes the deployment of those tools in service of fabricating high-performing millimeter-sized flexensional piezoelectric actuators.

4.3 Gen I: FR4 Actuators

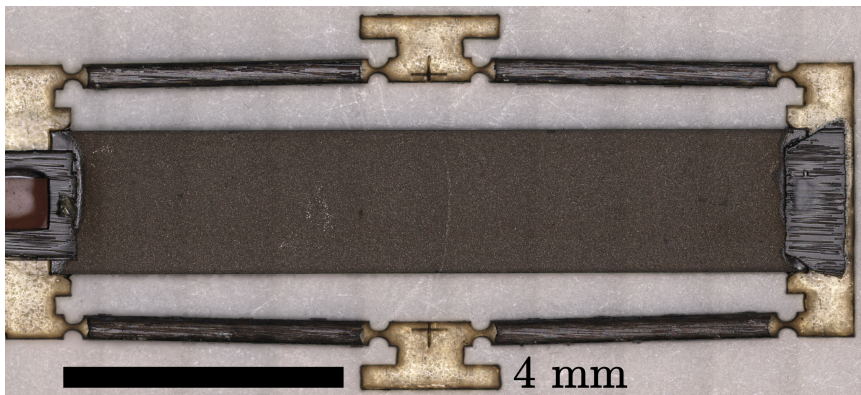


Figure 4.1: Gen. I flexensional actuator. The carbon fiber/FR4 linkages amplify the longitudinal contraction of the PZT member by 20 \times . Circular flexure hinges are used to produce rotational motion at the linkage joints. Device thickness is $\sim 200 \mu\text{m}$.

4.3.1 Composition

The basic design of the first generation actuator consists of a piezoceramic bonded to an external FR4 frame that geometrically amplifies the motion produced when an electric field is applied through the thickness of the piezoceramic. The key design parameters are shown in Figure 4.4. The designer is free to choose the size of the piezoceramic, the size and nominal angle of the linkage arms, and the flexure thickness. We chose to use circular flexure hinges, though it could be advantageous to consider other geometries.

Material selection was governed by a variety of considerations. I chose to use PZT-5H (Piezosystems, USA) because of its high strain constants, in particular, d_{31} . I used QA-112, an intermediate modulus, unidirectional pre-preg carbon fiber (Toho Tenax, Japan), because of its high specific modulus. For the frame, which includes the flexures, I chose to use FR4, a woven-fiber/resin composite, for its high strength-to-modulus ratio and its thermal stability at the cure temperature (150 °C) of the QA-112 resin. Finally, I incorporated copper layers to provide a low resistivity path for the drive signal.

4.3.2 Fabrication

The proposed design is straightforward to manufacture using the PC-MEMS manufacturing paradigm, in this case incorporating laser micromachining and pin-aligned heat and pressure lamination. An overview of the process is shown above in Figure 4.2 and is explained in detail as follows:

(1) I began by fabricating individual layers of PZT-5H, FR4, paper-backed resin-impregnated carbon fiber, and copper using laser micromachining. A 355-nm 8-W pulsed laser system is used (Oxford Lasers E Series). The laser spot size is power dependent and ranges from 7 to 20 μm , and the position accuracy ranges from 5 to 15 μm . Care is taken to minimize chemical composition change of the piezoceramic during laser processing,

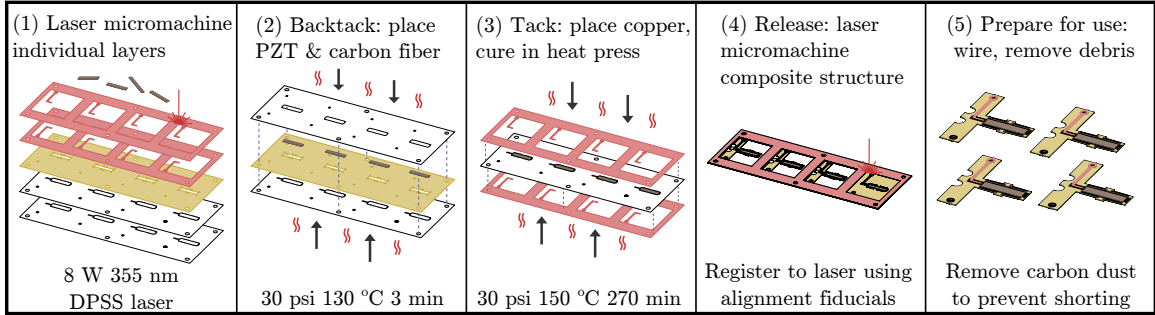


Figure 4.2: PC-MEMS process workflow. The process is easily parallelized for batch manufacturing.

which occurs during melting and resolidification of the material and results in reduced dielectric strength, as described in [6]. In practice, this means using several thousand cut passes at a relatively low laser power (0.23 W at 20 kHz pulse rate) to limit melting of the piezoceramic. Alternatively, one could use micropowder blasting (Chapter 3) to cut the piezoceramic, as in [22], which would obviate the possibility of thermal damage; however, downsides of the technique exist, namely etch anisotropy and the need for extra process steps (photolithographic masking).

The paper-backed carbon fiber is processed using two steps: first, a low power cut through the carbon fiber that defined the desired final geometry, and second, a high power cut through the carbon fiber and the paper backing to create alignment holes and voids over regions in which resin flow was undesirable. The carbon fiber that was not part of the final geometry was subsequently peeled off of the paper backing.

(2) Next I place the 8.5×1.5 mm piezoceramic beams into slots in the FR4 layer and use alignment holes to mate the carbon fiber layers on the top and bottom of the FR4 layers. The structure is then partially cured (30 psi, 150°C, 3 min) to transfer the carbon fiber from its paper backing to the FR4. This is a key step that allows carbon fiber to be placed only where desired. This is important for three reasons: first, by minimizing the amount of carbon fiber used, unwanted resin flow onto the piezoceramic or the to-be-

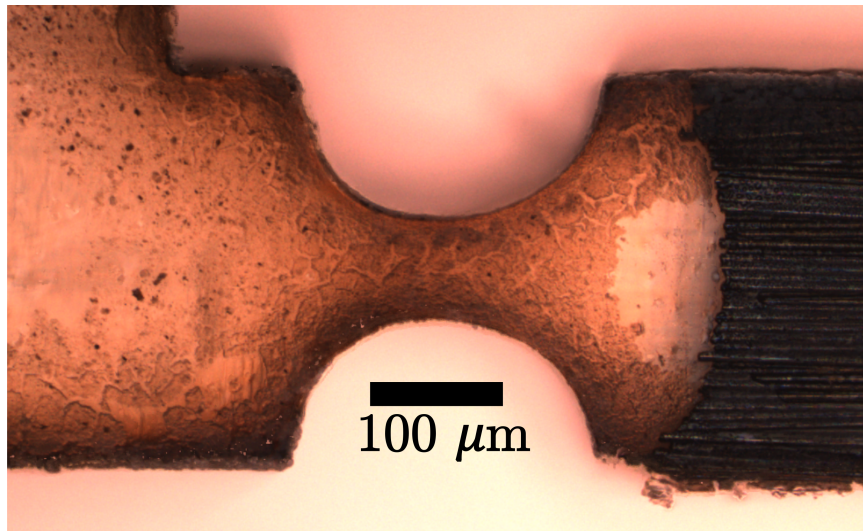


Figure 4.3: Circular flexure hinge (center) and carbon fiber reinforced linkage arm end (right) created during laser micromachining release cut.

created flexure joints can be avoided; second, it is critical to avoid cutting carbon fiber during the release cut (step 4, below), because the ablation process releases carbon dust that binds to the substrate edges, shorting the device; third, because mismatch between the top and bottom layer of carbon fiber can cause warping in the laminate during curing, putting stress on the piezoceramic. Minimizing the amount of carbon fiber can minimize this effect. During the carbon fiber transfer process, compressible (Pacothane Technologies PACOPADS) and chemical resistant layers (FEP) were added to ensure a uniform pressure distribution and minimize resin flow, respectively.

(3) Following the carbon fiber transfer process, I peel off the paper backing and mate the copper layers to the revealed carbon fiber/FR4/carbon fiber laminate. The structure was fully cured (30 psi, 150°C max, 270 min), once again with the temporary addition of compressible and chemically resistant layers.

(4) After the laminate is cured, I register it to the laser micromachining system using alignment fiducials and cut the final geometry of the device. This is the step in

which the amplification mechanism is formed; care is taken to cut the fine features of the mechanism (the flexure hinges and linkage arms) before fully releasing the structure. Low power is used to minimize laser spot size and avoid thermal damage to the laminate, in particular, the FR4. A zoomed-in image showing a fabricated flexure is shown in Figure 4.3.

(5) After the actuator is released from the substrate, it is cleaned with isopropyl alcohol to remove any carbon dust deposited during laser ablation. I typically place the actuators in an 80 °C ultrasonic bath for 5 min. Removing the carbon dust minimizes the risk of electrically shorting and is especially important for high-field operation. Finally, the actuator is wired and prepared for testing and/or integration into robotic devices.

4.3.3 Design

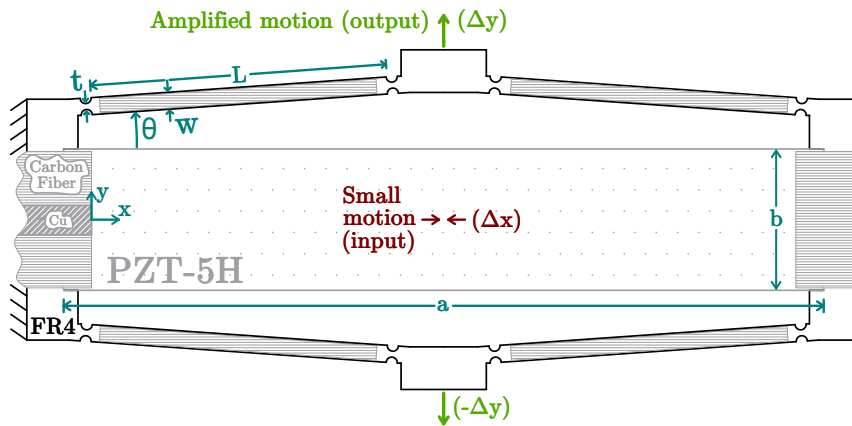


Figure 4.4: Design schematic of the amplified linear actuator along with geometric parameters and principle of operation (top view). Small strains in the piezoceramic are transmitted through the flexure hinges and linkage arms to produce amplified motion at the output links. The piezoceramic is bonded to the frame using resin-impregnated carbon fiber. Electrical signals are applied through copper bonded to the top of the carbon fiber. The device has top-bottom and front-back symmetry.

My goal for the first generation device was to maximize its amplification factor, which I define as the ratio of the output displacement of the mechanism and the contraction

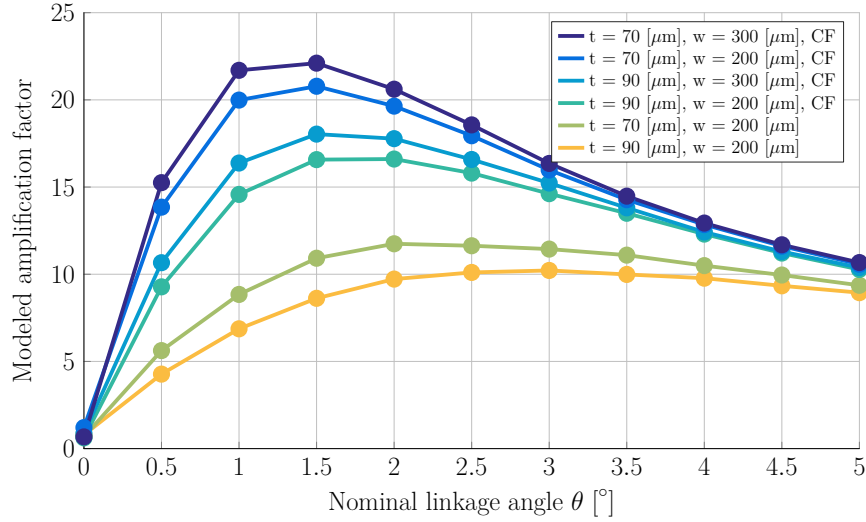


Figure 4.5: Modeled amplification factor as a function of geometry and materials. The nominal linkage angle represents the initial configuration of the mechanism with respect to the singular configuration ($\theta = 0$). Decreasing the flexure hinge thickness (t) increases the amplification factor, as do increasing the arm width (w) and adding carbon fiber reinforcements on the arms (CF). The amplification factor is nominally symmetric about the singular configuration for all device designs.

of the piezoelectric member:

$$\lambda = \lambda_A + \lambda_B = 2 \frac{\Delta y}{\Delta x} \quad (4.1)$$

as shown in Figure 4.4, where λ_A and λ_B are the amplification ratios of the top and bottom halves of the actuator, respectively. If the flexures at the joints of the mechanism are assumed to be perfectly compliant (i.e., revolute joints) and the links to be perfectly rigid, the amplification factor simply becomes:

$$\lambda = \cot \theta \quad (4.2)$$

where θ is the nominal angular offset of the mechanism from its singular configuration. This relationship represents an upper bound on the amplification factor for the quasi-static case.

When joint and link stiffness are considered, determining the amplification factor

becomes more challenging; the kinematics problem turns into a mechanics problem, which I solved using a commercial finite element package (COMSOL Multiphysics 4.4). The material properties used in the simulation are shown in Table 4.1. Linear elastic deformation was assumed, and the coupled piezoelectric/solid-mechanics problem was solved for varying applied voltages and frequencies. Amplification factor was found to be nearly constant across voltage and frequencies in the actuator passband.

The results of the model for a variety of actuator designs are shown above in Figure 4.5. I held piezoceramic size (a , b) and linkage arm length (L) constant and varied nominal linkage angle (θ), flexure thickness (t), linkage arm width (w), and the presence of carbon fiber reinforcement on the linkage arms. For each design, one can see a peak in the amplification ratio for some $\theta > 0$; these are the optimized geometries I am interested in selecting for a final design. In Figure 4.5, one also sees that decreasing the flexure thickness (t) increases the amplification factor and that increasing the linkage arm width (w) moderately increases the amplification ratio. Finally, we see a large performance improvement when we add carbon fiber reinforcements to the top and bottom of the linkage arms.

I heuristically set a lower bound on flexure thickness at $70 \mu\text{m}$ due to several concerns: first, the gap between fiber bundles in the FR4 is relatively large ($50 \mu\text{m}$); second, the accuracy of the fabrication method used was $\sim 10 \mu\text{m}$; and third, extremely thin flexures were to be avoided to prevent buckling under load. Thus, I chose to manufacture the design represented by the maximum in Figure 4.5. This displacement-optimized design has a nominal linkage angle of 1.5° , flexure thickness of $70 \mu\text{m}$, linkage arm width of $300 \mu\text{m}$, and contains carbon fiber reinforcements.

Output blocked force was also solved for using our finite element model, with the modeled force shown for our final design in Figure 4.6. The force determined by the finite element model was corrected using the substitution $Ed_{31} \leftrightarrow f_{31}$, where f_{31} , as defined in

	PZT-5H	QA-112	FR4
Elastic modulus [GPa]	60	170 (0°), 10 (90°)	22
Thickness [μm]	127	30	127
d_{31} [V/m]	-320×10^{-12}	–	–

Table 4.1: Material properties used in the finite element model. Note that the modulus and d_{31} constant of PZT-5H are, in general, field and strain dependent.

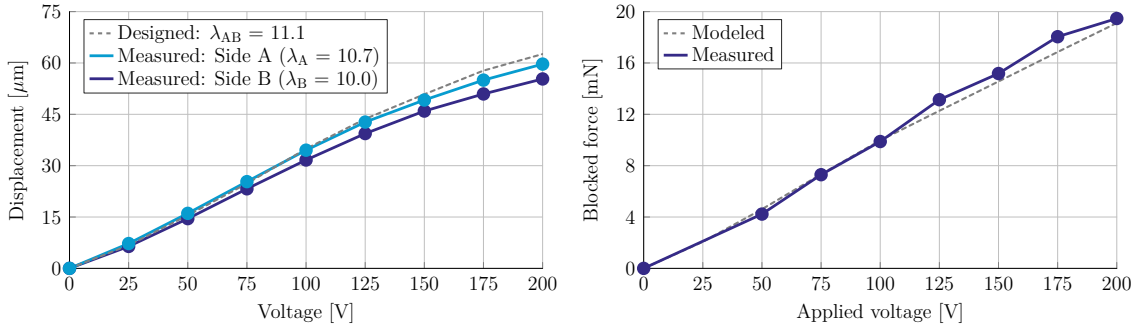


Figure 4.6: Output link displacement and force vs. applied voltage (quasi-static). The designed displacement was based on our amplification ratio model and on measurements of the actual displacement of the piezoelectric beam. The nonlinear response is due to the nonlinearity of the piezoelectric electromechanical coupling with respect to applied field.

[6], accounts for material nonlinearities in the piezoceramic at high fields and strains.

The manufactured geometry closely matched the designed geometry (see Table 4.2), though there is room for improvement. In particular, we found that there was some asymmetry between the two halves of the actuator. Measurements were taken using a confocal microscope (Olympus OLS 4000).

The output displacement vs applied voltage behavior is shown above in Figure 4.6.

	linkage angle θ [°]	flexure thickness t [μm]
Designed	1.5	[70, 70, 70, 70]
Side A	1.8	[78, 78, 61, 61]
Side B	2.0	[85, 81, 81, 57]

Table 4.2: Designed vs. produced geometry. Side A and Side B denote the two halves of the amplification mechanism (bottom and top halves, respectively, of the actuator in Figure 4.1). We see some discrepancy between designed and produced geometry and slight deviation between the two sides.

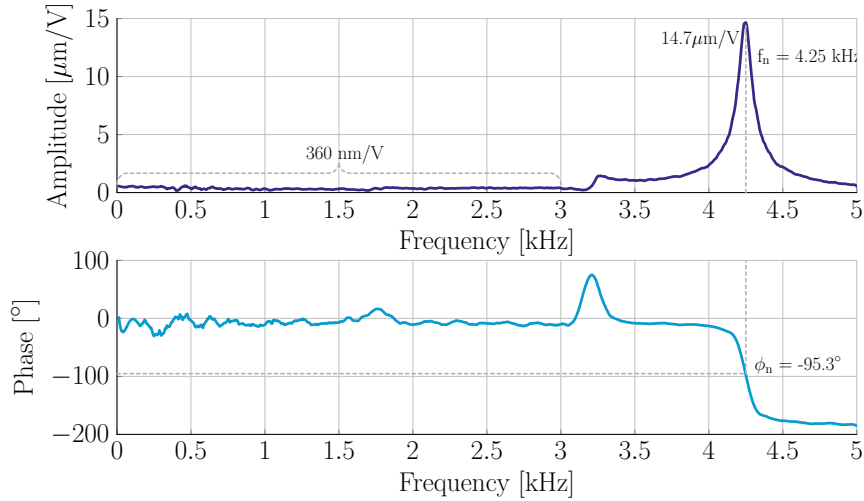


Figure 4.7: Frequency response of the Gen. I actuator.

One can see that both sides of the actuator slightly deviate from the designed behavior, though, given the geometry actually produced, both sides match well the model predictions in Figure 4.5. Measurements were taken with a laser Doppler vibrometer (Polytec PSV-500) with the actuator driven at 200 Hz, which is well within the bandwidth of the actuator and results in large velocities ($\sim 1\text{-}50$ mm/s) that are well above the noise floor of the vibrometer (~ 50 $\mu\text{m/s}$ for these tests).

The frequency response of the actuator was also measured using the vibrometer, and the results are shown below in Figure 4.7. White noise was used to stimulate the actuator. We see the expected second-order response for the system, with its resonance at 4.25 kHz. The passband displacement amplitude is ~ 360 nm/V, which is consistent with the displacement measurements for low frequencies taken above. The phase swing slightly above 3 kHz is likely due to the slight asymmetry between the two sides of the actuator or an out-of-plane mode.

Actuator blocked force was measured using the testbed shown in Figure 4.8. The actuator and test probe were mounted on linear stages to allow for precise alignment with

the force sensor (an ATI Nano 17). The actuator was positioned such that its linkages were undeformed at zero applied voltage and kept in this position for all tests. Measurements were taken across a range of applied voltages and are shown in Figure 4.6. We see that the measured blocked force closely matches our model.

Finally, we conducted a preliminary fatigue test and found that the actuator was able to complete 40,000 cycles under free displacement without failure when driven by a 3 kHz sinusoidal signal at 100 V.

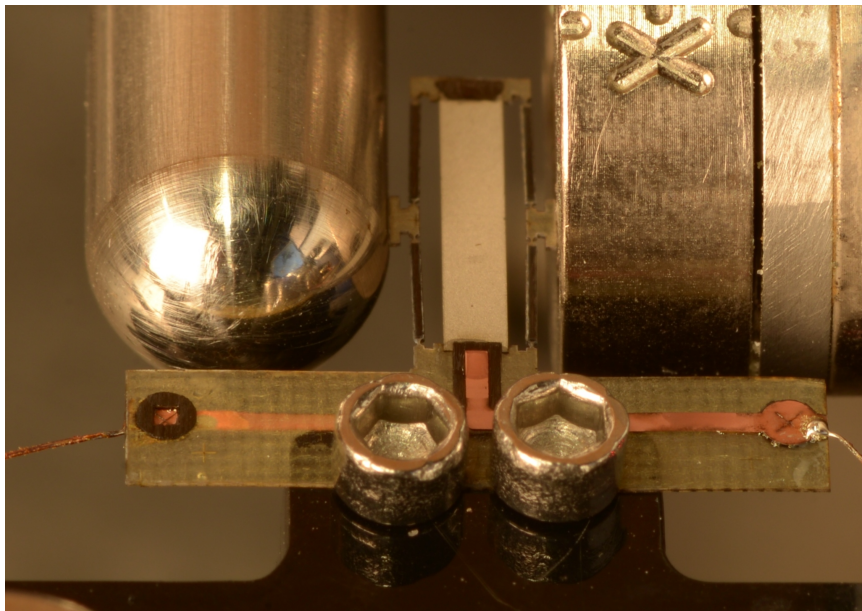


Figure 4.8: Gen. I Actuator blocked force testbed. Actuator is shown in the center with the force sensor on the right. The probe on the left was used to mechanically ground the actuator.

4.4 Gen II: Carbon fiber actuators

4.4.1 Composition

The second generation design ameliorated two key deficiencies of the first generation approach. First, it acknowledged that the width of the piezoceramic needed to be drastically shrunk, for reasons that will become clear in the forthcoming section. Secondly, I realized that if some carbon fiber support on the linkage arms was good, it would be even better to make the entire linkage out of carbon fiber. Those were the motivations that led to the second generation design, which consists of a narrower piezoceramic element surrounded by an entirely unidirectional carbon fiber displacement frame.

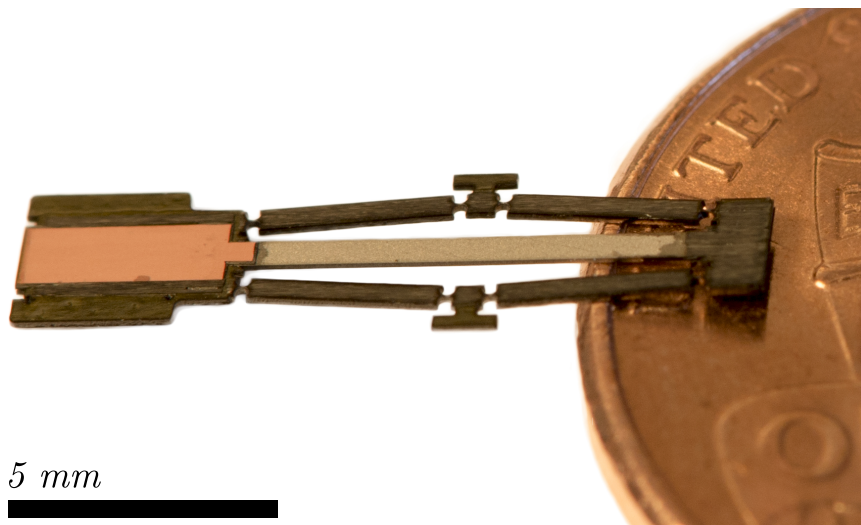


Figure 4.9: Second generation piezoelectric flextensional actuator shown with scale. The piezoelectric element (dark grey, center) is polarized through its thickness and driven by an external voltage source connected to the copper pads on the left. The carbon fiber flextensional frame produces a large displacement in response to a small contraction along the length of the piezoelectric element. Total device thickness is less than 200 μm .

4.4.2 Fabrication

The PC-MEMs process for making the second generation actuators incorporated laser micromachining, plasma etching, chemical vapor deposition, and precision pin-aligned heat/pressure lamination. The process is explained in detail as follows:

(1) I began by laminating four sheets of unidirectional prepreg carbon fiber with a thin polyimide sheet on top and bottom for electrical insulation. I used 30 μm thick intermediate-modulus carbon fiber (QA-112, Taho Tanex) and 5 μm thick polyimide film (Kapton 30 EN, DuPont) such that the resulting laminate had a compressed thickness of $130 \pm 2 \mu\text{m}$. A programmable heat press was used for the lamination (Carver Auto Series NE). The resulting laminate was to be used for the flexensional frame.

(2) Next, I formed individual layers of carbon fiber/polymide, PZT-5H, and copper using laser micromachining. The same 355-nm 8-W pulsed laser system was used (Oxford Lasers E Series) as before. This is also the step in which I form the flexures and linkage arms in the carbon fiber frame. I found that cutting these features upfront instead of cutting them after lamination (steps 4-5) and reregistration (step 6) resulted in greater symmetry between the top and bottom portions of the frame. In principle, the spot size and repeatability of the laser system are small enough to control the flexure thickness to within a few μm , which would allow for precise matching of the flexure hinge thickness within a desired specification.

(3) After micromachining individual layers, I ultrasonic cleaned (VWR 50HT) and plasma etched (Diener Electronic PCCE) the carbon fiber/polymide. A 2-min plasma etch in Argon is used. The purpose of the cleaning was to remove any residual carbon dust that was deposited during laser ablation and to prepare the surface for a parylene deposition. I deposited a 3 μm uniform parylene coat in order to electrically isolate the carbon fiber/polymide frame from the rest of the actuator. Chemical vapor deposition was

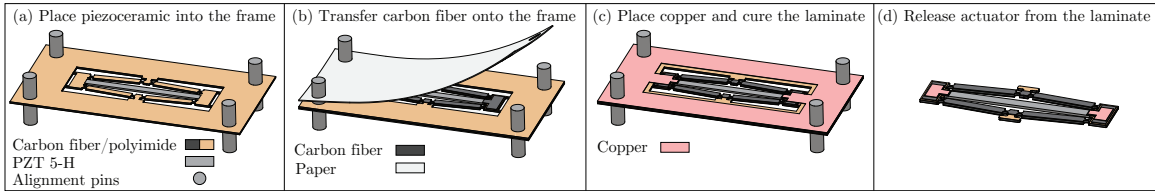


Figure 4.10: Key assembly steps: (a) Placement of piezoceramic beam in the laser-micromachined carbon fiber/polyimide frame. (b) Transfer of prepreg carbon fiber onto the assembly. (c) Placement of copper and curing of the laminate. (d) Following curing, the tabs are laser ablated to release the actuator from the laminate. A single actuator is shown for simplicity, but the process is easily parallelized to enable batch fabrication.

used for the parylene coating (SCS Specialty coating systems PDS 2010).

(4) Next, I laser micromachined the prepreg carbon fiber that would become the electrical and mechanical bridges between the carbon fiber/polymide/parylene frame and the piezoceramic. I then immediately (to avoid curing of the resin) placed the piezoceramic beams into slots in the frame and used alignment holes to mate the prepreg carbon fiber layers to the top and bottom of the frame. The structure was then partially cured (30 psi, 150°C, 3 min) to transfer the carbon fiber from its paper backing onto to the frame. See Figure 4.10a-b for detail. This is a key step that allows carbon fiber to be placed only where desired. It is important for three reasons: first, by minimizing the amount of carbon fiber used, unwanted resin flow onto the piezoceramic can be avoided; second, it is critical to avoid cutting carbon fiber during the release cut (step 6, below) because the ablation process releases carbon dust that binds to the substrate edges, shorting the device; third, because mismatches between the top and bottom layer of carbon fiber can cause warping in the laminate during curing, putting stress on the piezoceramic. Minimizing the amount of carbon fiber can minimize this effect. During the carbon fiber transfer process, compressible (Pacothane Technologies PACOPADS) and chemical resistant layers (FEP) were added to ensure a uniform pressure distribution and minimize resin flow, respectively.

(5) Following the carbon fiber transfer process, I peeled off the paper backing and

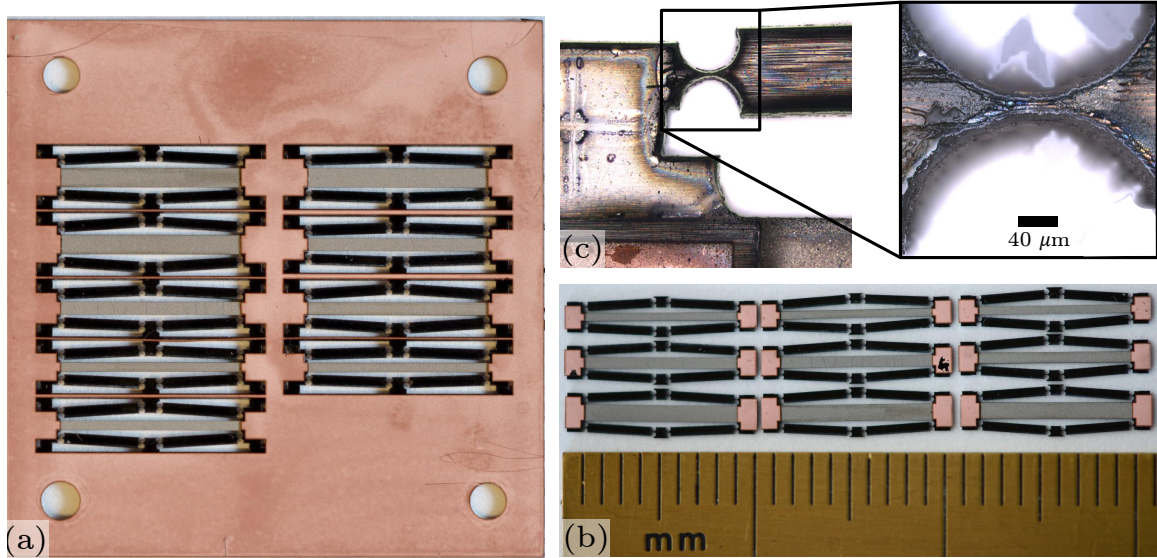


Figure 4.11: Batch manufactured actuators. (a) Laminated actuators before being released into individual pieces. (b) Actuators after being released from the substrate. These were the actuators manufactured for the model validation study. The aspect ratio r is varied in the vertical direction, and the nominal linkage angle is varied along the horizontal. (c) Zoomed-in image with a fabricated carbon fiber flexure.

mate the copper layers to the partially cured laminate (see Figure 4.10b-c). The structure was fully cured (30 psi, 150°C max, 270 min), once again with the temporary addition of compressible and chemically resistant layers. A typical laminate that was formed is shown in Figure 4.11a.

(6) After the laminate was cured, I registered it to the laser micromachining system using alignment fiducials and cut off the exterior tabs to release the device from the substrate. Once again, I was careful to avoid cutting through the carbon fiber frame in locations where electrical signals are present in order to avoid releasing conductive carbon dust.

(7) After the actuators are released from the substrate, they are cleaned with isopropyl alcohol to remove any carbon dust that was deposited during laser ablation. I typically placed the actuators in an 80 °C ultrasonic bath for 5 min. Removing the carbon

dust minimizes the risk of shorting and is especially important for high-field operation. The set of released and cleaned actuators used in the design study are shown in Figure 4.11b, and a close-up view of a fabricated flexure hinge is shown in Figure 4.11c.

4.4.3 Lumped parameter modeling

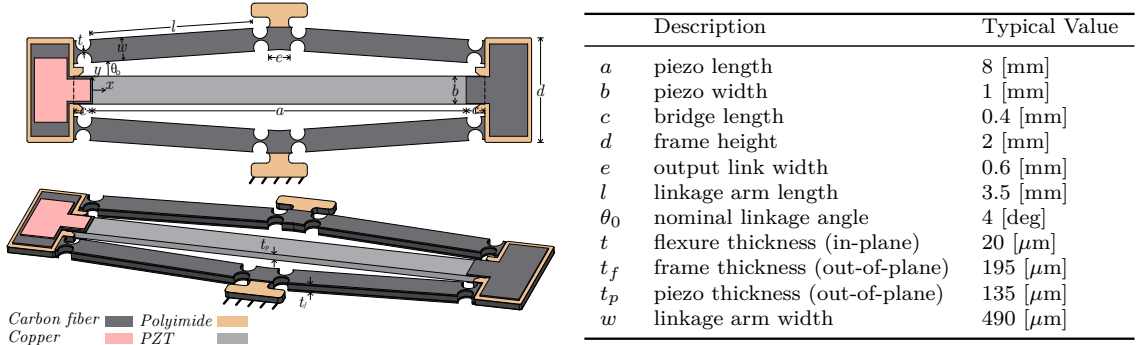


Figure 4.12: Flextensional actuator design schematic with materials and geometric parameters. Descriptions and typical values are shown on right.

I began the design process by simplifying the schematic shown in Figure 4.12 to the lumped parameter model shown in Figure 4.13. The piezoelectric element is replaced by a force source of magnitude f in parallel with a spring of stiffness k_p . The compressive force f is given by:

$$f = f_{31} V b \quad (4.3)$$

where f_{31} is an intrinsic material parameter that relates the stress generated in the piezoceramic to the applied electric field, V is the applied voltage, and b is the width of the piezoceramic element. Note that f_{31} depends both on applied electric field as well as the current strain state, and I use the empirical model from [6]. The stiffness k_p is equal to the compressive stiffness of the piezoelectric element, which is a function of the elastic modulus and geometric parameters. Note that the elastic modulus of PZT-5H increases with increasing compressive strain, and I use the empirical model found in [6].

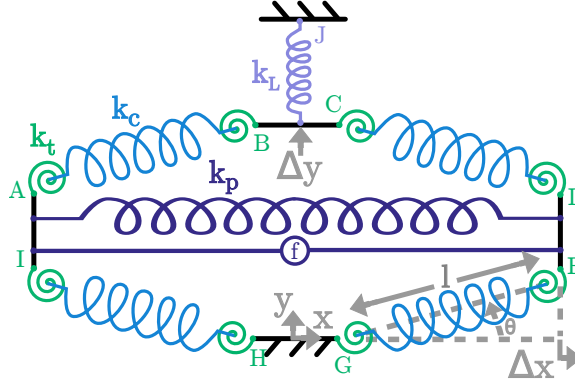


Figure 4.13: Lumped parameter model of the flextensional actuator. The piezoelectric element becomes a force source in parallel with a prismatic spring, while the flexures and linkage arms become torsional and prismatic springs, respectively. The principle of operation is that a small displacement Δx will produce a much larger displacement Δy due to the geometry of the linkage. Note that $\Delta x < 0$ in normal operation.

Similarly, the linkage arms are represented by torsional spring elements with stiffness k_t and prismatic springs of stiffness k_c . For simplicity of manufacturing, I restrict myself to using circular flexures, for which the torsional and compressive stiffnesses depend on Young's modulus Y_{cf} , flexure thickness t , fillet radius r , and frame thickness t_f . For constant fillet radius $r = 162.5 \mu\text{m}$, constant frame thickness $t_f = 135 \mu\text{m}$ (note that this is an effective thickness that ignores the effect of the low modulus materials, i.e., polyimide, parylene, resin), and constant modulus $Y_{cf} = 100 \text{ GPa}$, I conducted a simple finite element analysis to determine flexure stiffnesses as a function of Young's modulus and flexure thickness to be:

$$k_t = 0.3878t^2 - 2.00801t + 6.2 \text{ [N } \mu\text{m]} \quad (4.4)$$

$$k_{c,f} = -0.0001t^2 + 0.0296t + 0.5233 \text{ [N/}\mu\text{m]} \quad (4.5)$$

I used finite element analysis here instead of the standard lumped parameter representations for flexure stiffness because of concerns about the unsuitability of those representations

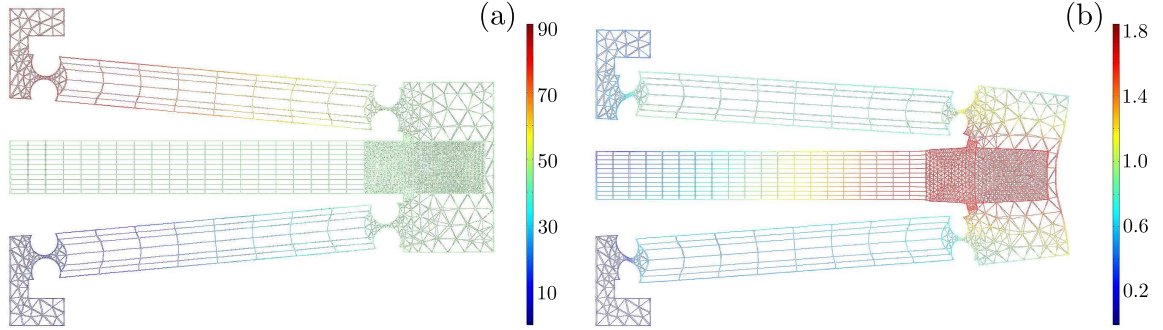


Figure 4.14: Finite element model of the flextensional actuator using COMSOL Multiphysics 5.2. Free displacement (a) and quasi-blocked force (b) simulations are shown. In both plots, total displacement is shown in μm for a $200 \text{ V}_{\text{pp}}$ input waveform, and deformation is scaled to facilitate visualization of the results. By exploiting symmetry I both minimize computation time and promote convergence.

for orthogonal materials. The magnitude of k_c is given by the series combination of the compressive stiffnesses of the flexure hinges, the linkage arms (treated as simple beams in compression), and the equivalent compressive stiffness due to shear of the member that connects the piezoceramic element to the linkage arm. This latter stiffness was found to be $1 \text{ N}/\mu\text{m}$ via finite element analysis. Lastly, I include a load spring with stiffness k_L in order to capture the actuator response to different loading conditions.

Due to symmetry, only two parameters are needed to represent any configuration, and to simplify the analysis, I chose l and θ . To further simplify the analysis, I assumed that links AI , BC , DE , and GH have zero length. Then, the static equilibrium equations for the actuator become:

$$\Sigma F_{x,D} = f + 2k_p\Delta x + 2k_c\Delta l c_\theta = 0 \quad (4.6)$$

$$\Sigma M_{CD,D} = (k_L\Delta y + k_c\Delta l s_\theta)l c_\theta + 2k_t\Delta\theta = 0 \quad (4.7)$$

where $\Delta l = l - l_0$ and $\Delta\theta = \theta - \theta_0$ describe the change from the initial configuration. The

output displacement and force are then given by:

$$\Delta y = 2(ls_\theta - l_0s_{\theta_0}) \quad (4.8)$$

$$f_{out} = k_L \Delta y \quad (4.9)$$

Moreover, the displacement amplification achieved by the linkage under no external load ($k_L = 0$) is simply:

$$\lambda = \left| \frac{\Delta y}{2\Delta x} \right| = \left| \frac{ls_\theta - l_0s_{\theta_0}}{lc_\theta - l_0c_{\theta_0}} \right| \approx \cot(\theta_0) \quad (4.10)$$

where the approximation holds for small Δl and $\Delta\theta$ (i.e. $\Delta l \ll l_0$ and $\Delta\theta \ll \theta_0$). Moreover, in the ideal case, in which the flexures have zero torsional stiffness and the compressive stiffness of the linkage arms is much greater than that of the piezoceramic element, the ratio of the output force to the force generated by the piezoceramic is simply:

$$f_{out}/f = \tan(\theta_0) \quad (4.11)$$

Because the product of (4.10) and (4.11) is unity, I note that the ideal flextensional actuator would be able to do the same work as the piezoceramic element acting alone, albeit with increased displacement and decreased force. The only losses in energy density would be due to the mass of the linkage frame.

4.4.4 Finite element modeling

To validate the lumped parameter model, I created a finite element model to capture the entire device physics and solve the coupled piezoelectricity/solid mechanics problem. All materials were assumed to be homogeneous and elastic. The elastic modulus of the piezoceramic was allowed to vary as a function of strain and the carbon fiber was

treated as orthotropic with the alignment of the fibers along the length of the actuator. Moreover, the piezoelectric coupling coefficient d_{31} was allowed to vary with strain and electric field according to:

$$d_{31} = \frac{f_{31}(\epsilon, E)}{Y(\epsilon)} \quad (4.12)$$

where E is the applied electric field, and ϵ is the strain in the x -direction. Thus, the strain-charge form for the piezoelectric constitutive relations becomes the nonlinear form:

$$\epsilon_{ij} = s_{ijkl}(\epsilon)\sigma_{kl} + d_{kij}(\epsilon, E)E_k \quad (4.13)$$

$$D_i = d_{ijk}(\epsilon, E)\sigma_{jk} + \epsilon_{ij}E_j \quad (4.14)$$

To promote convergence of the nonlinear problem, two simplifying assumptions were made. First, I treated the piezoceramic under the carbon fiber bridges as nonactive material with constant elastic modulus. This is reasonable because the bridge length (denoted c in Figure 4.12) is typically $< 10\%$ of the total length of the piezoelectric element and is restricted from contributing to the active deformation by the carbon fiber bridge. Second, I modified the nonlinear stiffness model from [6] in order to slightly smooth the problem; I used $\alpha = 6000$ instead of $\alpha = 8000$ as the value that governs the rate of transition from the low stiffness to high stiffness states. This resulted in only minor changes to the modulus of the piezoceramic ($< 4\%$ over strains in the region of interest) and makes the problem much more tractable to solve. Typical results are shown in Figure 4.14.

4.4.5 Design study

I found reasonable agreement between the finite element and lumped parameter models (see Figure 4.15) and thus felt confident to use the lumped parameter model to draw general conclusions about the design space as well as perform a design study. Using the

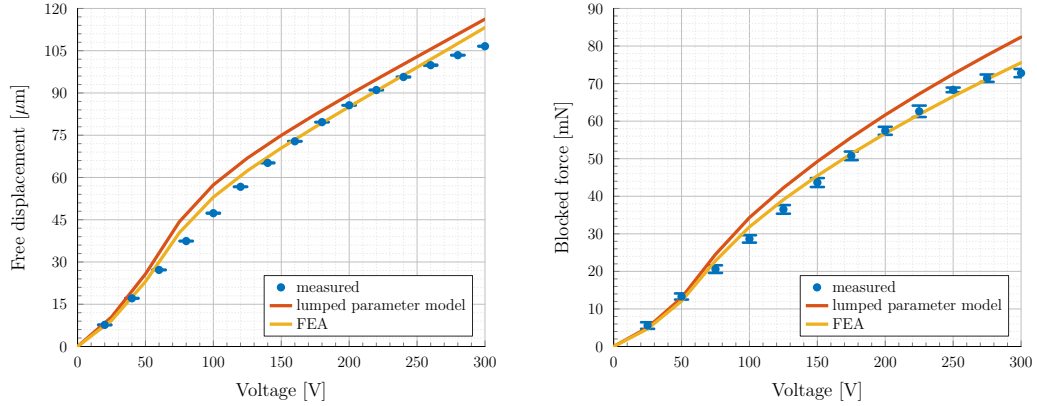


Figure 4.15: Modeled and measured free displacement and force for the high performing design: $r = 20$ and $\theta_0 = 3.3$ deg. Both the lumped parameter model and the FEA capture the measured free displacement data well (10.6% and 4.6% average relative error, respectively). The FEA captures the blocked force data well (5.7% error), and the lumped parameter model shows minor error (11.0%). The modeled values shown correspond to $Y_{cf} = 100$ GPa and the models are otherwise not fitted.

lumped parameter model, key relationships within the design space can be identified. An increase in the nominal linkage angle θ_0 (note Figure 4.12) will decrease output displacement but increase output force. For a constant piezoelectric element length a , increasing the width b will have negligible effect on displacement but will increase output force. Decreasing the flexure thickness t will increase displacement but decrease force. Finally, increasing t_f and w will increase force and have a small effect on displacement.

One can see that there is considerable flexibility within the actuator design space to achieve a wide range of application-driven requirements. These requirements would likely be related to device size, weight, and force/displacement characteristics. Other considerations could include electromechanical efficiency, lifetime (not modeled here, but empirical results are described in Section 4.4.7), and cost. In the first generation device, I optimized for free displacement. Here, I conduct a more general design study with the goal of demonstrating that the actuator can be designed to achieve a wide range of force/displacement characteristics. I also want to show that mechanical energy density, which captures in-

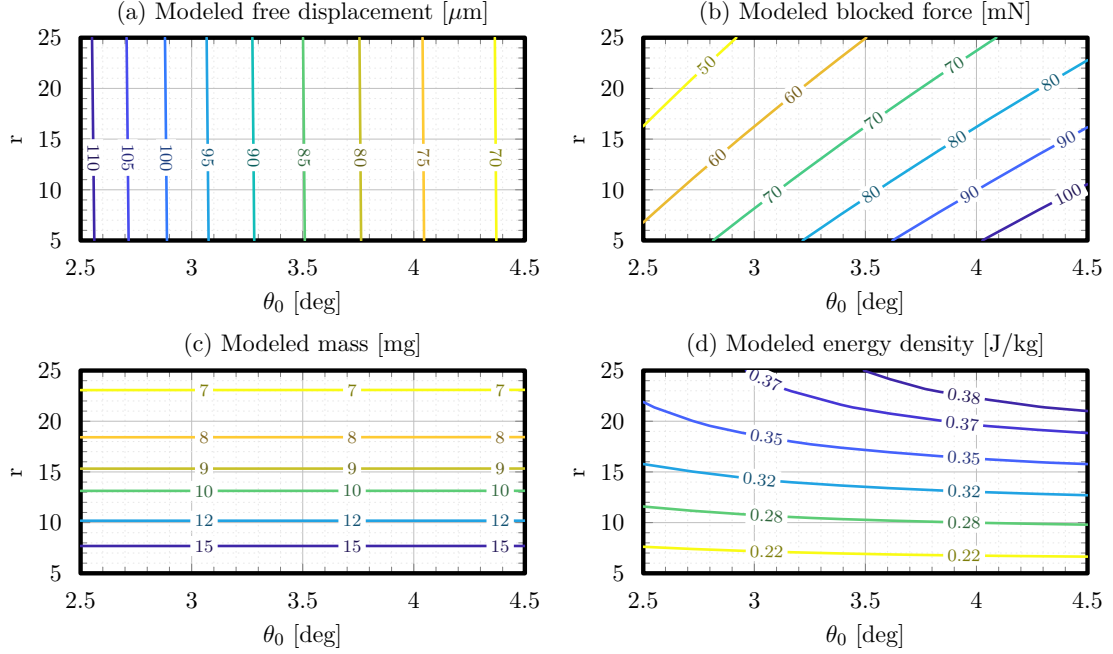


Figure 4.16: Design study modeling. The effect of varying the aspect ratio r and the nominal linkage angle θ_0 on modeled device performance is shown in plots (a-d).

formation about device weight and its force/displacement characteristics, stays relatively constant across designs. Assuming an actuator has a linear force/displacement profile (i.e. constant output stiffness), its energy density is given by:

$$D_u = \frac{f_{block}\Delta y_{free}}{2m} \quad (4.15)$$

where f_{block} , Δy_{free} , and m are the blocked force, free displacement, and mass, respectively.

To determine which design parameters most affect energy density (and by extension, force and displacement), I performed a sensitivity analysis, the results of which are shown in Table Section 4.4.5. I limited my analysis to the four parameters that can be easily varied during manufacturing: the nominal linkage angle θ_0 , the aspect ratio $r = (a + 2c)/b$, the flexure thickness t , and the arm width w . Some parameters, such as the thickness of the piezoceramic t_p , are not easy to vary because they are contingent upon material availability.

Moreover, some parameters, such as the length of the piezoceramic a are assumed to be governed by application requirements. Here, I used $a = 8$ mm for all designs. The sensitivity analysis was conducted by sampling $N = 2000$ random designs within the following ranges: $\theta_0 \in [1, 5^\circ]$, $r \in [5, 25]$, $t \in [10, 50 \mu\text{m}]$, and $w \in [100, 500 \mu\text{m}]$. These were chosen to capture all possible designs that could be manufactured while excluding designs that would result in undesirably low output displacement or force.

From the sensitivity analysis, I determined that θ_0 and r were the most critical parameters in the design space. To validate the model and demonstrate that this type of actuator can be designed to achieve a wide range of performance goals, I fabricated nine actuators, varying θ_0 and r each in three ways.

	θ_0	r	t	w
θ_0	.21	.01	0	0
r		.67	0	.01
t			.04	0
w				.07

Table 4.3: Variance-based sensitivity analysis. Each entry describes the effect of a design parameter or combination of parameters to the overall device performance (i.e., energy density). Sensitivity values were calculated via the Monte Carlo method with $N = 2000$ sample points.

4.4.6 Results

The performance of the fabricated actuators was found to reasonably match that predicted by the lumped parameter model, as shown in Figure 4.17. Across all nine actuators, the mean relative error in predicted versus measured free displacement and blocked force were $(6.5 \pm 0.7) \%$ and $(8.3 \pm 2.8) \%$, respectively. One can see that the model correctly predicts the trends in the data: as θ_0 increases, free displacement decreases and blocked force increases, and as r increases, free displacement decreases and blocked force

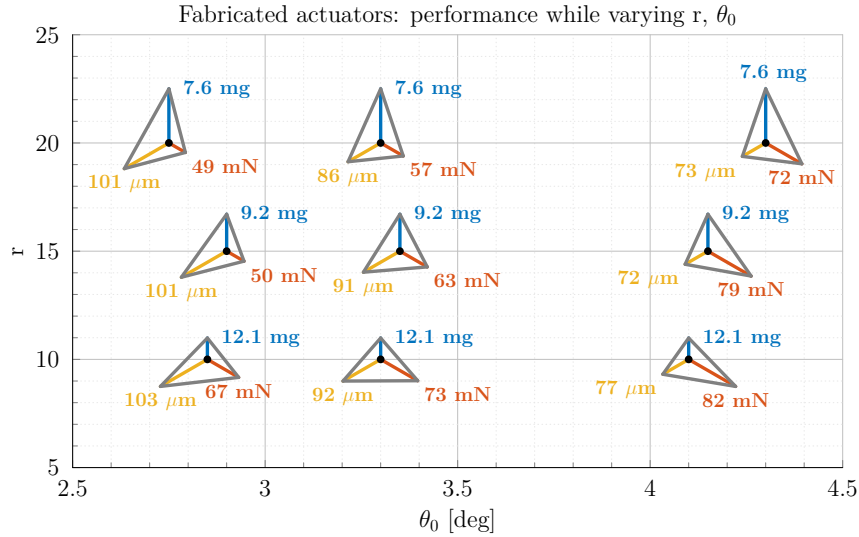


Figure 4.17: Design study results: Measured performance follows the trends predicted by the model and reasonably matches the predicted values. Note that the horizontal axis shows the nominal linkage angle (θ) and the vertical axis shows the aspect ratio of the piezoceramic element (r). The data demonstrate that the actuator can be designed to achieve a wide range of performance characteristics. All data were taken at a 200 V_{pp} operating voltage.

decreases.

The voltage response of one of the best performing actuators ($r = 20$ and $\theta_0 = 3.3^\circ$), is shown in Figure 4.15. Both the lumped parameter model and the FEA accurately capture the measured free displacement of the actuator, though only the FEA well captures the measured blocked force. This is likely due to the simplifications made to the geometry in the lumped parameter model.

The free displacement voltage response measurements were taken with the actuator in a quasi-static state (1 Hz driving frequency) with a laser Doppler vibrometer (Polytec PSV-500). Voltage measurements were taken in increments of 20 V from 0 to 300 V_{pp} . For each applied voltage, the velocity during forty periods of the drive signal was measured, averaged to find the periodic average, integrated to yield displacement, and recorded. The number of time averages was chosen to minimize the measurement error while maintaining

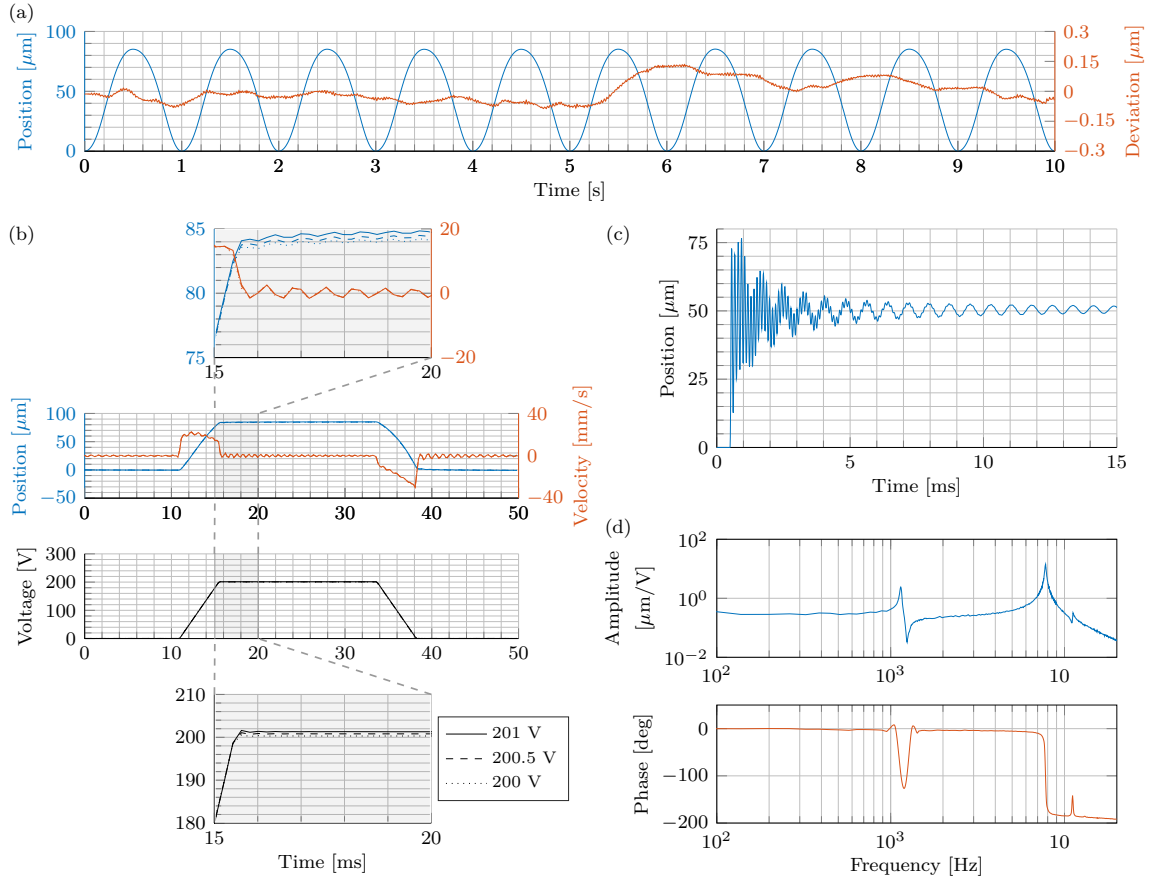


Figure 4.18: Actuator transient response in a variety of contexts: (a) Open loop repeatability while driven by a $200 V_{pp}$ sine wave. Absolute and deviatoric position are shown. Position deviation from cycle to cycle ($\sigma = 55 \text{ nm}$) is within the measurement noise ($\sigma = 144 \text{ nm}$). (b) Open loop position resolution. Position and velocity waveforms in response to ramp inputs are shown for ramp threshold voltages of 200, 200.5 and 201 V, and resolution of 300 nm is demonstrated. (c) Transient response to a $100 V_{pp}$ step input. One can see oscillations at both resonant frequencies that are present in the frequency response shown in (d).

a reasonable bound on total experiment time. Measurement error, defined as the average relative standard deviation, was found to be acceptably low: 0.4%.

Actuator blocked force was measured under the same drive signal with a high resolution force sensor (ATI Nano 17). The actuators were mounted in turn on a linear stage to allow for precise alignment with the force sensor. They were positioned such that their linkages were undeformed at zero applied voltage and were kept in this position for all tests. The measurement error for the blocked force measurements was reasonably low: 3.9%.

The transient response to sine, ramp, and step inputs is shown in Figure 4.18. All measurements were taken using the laser Doppler vibrometer on an actuator ($r = 15$ and $\theta_0 = 3.3^\circ$) that was slightly worse performing than the corresponding one used in the design study. In Figure 4.18a, I show the repeatability of the actuator in response to a $200 V_{pp}$ sine wave. The standard deviation of the response from the cyclic average ($\sigma = 55 \text{ nm}$) is within the measurement noise ($\sigma = 144 \text{ nm}$, recorded with no voltage input to the actuator), so I conclude that the repeatability is bounded by the measurement noise. In the Figure 4.18b, an actuator resolution of 300 nm is demonstrated. Ramp threshold voltages of 200 , 200.5 and 201 V were applied and actuator velocity was averaged over 100 cycles for each ramp voltage. The measurement noise for a null input with this averaging was ($\sigma = 14 \text{ nm}$). In Figure 4.18c, the transient response to a $100 V_{pp}$ step input is shown. Two resonances are visible, as can also be seen in the frequency response shown in Figure 4.18d. The lower resonance corresponds to the bulk motion of the piezoceramic, while the higher resonance corresponds to the oscillation of the output links.

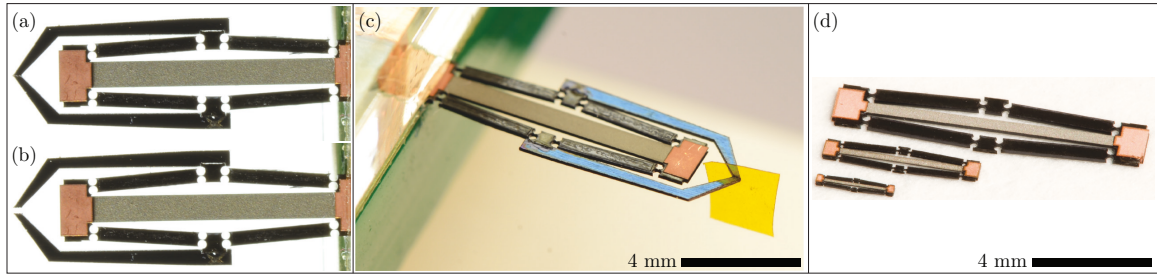


Figure 4.19: (a-c) Microgripper fabricated from a single flextensional actuator. The actuator is grounded at the base of the piezoceramic element, and the output links move away in equal and opposite directions from the center of the actuator when an external voltage is applied. (d) Half and quarter-sized actuators shown with full-size actuator for comparison. The half and quarter-sized actuators were fabricated with the same process that was used for the full-size actuator, though thinner piezoceramic and carbon fiber ($60\ \mu\text{m}$) was used for the smaller devices. Note that the scale bar is valid for all images (a-d).

4.4.7 Discussion

Though I have herein explored many interesting dimensions of actuator design and fabrication—lumped parameter and nonlinear finite element modeling, sensitivity analysis, and batch fabrication using an emerging manufacturing paradigm—many interesting questions remain. Primary among them is what types of devices this actuator might be useful in. One such device, a microgripper, is shown in Figure 4.19a-c. It was constructed through minor modification to one of the actuators used in the design study, and is able to grip objects of thickness 10 to $100\ \mu\text{m}$. It uses the actuator in its two-output configuration: the base of the piezoceramic beam is mechanically grounded and the output links actuate bi-directionally. One intriguing possibility with this device is to leverage its high bandwidth in de-grasping: to vibrate the actuator in order to break the surface forces that develop between the gripper and a grasped object. Other potential applications lie in micro-optics, either in micro-focusing or micro-zoom modules, or in micro-laser systems, such as miniature galvanometer scanners in which mirrors steer a laser beam at ultra-high speeds.

Related to the question of applicability is that of scalability: how small can it be

made, and does its performance change as we decrease size? I have begun investigating these questions, and have successfully manufactured the half and quarter-sized actuators shown in Figure 4.19d. The most challenging dimension to properly scale is the thickness of the actuator, as carbon fiber is only available in discrete thicknesses, and piezoceramic cannot be easily ground down lower than 50 μm . I used 60 μm for both the half and quarter-sized actuators (from Piezosystems, Inc). The 60 μm piezoceramic is much more fragile than the 135 μm and thus requires exceptionally delicate handling. For the carbon fiber, I formed a laminate of two sheets of carbon fiber (instead of four) and sanded it down to 54 μm , allowing the parylene coat to add the last 6 μm of thickness to the frame.

Other key questions remain with respect to sensing and control. If the actuator were to be used in a closed-loop control system for one of the applications described above, sensors would need to be integrated, dynamics derived, and a control law implemented. For sensing, a current-based method [58] would likely be the most straightforward to implement, but embedded strain-gauge approaches also are promising. Closed-loop control is likely necessary for accurate position control due to the hysteresis within the piezoceramic.

With regard to lifetime, I conducted a preliminary fatigue test and found that the actuator was able to complete 7 million cycles under free displacement without failure when driven by a 100 Hz sinusoidal signal at 100 V. Further tests are needed to characterize lifetime over a range of operating conditions.

The maximum achieved energy density of 0.51 J/kg is a tenfold increase over the Gen. I device. The key design improvements were the use of a higher modulus material for the frame, slightly increasing the nominal linkage angle, and increasing the aspect ratio of the piezoceramic element. These considerations are connected by the need to properly size the piezoceramic compressive stiffness to the compressive stiffness of the linkage arms and flexures. Another important design improvement was the incorporation of insulating

materials (i.e., polyimide and parylene) to allow for higher voltage operation.

4.4.8 Summary

The second generation flextensional actuator was made from a piezoceramic element and a carbon fiber amplification frame. The carbon fiber frame has flexures formed in it to allow rotation in key locations. Together, the piezoceramic and the amplification frame produce output displacements on the order of $100\ \mu\text{m}$ and blocked forces on the order of $70\ \text{mN}$. A design study was performed to show that my model accurately predicts trends in device performance and that force/displacement characteristics can be tailored for specific applications. A batch manufacturing process for the device was elucidated. Lastly, the actuator was shown integrated into a microgripper, and several other application areas for the actuator were described.

4.5 Gen III-V: Alumina-reinforced carbon fiber actuators

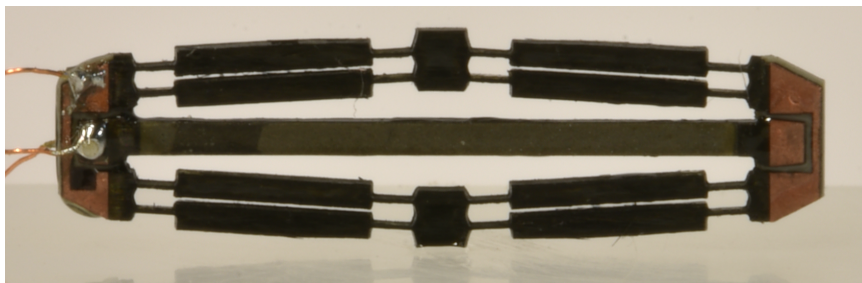


Figure 4.20: Fifth generation flextensional actuator, composed of a parallelogram carbon fiber amplification frame and alumina-reinforced base attachments.

4.5.1 Composition

Three key compositional improvements contribute to improved performance and manufacturability relative to previous two generations of these devices: (1) the incorpora-

tion of high-modulus alumina to create a stiff connection between the piezoceramics and the amplification frame, (2) the use of a parallelogram linkage structure to decrease the serial compliance of the amplification structure, and (3) the addition of a second layer of piezoceramic, which reduces out-of-plane motion and allows the fabrication process to be modified in advantageous ways. These differences can be partially seen in the image of a Gen. V actuator shown in Figure 4.20 and are illustrated in Figure 4.21. Note that the third generation design only incorporated the first design improvement, and that the fourth generation design used shorter flexures, but they were functionally quite similar to the fifth generation approach. Each design improvement is described in detail below, with a focus on the performance benefits accrued and the implications for device fabrication due to each modification.

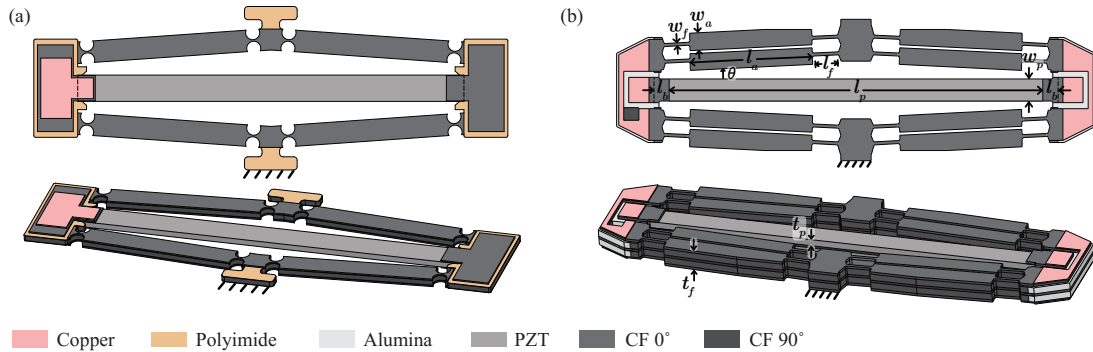


Figure 4.21: (a) Gen. II design, with a single piezoelectric element and a unidirectional carbon fiber frame that is insulated from the piezoceramic using a thin parylene coating. (b) Gen. V design, with two piezoceramic elements and an alumina-reinforced frame for more efficient force transfer. The parallelogram structure further reduces serial compliance in addition to inhibiting off-axis translation and rotation, which can arise from external disturbances or structural asymmetries.

Alumina base connections

In the second generation actuator design, the entire frame around the piezoceramic element was made from unidirectional carbon fiber. This had the advantage of minimizing

the number of parts needed while ensuring that the flexures and linkage arms were stiff along their length, i.e., in the direction of force transmission. However, unidirectional fibers have a key structural deficiency: they are weak in shear in the planes parallel to the fibers. This was an issue in the regions of the actuator connecting the piezoceramic to the flexure transmission. When the output link of the actuator was blocked, these regions could not resist the shear stresses that arose due to the contractile force of the piezoceramic. This is shown graphically in Figure 4.22.

In the improved design, the shear stiffness in the key connecting regions is increased by $\sim 30\times$ by replacing the unidirectional carbon fiber laminate ($G = 5$ GPa) with alumina ($G = 150$ GPa). Finite element analysis, shown in Figure 4.22, indicates that this yields an increase in blocked force of 40%, at the cost of a 9% increase in mass. Alumina is heavier than carbon fiber (3.9 g/cm³ vs. 1.6 g/cm³), but it only represents a small fraction (15%) of the total actuator mass.

Creating the composite alumina/carbon fiber frame also necessitated some rethinking of the fabrication processes. Previously, the carbon fiber frames were pre-machined and the piezoceramic elements placed inside before lamination. This is a somewhat fraught process, because nothing holds the piezoceramics in place during the lamination. This issue would be exacerbated by the need to also place alumina pieces inside the frame; moreover, this manual placement process is time sensitive, because prepreg carbon fiber desiccates and begins to cure out at room temperature, leading to inadequate interlayer bonding.

Double layer of PZT

To surmount these fabrication challenges, I added a second piezoceramic layer, which meant that the piezoceramic/alumina connection would no longer occur in the center plane of the laminate. This allowed the pieces of piezoceramic, alumina, and carbon fiber

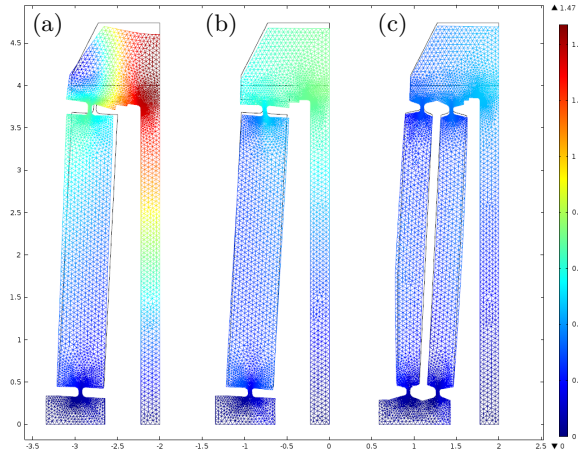


Figure 4.22: Finite element models (COMSOL 5.0) showing the internal deformation with the output link blocked for three different actuator designs: (a) carbon fiber frame, (b) alumina-reinforced frame, and (c) alumina-reinforced frame with parallelogram amplification linkage. Symmetry boundary conditions are imposed to simplify computation: only one quarter of the device needs to be modeled. The alumina-reinforced design experiences 40% less deformation at the piezoceramic/frame boundary than the carbon fiber design, and the parallelogram design sees 15% less deformation than the single-arm design. This fraction is the same by which the blocked force at the output link is increased.

to be held in place by carrier layers (Gel-Pak) and laminated together using the prepreg carbon fiber that becomes the center layer of the laminate. This approach is inspired by the fabrication process for bimorph bending actuators presented in [6] and is described in more detail below in Section 4.5.2.

Adding the second layer of piezoceramic roughly doubles the thickness of the device, which could be detrimental in the most space-constrained applications, but other benefits beyond manufacturability are accrued. During laser micromachining, a small taper on each edge is introduced. This variation in edge thickness results in a net moment being generated by the piezoceramic in addition to its contractile force. For the previous actuator design, this moment created an out-of-plane motion of the piezoceramic and resulted in out-of-plane motion of the output link on the order of a few percent of the in-plane motion. In the new design, by essentially stacking two of the previous actuators back-to-back, the

moments cancel and the out-of-plane motion is eliminated.

Increasing the thickness of the actuator also clearly increases the off-axis stiffness at the output link in the out-of-plane direction. This could be advantageous if the load being driven isn't well supported or is subject to external disturbances. A final, more speculative benefit is that by reducing out-of-plane motion, actuator lifetime at high voltages will be increased. The primary mechanical failure mode of piezoceramics is crack propagation initiated by tensile strain, and the parasitic out-of-plane bending implies some small tensile strain that could lead to premature failure of the device.

Parallelogram arm structure

The output force of the actuator can be further increased by about 15%, at no cost to energy density, by replacing the previous single arm amplification structure with a parallelogram topology. In the previous design, the contractile deformation of the flexures under blocked force limited the amount of force that could be transmitted from the actuator to the output link. The parallelogram structure essentially doubles the contractile and rotational stiffness of each flexure, but for the range of geometries under consideration, the effect of increasing the contractile stiffness is more pronounced on device performance. The manufacturing process for making the parallelogram structure is little changed from that of the single arm design. Some care must be taken for chip removal in the small internal regions between the flexures, but this is generally achievable through the appropriate selection of processing parameters.

The parallelogram arm structure has ancillary benefits on the output properties of the actuator, in both a static and dynamic sense. It is significantly stiffer than the single-arm approach in off-axis directions, particularly in the in-plane direction lateral to the output motion. Finite element analysis indicates an increase of $\sim 20\times$ in stiffness in

this direction. The increase in off-axis stiffness also implies improved disturbance rejection and attenuation of unwanted dynamic modes.

4.5.2 Fabrication

The actuator fabrication proceeds in three broad steps: lamination of the constituent materials, laser micromachining to create the actuator structure and release it from the laminate, and post-processing, which includes cleaning, dielectric breakdown enhancement, and wiring. The process easily lends itself to batch fabrication; only the post-processing steps require individualized handling and manipulation of the actuators.

The goal of the lamination step, shown in Figure 4.23, is to create strong inter-layer bonds while ensuring good lateral alignment between layers. The first two layers are formed from individual pieces of PZT-5H, as-fired alumina, and cured unidirectional M55J carbon fiber (a). The carbon fiber pieces are sanded to match the thickness of the PZT-5H and alumina (135 μm). The pieces are placed into the FR4 alignment frames and held in place by a gel carrier (GelPak x8, Delphon Industries). Small notches in the alumina allow the carbon fiber and piezoceramic pieces to be laterally aligned. Vertical alignment puts the piezoceramic and alumina pieces in direct contact, leaving a small gap in the vertical direction between the alumina and the carbon fiber pieces. The center layer (b), an adhesive layer, is formed from two pieces of prepreg M55J/RS-3C carbon fiber composite. The outer piece has its fibers aligned along the length of the actuator, to ensure strong mechanical connection between the piezoceramic and alumina and a low resistance electrical connection to the inner piezoceramic layers, and the inner piece has its fibers aligned perpendicularly to the actuator length, so as not to inhibit the piezo-induced motion. The outer layers (c), are made from prepreg M55J/RS-3C and a two-layered copper. The carbon fiber provides mechanical and electrical connection to the piezoceramic, and the copper allows for easy

electrical connection to external drive electronics. The assembly process is shown in (d-g); first, the FR4-held pieces are bonded to either side of the center layer (d-f), then the GelPak is peeled off and the outer layers are bonded on (g). During this lamination, a chemically-resistant layer (FEP) and conformable layer (PacoPad) are used to ensure uniform pressure throughout the stack and are then discarded after the lamination. A pressure of 25 psi and the manufacturer-recommended temperature profile were used for both laminations.

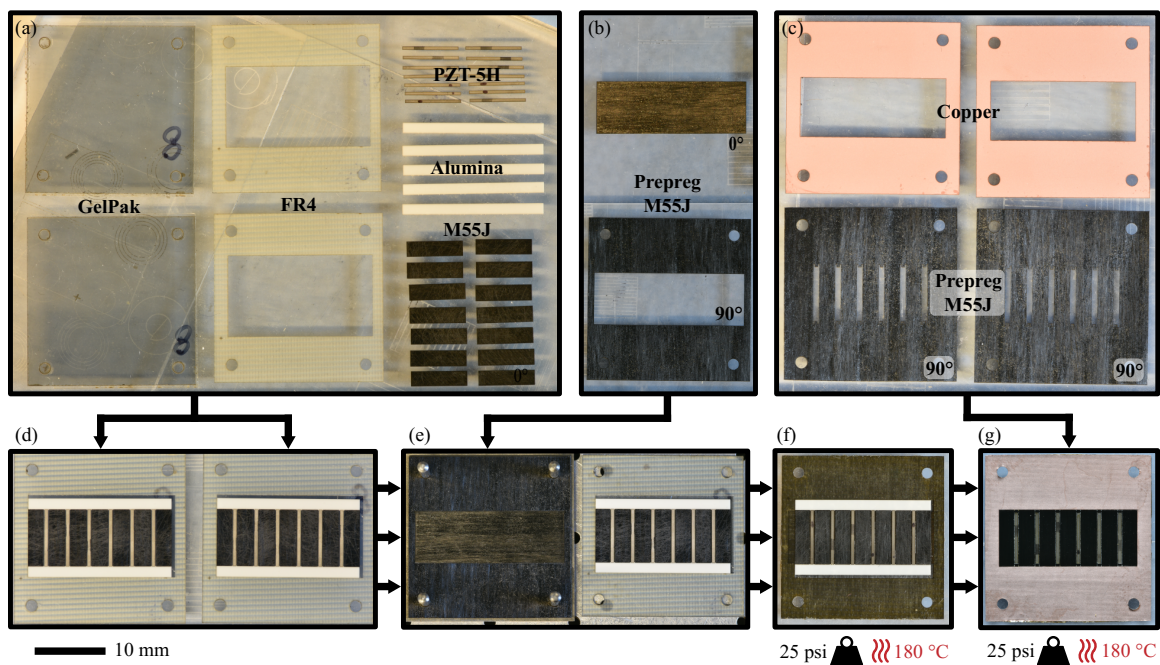


Figure 4.23: The flextensional actuators are formed from a piezoceramic/carbon-fiber/alumina laminated composite. The arrows show the process flow from the forming of raw materials (a-c) to assembly and lamination (d-g). Heat and pressure are applied in assembly steps (f) and (g). The composite thus formed contains six actuators ready to be released from the substrate.

There are a few subtle points of this lamination process that bear mentioning. First, all of the constituent materials are cut using a 355-nm 7-W pulsed laser (Coherent Avia 355-7). Because of the finite depth of field of the focusing optics, each piece has a tapered edge with taper width approximately equal to 1/10th of the thickness. Not keeping track of this taper can lead to poor lateral alignment and weak mechanical connection between the

alumina and the piezoceramic. To avoid this, I kept track of the taper direction and in the assembly shown in Figure 4.23(d) make sure to align the tapers of adjacent pieces so as to minimize the air gap between them. The use of laser micromachining also necessitates some amount of tedious cleaning; I cleaned each piece of piezoceramic after cutting (Figure 4.23a) with isopropyl alcohol using a small fabric wipe so as to remove any debris deposited on the edges. This prevents premature dielectric breakdown of the piezoceramic. Second, the use of as-fired alumina, rather than polished, and the use of sanded M55J is important to ensure strong bonding with the prepreg fibers. Sanding should be done on the bulk material before the individual pieces are formed. I found the medium roughness of papers from 240-600 grit to be appropriate. Third, small amounts of resin tend to squeeze out during lamination and build up on the edges of the stack. These can be sanded off before subsequent lamination steps. Lastly, some amount of resin will flow on top the copper layers during the final lamination step. This resin can also be removed with light sanding, or a two-ply copper can be used and the outer, resin-spotted layer peeled away to reveal a clean copper layer that is easy to solder onto.

In the next fabrication step, the actuators are released from the laminate, which is shown before release in Figure 4.24a. The process begins with the creation of the carbon fiber flexures and arms (b) using the same laser micromachining system described above. During this process, the vaporized carbon is deposited on the edges of the piezoceramic, which will lead to near instantaneous dielectric breakdown if not treated. To remedy this, I used the laser to remove these carbonized edges and create new, clean edges (c). With the laser-induced tapering in mind, these steps are undertaken symmetrically on the top and back sides, so as to ensure symmetry of the final device in the thickness direction. Next, trenches in the outer layers of carbon fiber and copper are formed to electrically isolate the connections to the different piezoelectric electrodes (d). Vias are also carefully

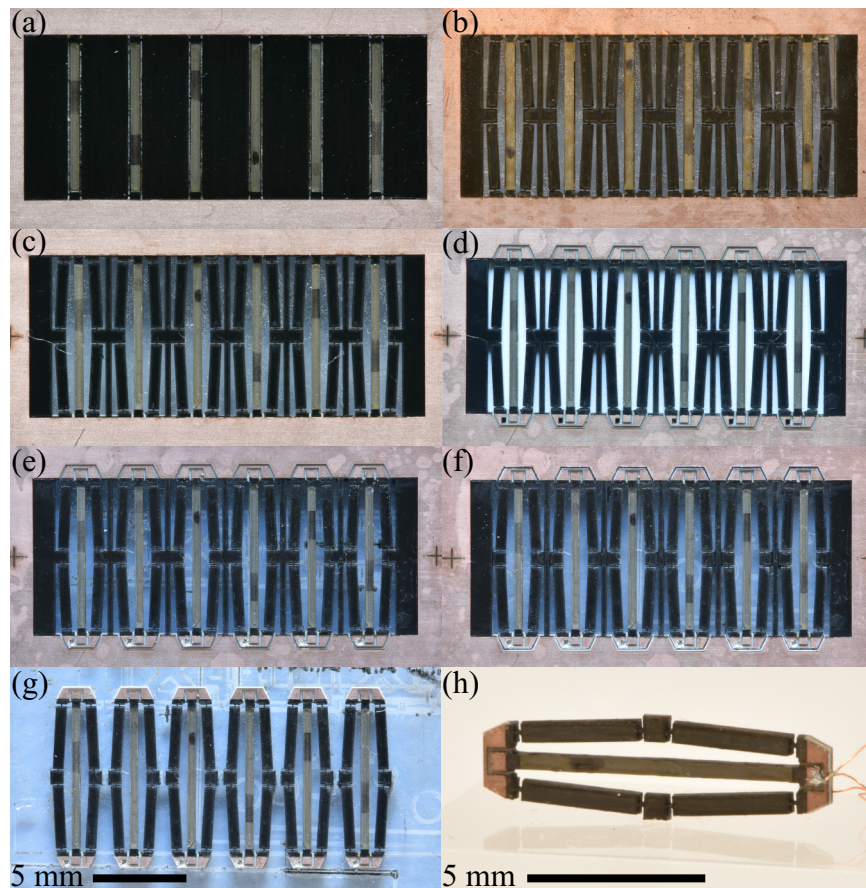


Figure 4.24: The flextensional actuators are released from the laminate using a sequence of careful laser micromachining steps. The laminate before release (a) is first registered to the laser micromachining system, and then the linkage arms are formed (b), the piezoceramic edges cleaned (c), and the vias to the center layer machined (d). The vias are then filled with conductive epoxy (e) and the outer boundaries of the actuators are defined (f). For symmetry, these cuts are then repeated on the back side of the substrate. The released actuators are shown as a set (g), and a single actuator after cleaning and wiring is shown (h).

cut through the alumina to the center carbon fiber layer, to allow electrical connection to the inner electrodes. The vias are then filled with conductive epoxy, which connects to the previously formed copper pads (e). The final laser micromachining step is the definition of the outer border to fully release each actuator from the laminate (f). Once again, this cut is done symmetrically, from the top and back sides. The excess outer material can then be discarded to reveal the released actuators (g).

Post-processing, the final fabrication step, includes a few tedious but important processes. First, The edges of the piezoceramic should be cleaned with isopropyl-alcohol-wetted cloths to remove electrically conductive debris deposited during the release cuts. This is challenging due to the small space between the piezoceramic element and the carbon fiber arms, but it can be done using a thin cloth manipulated by tweezers. It would save processing time to use a batch cleaning process or to mask off the piezoceramic edges to sidestep the need for cleaning, and these directions would certainly merit investigation if large-scale production would be pursued. Second, the edges of the piezoceramic should be treated to enhance the dielectric strength of the actuators. For small batches of actuators we have used cyanoacrylate glue (Loctite 495) and individually coated the edges using a thin tungsten wire, but for larger batches, a parallelized process such as chemical vapor deposition of parylene could be used. Lastly, electrical connections to the actuators are made. The pads are lightly sanded, cleaned with flux remover, and tinned; similarly, thin copper wires are stripped and tinned. The wires are then soldered to the pads to complete the electrical connections.

4.5.3 Modeling

Just as the design and fabrication became more sophisticated over successive iterations of devices, so did my modeling approach. Here I describe my final approach to

modeling these actuators by first reviewing existing modeling approaches in the literature:

Analytic prediction of absolute performance of flexensional actuators is a complex modeling problem that has attracted many different approaches. The simplest approach is the equivalent rigid body method, in which the torsional stiffness of the flexures and bending stiffness of the connecting arms are lumped into torsional stiffnesses acting about ideal revolute joints [52]. The next step in complexity is to treat the flexures and arms as discrete Euler-Bernoulli beams. This is the approach of Wei, et al, [59], who analyzed the general case of a compliant bridge-type mechanism and provided analytic solutions for their deformation under applied force. That approach was generalized by Ling, et al. [60], so as to cover a broader class of planar compliant mechanisms and to include the dynamics of the structure. Liu, et al. [54] used a matrix-based approach to find the equivalent compliance of the flexures at the input and output links. All of these methods discretize the structure in a way that lets the mechanism be represented with some minimal degrees of freedom. The goal of such efforts is to provide general insight to the designer without resorting to finite element analysis.

Two key themes that emerge from these modeling efforts are the sensitivity of device performance to flexure hinge width and the sensitivity of analytical models at high displacement amplification ratios. In the section that follows, I strip away most of the modeling complexity and distill these insights into quantitative design guidelines that allow a designer to size the flexure hinge width for a particular piezoelectric force and linkage amplification ratio. Unlike any of the more complex methods previously proposed, our approach does not require significant computation, numerically solving equations of static equilibrium, and the like. This should be particularly useful for those who prefer a model-light, design-by-experiments approach, for whom a loss in modeling accuracy can be compensated for with the information gained from experimental measurements.

With a view toward simple design guidelines, I use the equivalent rigid body approach, with the parameters and geometric definitions shown in Figures 4.21 and 4.25. The analysis will proceed by addressing the two extreme cases of actuator behavior: free displacement and blocked force. This allows the effects of the torsional stiffness k_t of the flexures and the compressive stiffness k_c of the linkage to be treated separately, simplifying the analysis. In the free displacement case, the torsional stiffnesses dominate, and in the blocked force case, the compressive stiffnesses dominate.

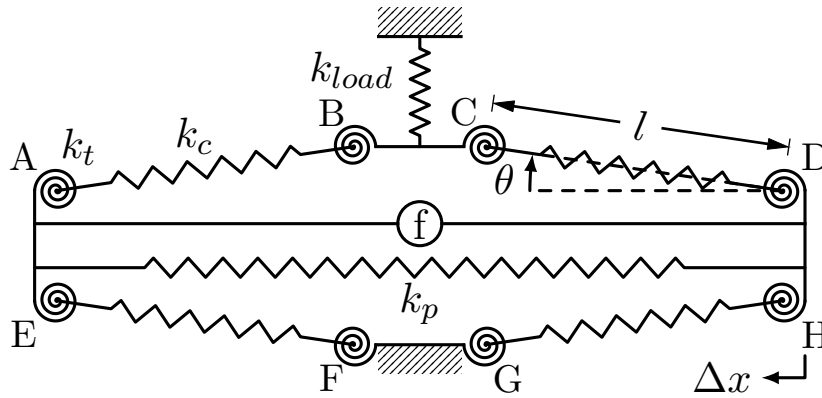


Figure 4.25: Lumped parameter representation of the piezoelectric flextensional actuator. The piezoceramic transducer is represented by a voltage-dependent force source f in parallel with a prismatic spring k_p . The flexure hinges are represented by torsional springs with stiffness k_t , and the series equivalent stiffness of each set of flexure hinges and amplification arm is represented by the prismatic spring of stiffness k_c . This simplified model grants insight into proper sizing of the amplification frame stiffness relative to the piezoceramic stiffness.

First, in the free displacement case, the torsional stiffnesses k_t of the flexure hinges are reflected back to the active element. The equivalent energy U stored in the eight flexures is equivalent to that stored in a single linear spring in parallel with the active element, as given by:

$$U = 8 \left(\frac{1}{2} k_t \Delta \theta^2 \right) = \frac{1}{2} k_{eq,t} \Delta x_p^2 \quad (4.16)$$

Where $k_{eq,t}$ is the equivalent stiffness seen by the active element and $\Delta x_p = 2\Delta x$ is the

active element's displacement. Assuming small deviations from the initial configuration, it follows from geometry that $\Delta x = l\Delta\theta \sin\theta$. Substituting this into (4.16), the equivalent stiffness $k_{eq,t}$ is found to be:

$$k_{eq,t} = \frac{2k_t}{l^2 \sin^2(\theta)} \quad (4.17)$$

Second, in the blocked force case, the compressive stiffness of the flexures and linkage arms, together represented by the lumped parameter k_c , are reflected back to the active element. The energy stored in the four linkage arms and flexures U is equivalent to that stored in a single spring in parallel with the active element, as given by:

$$U = 4 \left(\frac{1}{2} k_c \Delta l^2 \right) = \frac{1}{2} k_{eq,c} \Delta x_p^2 \quad (4.18)$$

Assuming small displacements of the structure, for this case it follows from geometry that $\Delta x = \Delta l \cos\theta$. These terms can be substituted into (4.18) to yield the following expression for the equivalent stiffness $k_{eq,c}$:

$$k_{eq,c} = \frac{k_c}{\cos^2(\theta)} \quad (4.19)$$

In the free displacement case, the motion of the active element is reduced by the factor η_u , termed “displacement efficiency” due to the parallel stiffness of the torsional hinges, such that:

$$\eta_u = \frac{k_p}{k_p + k_{eq,t}} = \frac{1}{1 + k_{eq,t}/k_p} \quad (4.20)$$

Similarly, in the blocked force case, any motion of the active element represents a reduction in the actuator's output force. The displacement of the active element Δx_p in that case is given by:

$$\Delta x_p = f_p / (k_p + k_{eq,c}) \quad (4.21)$$

“Force efficiency”, η_f , the fraction of the active element force that contributes to the output force of the actuator, can then be written as:

$$\eta_f = 1 - \frac{\Delta x_p}{u_p} = \frac{k_{eq,c}}{k_p + k_{eq,c}} = \frac{1}{1 + k_p/k_{eq,c}} \quad (4.22)$$

where $u_p = f_p/k_p$ is the free displacement of the active element.

The actuator’s output characteristics can now be written as a function of the active element properties and the linkage lumped parameters. First, the actuator’s free displacement u_a is given to be:

$$u_a = \eta_u T u_p \quad (4.23)$$

where T , the geometric transmission ratio from the active element to output link motion is simply given by $T = \cot \theta$ and u_p is the active element’s free displacement. Second, the actuator blocked force f_a can be written as:

$$f_a = \eta_f \frac{f_p}{T} \quad (4.24)$$

Now we are prepared to write the actuator’s mechanical efficiency in terms of the quantities defined above. For any actuator formed from an active element acting through a flexible transmission, the mechanical efficiency η_{mech} can be written as:

$$\eta_{mech} = \frac{u_a f_a}{u_p f_p} \quad (4.25)$$

Clearly, this represents the reduction in energy output of the actuator from that of the active material. Substituting from above, we find that mechanical efficiency can also be written simply as:

$$\eta_{mech} = \eta_u \eta_f \quad (4.26)$$

4.5.4 Scaling analysis and design guideline derivation

Now we are prepared to use the lumped parameter model to derive design guidelines for choosing geometric and material parameters. Given some minimum desired displacement and force efficiencies $\eta_{u,des}$ and $\eta_{f,des}$, respectively, two design constraints can be written using the relations above:

$$k_{eq,t} < 2k_p \left(\frac{1 - \eta_{u,des}}{\eta_{u,des}} \right) \quad (4.27)$$

$$k_{eq,c} > k_p \left(\frac{\eta_{f,des}}{1 - \eta_{f,des}} \right) \quad (4.28)$$

where the factor of two accounts for the strain stiffening of the piezoceramic, as described in [6].

We can employ the simplest torsional stiffness model for the flexure hinges, that of an Euler-Bernoulli beam:

$$k_t = 2 \left(\frac{Y_f t_f w_f^3}{12 l_f} \right) \quad (4.29)$$

The factor of two accounts for the double flexure of the parallelogram design. Under this definition I implicitly assume that the linkage arms are rigid and that all rotation occurs in the flexures. Moreover, by taking the centers of rotation of the flexure hinges to be fixed at the hinge centers, the distance between the centers l from Figure 4.25 becomes: $l = l_l + l_f$.

The lumped stiffness k_c can similarly be written in terms of geometric and material properties:

$$k_c = 2 \left(\frac{k_f k_l}{k_f + 2k_l} \right) = 2Y_f t_f \frac{w_f w_l}{w_f l_l + 2w_l l_f} \quad (4.30)$$

where k_f and k_l are the compressive stiffnesses of a single flexure and arm, respectively, and the factor of two accounts for the parallelogram structure. Note that I assume that the flexure and arm are constituted of the same material and thickness. In the same way, the

stiffness of the piezoceramic element is simply:

$$k_p = Y_p w_p t_p / l_p \quad (4.31)$$

where Y_p represents the elastic modulus in the zero strain condition.

Now, substitutions can be made to express the design constraints (4.27) and (4.28) in terms of the material properties and geometric parameters. Two cases will be considered: first, the general case in which the designer is free to choose all parameters, and second, a more restricted case in which order of magnitude assumptions are used to reduce the dimensionality of the design space to the most critical subset of design choices.

General case

When all parameters are left free to the designer, the design constraints take the form:

$$\frac{1}{6} \frac{Y_f t_f w_f^3 l_p}{Y_p t_p w_p l_f} \frac{1}{(l_l + l_f)^2 \sin^2 \theta} \left(\frac{\eta_{u,des}}{1 - \eta_{u,des}} \right) < 1 \quad (4.32)$$

$$2 \frac{Y_f t_f l_p}{Y_p t_p w_p} \frac{w_f w_l}{(w_f l_l + 2w_l l_f)} \frac{1}{\cos^2 \theta} \left(\frac{1 - \eta_{f,des}}{\eta_{f,des}} \right) > 1 \quad (4.33)$$

A few trends can be identified. Decreasing the flexure width w_f will more quickly satisfy (4.32) than violate (4.33), so all things being equal, flexure width should be decreased in order to satisfy the constraints. This is particularly necessary for small angles of θ , at which (4.32) becomes increasingly difficult to satisfy. Correspondingly, at high angles of θ , the designer is free to choose a wider flexure. Lastly, note that at some small angles of θ it is likely that no feasible choice of material properties and geometric parameters will satisfy both constraints.

Simplified case

The designer can make scaling assumptions for their specific design problem in order to cast (4.32) and (4.33) into more simplified forms. These assumptions can be drawn from manufacturing constraints and geometric scaling between parameters. A set of scaling assumptions for the millimeter-sized actuators described herein might be as follows:

1. *Constant thickness.* From the manufacturing process used (Section 4.5.2), large ratios between piezoceramic and frame thickness are difficult to achieve. We assume these to be nearly equal: $t_p \approx t_f$.
2. *Ratio-metric lengths.* To achieve reasonable absolute displacements, the linkage arms should be longer than the flexures. We can choose: $l_l = 5l_f$
3. *Ratio-metric lengths.* From geometric constraints, and assuming the length of the output link to be very small, it follows from the second assumption that: $l_p = 14l_l/5$.
4. *Localized rotation.* To ensure that bending primarily occurs in the flexure regions, the linkage arms should be much stiffer in bending than the flexures. Because the flexure and arm materials are the same, this means that:

$$\frac{l_f w_l^3}{l_l w_f^3} \gg 1 \quad (4.34)$$

By choosing $w_l = 5w_f$ I ensure that the linkage arms are $25\times$ stiffer than the flexure regions.

These assumptions yield the following simplified constraints:

$$\frac{343}{27} \frac{Y_f w_f^3}{Y_p l_p^2 w_p} \frac{1}{\sin^2 \theta} \left(\frac{\eta_{u,des}}{1 - \eta_{u,des}} \right) < 1 \quad (4.35)$$

$$\frac{28}{3} \frac{Y_f w_f}{Y_p w_p} \frac{1}{\cos^2 \theta} \left(\frac{1 - \eta_{f,des}}{\eta_{f,des}} \right) > 1 \quad (4.36)$$

These relations should be useful in the scenario in which a designer is given a piezoceramic element, amplification frame material, and nominal transmission ratio and wants to select a flexure size without resorting to cumbersome modeling methods that require computing forces and displacements in the entire structure.

This can be challenging to achieve in devices in which piezoceramics are employed, due to their high stiffness. The temptation for the designer is to add material to the frame to bulk it up, but this erodes actuator performance in terms of how efficiently it uses its mass or volume. This motivates the use of mass efficiency as a quality metric, defined as:

$$\eta_{mass} = \frac{m_{p,active}}{m_{act}} \quad (4.37)$$

Taken together, mass and mechanical efficiency can be used to define actuator energy density in terms of energy density of the bulk material.

$$D_{act} = \eta_{mech} \eta_{mass} D_p \quad (4.38)$$

4.5.5 Results

The design enhancements described in Section 4.5.1 yield an increase in mechanical efficiency from 33 % to 70 % from the Gen. II to Gen. V actuators, as shown in Table 4.4. The fourth generation is similar to the third, except the amplification arms are split into the

parallelogram structure that reduces the serial compliance seen between the active element and the load. The fifth generation is similar to the fourth, except the flexure geometry is chosen in accordance with the scaling analysis conducted in Section 4.5.4. The target efficiencies were $\eta_{u,des} = 76\%$ and $\eta_{f,des} = 91\%$, chosen somewhat arbitrarily to simulate a real design scenario, and the achieved efficiencies were 88% and 79% , respectively. This small deviation is likely due to some small unmodeled compliance in the frame and uncertainty in the material parameters.

The most significant trend that can be seen in Table 4.4 is an increase in blocked force from generation to generation while free displacement stays relatively constant. The third through fifth generations, which employ two active elements and alumina base attachments, all have significantly higher blocked force than the first or second generations. The small differences in blocked force and free displacement seen in the third through fifth generations are due primarily to different flexure geometry and amplification frame topology and in part to the slightly larger active elements employed.

To elucidate these trends and provide clarity to the derived values, a detailed description of the tabulated Figures is merited. First, the length and width of the active elements and the linkage geometry were measured using a confocal microscope (Olympus OLS 4000). The measured values were largely as designed, with some small variations due to the evolution and refinement of the manufacturing process. Inadvertently, half of the flexures on the second generation device were made slightly elongated from the others, which was resolved for subsequent generations. The active element thickness was simply measured using a micrometer. The piezoelectric coefficients d_{31} and $f_{31,block}$ were taken from previous experimental work [6]. Note that these values are significantly higher than typical values reported by manufacturers, which are given for low field operation. The free displacement u_p and blocked force F_p of the active element were calculated from its geometry and material

model, i.e.,:

$$u_p = d_{31}El_p \quad (4.39)$$

$$F_p = f_{31,block}Et_p w_p \quad (4.40)$$

where E , the applied electric field, is $1.5 \text{ V}/\mu\text{m}$ for all tabulated values. For the first and second generations, data is as reported in Section 4.3 and Section 4.4, respectively. For the third through fifth generations, free displacement was measured using a high-zoom inspection camera (PixeLINK PL-B741F), with resolution of 1.6, 2.77, and $2.4 \mu\text{m}/\text{pixel}$ for the respective measurements. Blocked force was measured using a load cell (ATI Nano17 Titanium) with a resolution of 1.5 mN. The actuators were weighed using an electrobalance (Cahn 25). Lastly, bandwidth, defined as the f_{+3dB} frequency, was measured using a laser Doppler vibrometer (Polytec PSV-500).

Lastly, I conducted a series of experiments to validate the constancy of the output stiffness across a range of load stiffnesses and operating conditions. Springs of various stiffness were placed between the load cell and the output link of the actuator, and output force and displacement were measured simultaneously (displacement was measured with the inspection camera, as before). These experiments were conducted on a Gen. III actuator. The results are shown in Figure 4.26, and it can be seen that output stiffness is nearly constant at $\sim 2.75 \text{ N}/\text{mm}$, with some nonlinear effects becoming visible at high fields.

4.5.6 Discussion

The millimeter-sized flexensional actuators described herein compare favorably to existing centimeter-sized designs. The most mechanically efficient actuator seen in the literature is that of Janker, et al. [51]. Their centimeter-scale actuator uses an aluminum






		Gen. I	Gen. II	Gen. III	Gen. IV	Gen. V
						
Piezo. active element						
number		1	1	2	2	2
length \times width [mm]	l_p, w_p	8.00×1.5	8.00×0.43	7.40×0.41	7.44×0.425	7.44×0.425
bridge length [mm]	l_b	0.25	0.4	0.3	0.28	0.28
thickness [μm]	t_p	135	135	135	135	135
d_{31} [pm/V]		544	544	544	544	544
$f_{31,block}$ [Pa m/V]		26	26	26	26	26
free displacement [μm]	u_p	6.5	6.5	6.0	6.1	6.1
blocked force [N]	f_p	7.90	2.26	4.32	4.48	4.48
total active mass [mg]		12.64	3.62	6.39	6.66	6.66
Amplification frame						
base connection		FR4	UD CF	alumina	alumina	alumina
topology		single arm	single arm	single arm	parallelogram	parallelogram
linkage angle [$^\circ$]	θ	1.9	3.35	3.4	3.4	3.4
flexure width [μm]	w_f	70	20	30/20	30	60
flexure length [μm]	l_f	150 (eff.)	110 (eff.)	60/90	60	480
arm width [μm]	w_l	300	490	560	340	350
arm length [mm]	l_l	3000	3500	3300	3300	2500
Actuator performance						
free displacement [μm]	u_a	115	86	90.5	83.8	89.6
blocked force [mN]	f_a	20	57	191	211	211
mass [mg]		24.9	7.6	16.0	17.5	16.8
bandwidth [kHz]		-	1.1	1.6	-	2.1
Performance metrics						
mass efficiency [%]	η_{mass}	51	48	40	38	40
mechanical efficiency [%]	η_{mech}	4.5	33	66	65	70
disp. efficiency [%]	η_u	59	74	89	82	88
force efficiency [%]	η_f	0.8	42	75	79	79

Table 4.4: Comparison of multiple generations of millimeter-sized piezoelectric flextensional actuators showing the increase in mechanical efficiency arising from the incorporation of alumina base connections, parallelogram amplification topology, and proper selection of flexure geometry across designs generations. Note that the piezoelectric coupling coefficients are given for an applied field of $1.5 \text{ V}/\mu\text{m}$.

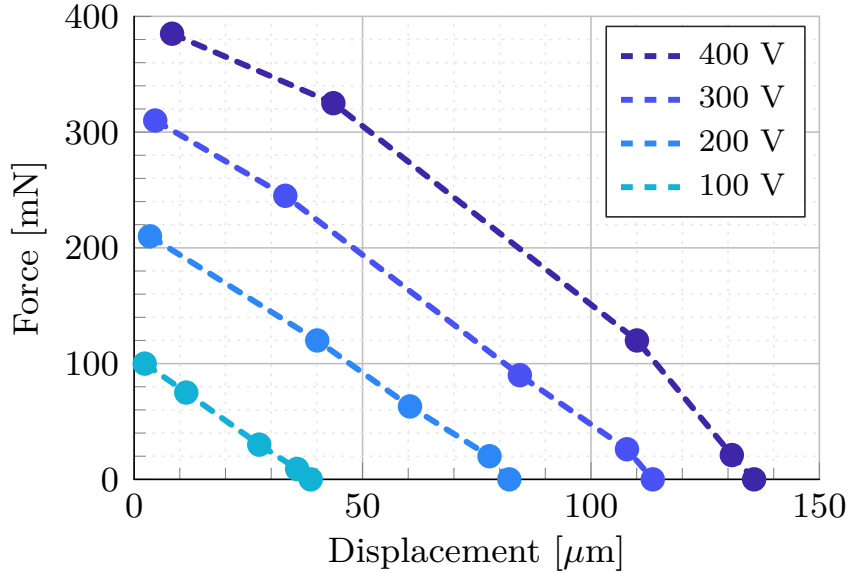


Figure 4.26: Static performance of the Gen. IV design with a purely compliant load, across a range of input voltages and load stiffnesses. Output stiffness is nearly constant at low fields and varies slightly at high fields. A maximum energy density of 1.5 J/kg is achieved at 400 V.

frame with the parallelogram topology and achieves 83% mechanical efficiency at 33% mass efficiency, compared to 70% mechanical efficiency and 40% mass efficiency for the Generation V actuator.

The actuators presented in this work also compare favorably to other millimeter-sized piezoceramic actuator topologies. Of particular interest are bimorph bending actuators, which are widely used in microrobotic devices. For a similarly sized bimorph beam ($L \times W = 8.2 \text{ mm} \times 2 \text{ mm}$), the free displacement and blocked force of the active element are $6.7 \mu\text{m}$ and 10.6 mN , respectively, and the free displacement and blocked force of the actuator are $375 \mu\text{m}$ and 115 mN , respectively. This yields a mechanical efficiency of 61%. The mass efficiency is the mass of the active elements (34.6 mg) divided by the total mass (43 mg)–80%. Thus, the energy density achievable with the flextensional actuators is about 60% of the energy density of bimorphs. This could perhaps be further increased through

incorporation of lighter passive materials and more exacting design optimization.

The most deficient aspect of these actuators is their dependence on the mechanical bridges to transfer force from the active element to the amplification frame. The bridges are in tension, and, while they are much stiffer than the piezoceramic elements, their bonds to the frame and piezoceramic, respectively, must be able to resist the shear force generated by the contracting piezoceramic. Unfortunately, it is difficult to guarantee high quality bonds due to the small bond area and variable quality of prepreg carbon fiber. A better approach might be to prestretch the amplification frame around the active element, such that it always is in compression. In such a scheme, contraction of the active element would work to relieve the tension in the frame. Importantly, force transfer would no longer rely on the quality of the mechanical bridges.

The lumped-parameter-based scaling analysis could be extended in a variety of ways. It could be adapted to incorporate more sophisticated representations of rotational stiffness beyond the beam-bending approach taken here. It could also be generalized to more complex structures—any in which the work of an active element is transformed through a compliant mechanism.

4.6 Summary

I have herein described a series of new flextensional millimeter-sized piezoelectric actuator designs with high mechanical efficiency (70%) and energy density (1.5 J/kg). Mechanical efficiency is an important quality metric, as it captures how well the flexible transmission converts the input work to output work. I have shown that to optimize mechanical efficiency it is useful to think in terms of equivalent stiffnesses. Moreover, by focusing on the extremes of actuator behavior—blocked force and free displacement—anal-

ysis can be simplified and simple design guidelines derived with the assistance of simple scaling assumptions. These actuators expand the possibilities for millimeter-sized robotic devices, and the methods proposed should be broadly useful for designers of similar devices across all scales.

Chapter 5

Robotic Laser Steering: Centimeter-scale Device

5.1 Introduction

I first encountered the concept of a robotic surgical laser manipulator in the work of Alperen Acemoglu and Leonardo Mattos at the Italian Institute of Technology. My discovery of this work came at the same time that I was repairing the galvanometer on the one of the lab's laser laser cutters, which started me thinking about what would be needed to build a galvanometer in miniature using the PC-MEMs techniques.

I had a worthy partner in this work, Simon Bothner, a visiting student from EPFL. He contributed the device design and conducted much of the prototyping for this device, details of which can be found in the paper we published on the subject [61]. This chapter is thus relatively brief; herein I will describe the clinical background and motivation, state of the art, our system concept (which I provided), as well as modeling and results from experiments, which I led.

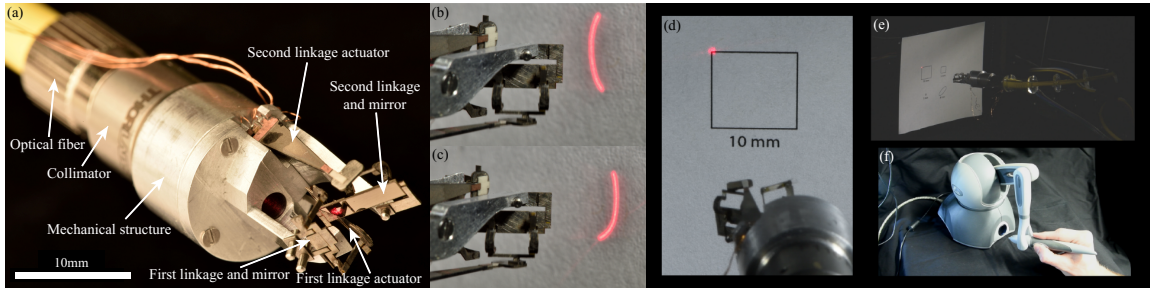


Figure 5.1: Centimeter-scale laser steering system integrating focusing optics and articulable mirrors: (a) Prototype device; (b-c) Long exposure images of laser trajectory; (d-f) Laser steering system deployed under teleoperation.

5.2 Clinical background: vocal fold surgery

Over 30,000 people in the U.S. were diagnosed in 2018 with a cancer of the pharynx or larynx [62], resulting in 6,000 deaths. These cancers are notable for their deleterious effect on quality of life; their symptoms, including dysphagia and voice impairment, often lead to depression and social isolation, and curative treatments often exacerbate these functional maladies [63]. Incidence, historically driven by the smoking of tobacco, is increasingly driven by human papillomavirus, resulting in a historically young patient population even more concerned with long-term functional outcomes [64].

Thus, there is significant need for curative treatment methods for these cancers that enable post-treatment organ function. Partial or full organ removal via open surgery represents one extreme: the near guarantee of excellent oncological results at the expense of functional outcomes. Nonoperative methods, including induction chemotherapy, intensity modulated radiotherapy, and concurrent chemotherapy with radiotherapy, offer better functional outcomes than open surgery while achieving good oncological results. Such techniques are currently recommended for most laryngeal cancers [65]. However, within the last two decades, the perceived long-term morbidity and functional impairment associated with radiotherapy have led some otolaryngologists to reexamine surgical techniques [66]. Mini-

minimally invasive methods are of particular interest, with a view toward greater preservation of healthy tissue and associated improvements in post-operative organ function relative to open surgery.

Transoral laser microsurgery (TLM), first described in 1972 [67], is the most mature minimally invasive approach. In TLM, a carbon dioxide laser is coupled to a surgical microscope and aimed through a laryngoscope, which provides line-of-sight access to the upper airway. The surgeon uses manual tools inserted through the laryngoscope to retract the lesion and uses a micromanipulator on the microscope to steer the laser beam to resect the diseased tissue. In advanced systems, the micromanipulator is motorized, allowing the surgeon to direct the laser along predetermined arcs and lines at precisely controlled speeds, resulting in very high quality incisions [68]. The most significant limitation of TLM is its line-of-sight constraint, which restricts both visualization and exposure. Moreover, the long, narrow laryngoscope makes the manual manipulation of tools required for retraction and suturing difficult.

To address these shortcomings, transoral robotic surgery (TORS) was developed in the mid 2000s [12, 69]. In TORS, flexible or wristed robotic manipulators are used in conjunction with endoscopic vision systems, providing superior visualization and tissue manipulability at the surgical site. The da Vinci multi-port and da Vinci single port systems (Intuitive Surgical Inc, Sunnyvale, CA) and the Flex Robotic System (Medrobotics, Raynham, MA, USA) are currently in clinical use [70].

However, TORS remains deficient to TLM in at least one key respect: in TORS, electrocautery is primarily employed for resection, which leads to greater post-operative pain and longer recovery times than in similar procedures conducted with TLM [71]. With the recent development of hollow core fibers capable of delivering carbon dioxide lasers through flexible instruments, the use of lasers in TORS is expected to increase [72], which

should mitigate this problem to some degree. However, fiber-based lasers must be held and manually manipulated by robotic tools, and thus lack the spatial repeatability, precision, and speed of free-beam scanning systems. This implies that incision quality suffers relative to the free-beam systems used for TLM. Free-beam systems have the additional benefit of leaving the surgical site clear for exposure and visualization of margins.

Thus, there is an opportunity to capture the benefits of both TLM and TORS, by creating a laser scanning system that operates at the end of a robot manipulator. This configuration would enable more precise incisions and tighter margins than achievable with existing laser or electrocautery tools. Moreover, by moving the laser fiber inside the robot manipulator, it may be possible to relax some of the constraints on the fiber’s design and use; currently available CO₂-laser fibers are expensive (around \$1000) and single-use. In the proceeding sections, we will describe a prototype device for enabling this TLM/TORS hybrid paradigm.

5.3 State of the art

A number of prototype endoscopic devices have been developed for minimally invasive laser scanning tasks, each with a different approach to the challenging design problem. I describe each below, highlighting the tradeoffs inherent to each design and providing absolute numbers when possible:

1. M. Zhao, T. J. O. Vrieling, A. A. Kogkas, M. S. Runciman, D. S. Elson, and G. P. Mylonas, “LaryngoTORS: A novel cable-driven parallel robotic system for transoral laser phonosurgery,” *IEEE Robotics and Automation Letters*, vol. 5, no. 2, pp. 1516–1523, 2020

This recent work from the HARMS Lab at the Hamlyn Centre at Imperial College

reports a cable-driven approach to manipulate a laser fiber. This approach to robotic laser steering is attractive for its simplicity, but the achievable laser speed is very low (3 mm/s); also, I do not believe that this approach will scale well to the millimeter-scale. Their current version is quite large: ($22 \times 20 \times 22$ mm).

2. A. Acemoglu, D. Pucci, and L. S. Mattos, “Design and control of a magnetic laser scanner for endoscopic microsurgeries,” *IEEE/ASME Transactions on Mechatronics*, vol. 24, no. 2, pp. 527–537, 2019

This is one of many in a series of publications on magnetic-coil-based laser scanning from the Biomedical Robotics Lab at the Italian Institute of Technology. In their approach, external coils manipulate the angle of a laser fiber via permanent magnets arrayed around the fiber. This approach is attractive for its simplicity and robustness, but there are pernicious trade-offs between range-of-motion, bandwidth, and device size based on the size of the coils and permanent magnets. Their device achieves a range of motion of 3×3 mm and speed of 94 mm/s at 30 mm working distance.

3. R. Renevier, B. Tamadazte, K. Rabenorosoa, L. Tavernier, and N. Andreff, “Endoscopic laser surgery: design, modeling and control,” *IEEE/ASME Transactions on Mechatronics*, vol. 22, no. 1, pp. 99–106, 2017

The FEMTO-ST Institute in France developed this system that uses off-the-shelf piezoelectric linear actuators to articulate a silicon mirror held on a tip-tilt stage, which achieves a sizeable 20×20 mm field of view but relies on an unwieldy external mirror to reflect back on to the tip-tilt stage. Also, the device is boxy and quite large because of its use of off-the-shelf components ($9 \times 11 \times 42$ mm).

4. O. Ferhanoglu, M. Yildirim, K. Subramanian, and A. Ben-Yakar, “A 5-mm piezo-

scanning fiber device for high speed ultrafast laser microsurgery,” *Biomedical Optics Express*, vol. 5, no. 7, pp. 2023–2036, 2014

This group from University of Texas used piezoelectric actuators to directly bend an optical fiber, achieving a high laser speed (500 mm/s at 3.5 mm working distance) in a thin device profile (5 mm diameter), but the field of view ($250 \times 250 \mu\text{m}$) is extremely small as a result. In applications in which this set of properties is desired, this seems like a reasonable approach. An important tradeoff is that range of motion is strongly related to device length – the device must be long enough to allow space for the optical fiber to bend. The length of this device is 40 mm.

5. S. Patel, M. Rajadhyaksha, S. Kirov, Y. Li, and R. Toledo-Crow, “Endoscopic laser scalpel for head and neck cancer surgery,” in *Photonic Therapeutics and Diagnostics VIII*, vol. 8207, p. 82071S, International Society for Optics and Photonics, 2012

This group from the Memorial Sloan-Kettering Cancer Center in New York City used DC motor-driven Risley prisms as the beam steering method to achieve moderate scanning speeds (471 mm/s) and a large field of view (75 mm diameter) at 75 mm working distance, but the device is quite bulky (17 mm diameter) and uses rotary transmission components that are challenging to further miniaturize.

6. N. Yamanaka, H. Yamashita, K. Masamune, T. Chiba, and T. Dohi, “An endoscope with 2 dofs steering of coaxial nd: YAG laser beam for fetal surgery,” *IEEE/ASME Transactions on Mechatronics*, vol. 15, no. 6, pp. 898–905, 2010

This device from the University of Tokyo transmits a laser beam through a rigid endoscope using a lens relay system. The beam is steered using a conventional galvanometer before it is coupled into the device. It is focused using an objective lens system at the end of the scope. This is an intriguing approach that achieves

a large range of motion ($\pm 11^\circ$ and $\pm 12^\circ$) in its two controllable axes. Putting the steering components at the distal end of the device nicely works around some of the challenges of miniaturization, but it is unlikely that this approach would work for flexible tools.

5.4 System concept

In our approach, shown assembled in Figure 5.1a and schematically in Figure 5.2, we leverage the PC-MEMs manufacturing techniques to create miniature mechanical transmissions that convert the quasi-linear motions of high-bandwidth piezoelectric bending actuators [6] into rotational motions that are used to orient mirrors. Our device contains two such actuator-transmission-mirror combinations, situated orthogonally, such that the two actuation inputs correspond to ablation in orthogonal directions on the target tissue. Light is transmitted to the laser scanner using an optical fiber and then fed into a collimating and a focusing lens assembly. The focused beam is then steered by rotating the two mirrors using crank-slider transmissions to convert the linear actuator movement to the desired rotational mirror movement. The scanning base provides a mechanical ground for the actuators and the transmissions and guarantees precise alignment between the optical subsystem and the mirror subsystem.

5.5 Modeling

Given the mirror angles determined by the crank-slider kinematics, the laser spot location on the target plane can be found using the vector formulation of specular reflection. Symbols and geometric definitions used are given with the system schematic shown in

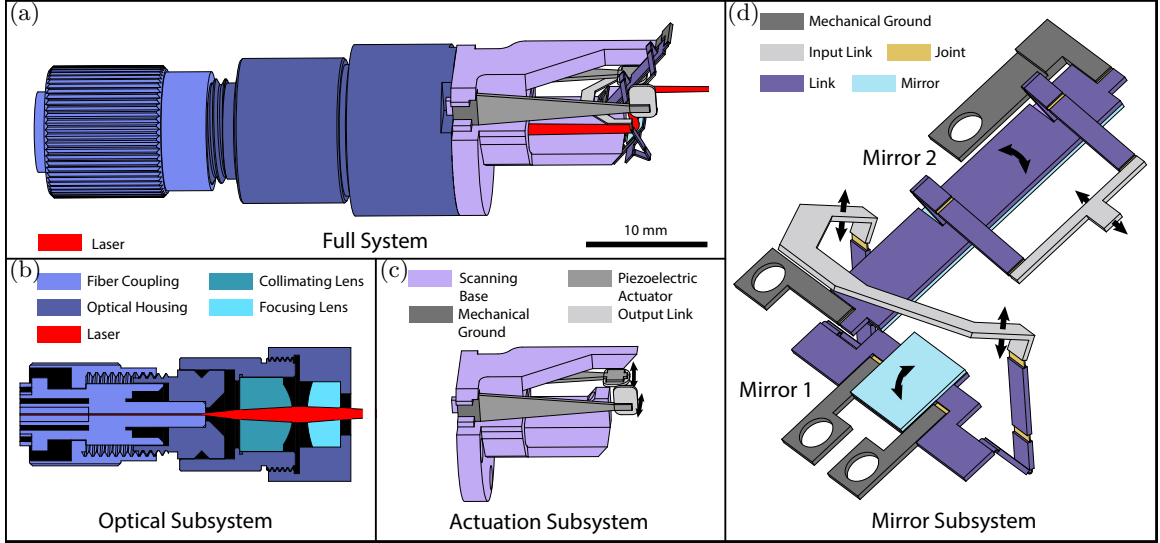


Figure 5.2: (a) 3D drawing of the laser-scanning end effector defining the location of key subsystems. (b) Optical subsystem, which connects a fiber optic source to the laser scanner. (c) Actuation subsystem, consisting of piezoelectric bending actuators and a rigid mechanical base that aligns the optics with the rest of the device. (d) Mirror subsystem containing motion transmissions and flat mirrors.

Figure 5.3. The orientations of the mirrors in 3D space are given by:

$$R_1^w = R_{z, \theta_1 + \theta_{1,0}} \quad (5.1)$$

$$R_2^w = R_{z, (\theta_{1,0} - \pi)} R_{y, -\pi/2} R_{z, \theta_2} \quad (5.2)$$

Where $\theta_{1,0}$ is a design variable denoting the initial orientation of the first mirror. Now, the ray reflected from the first mirror has direction:

$$\hat{v}_{12}^1 = H_2^1 (R_1^w)^{-1} e_2^w \quad (5.3)$$

And it intersects the second mirror after a distance d_{12} :

$$d_{12} = (o_2 - o_1)^T e_2^w / (R_1^w \hat{v}_{12}^1)^T e_2^w \quad (5.4)$$

Symbol	Description
$e_j^i \in \mathbb{R}^3$	The j th basis vector of the i th coordinate system.
$\hat{v}_{jk}^i \in \mathbb{R}^3$	The unit vector directed from point p_j to point p_k , with respect to the i th frame.
$R_j^i \in SO(3)$	The orientation of the j th coordinate system with respect to the i th coordinate system.
$R_{i,\theta} \in SO(3)$	Elementary rotation about the i axis by angle θ .
H_j^i	Householder transformation about the j th basis vector of the i th coordinate system, expressed in local coordinates.

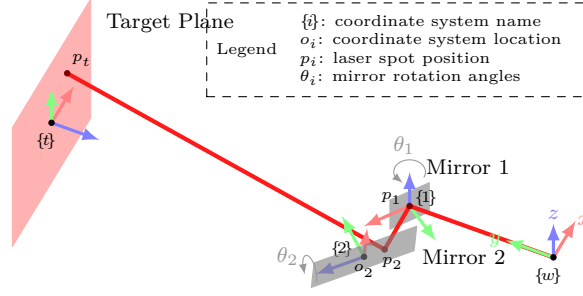


Figure 5.3: Diagrammatic representation of laser scanning system with key symbols defined.

Thus, the location of the laser on the second mirror is given by:

$$p_2^w = \begin{bmatrix} R_1^w & p_1^w \\ 0 & 1 \end{bmatrix} \begin{bmatrix} d_{12} \hat{v}_{12}^1 \\ 1 \end{bmatrix} \quad (5.5)$$

Similarly, the reflected ray from the second mirror has direction:

$$\hat{v}_{2t}^2 = H_2^2 (R_2^w)^{-1} R_1^w \hat{v}_{12}^1 \quad (5.6)$$

And intersects the target plane after a distance d_{2t} :

$$d_{2t} = (o_t - o_2)^T e_3^t / (R_2^w \hat{v}_{2t}^2)^T e_3^t \quad (5.7)$$

Finally, p_t^w , the location of the laser spot on the target plane is given by:

$$p_t^w = \begin{bmatrix} R_2^w & p_2^w \\ 0 & 1 \end{bmatrix} \begin{bmatrix} d_{2t} \hat{v}_{2t}^2 \\ 1 \end{bmatrix} \quad (5.8)$$

5.6 Results

In order to find safe bounds on input drive frequency, I conducted frequency analyses on both actuator-transmission-mirror subsystems. Data were collected under low-voltage white noise input using the Polytec PSV-500 laser Doppler vibrometer. The results are shown in Figure 5.4; as expected, both subsystems closely resemble second-order linear systems. The resonant frequencies of 850 Hz and 750 Hz accord with physical intuition: the free-beam resonance of the actuators (~ 1.6 kHz) has been reduced due to the added mass of the transmission.

To validate the beam steering capabilities of the device, I created a benchtop scanning arena incorporating a calibrated high-speed camera (Phantom v710) with a 200 mm macro lens and two non-flicker flood lights, all mounted on an optical table. The camera view is shown in Figure 5.4 along with the grid used for image registration. One pixel corresponds to $50\ \mu\text{m}$ in the image plane. We fixed our device on the optical table at our determined stand-off distance of 20 mm from the target.

We then calibrated the scanner by sweeping the voltage space and tracking the laser spot position. The overall field of view matches the model prediction well, as shown in Figure 5.4. However, unmodeled compliance in the system and assembly misalignment created a slight scaling of the laser task space. Rather than adding extra degrees of freedom to our model and calibrating it, we chose to use a lookup-table approach for controlling the laser spot position.

This approach yields reasonable results for task-space trajectory following, as shown in Figure 5.5. Three shapes, an “H”, a “star”, and a Lissajous figure, were drawn across a range of speeds. Each shape is shown at a base speed of 100 mm/s and at the highest speed that it could be reproduced before oscillations in the transmissions erode the

device’s tracking performance. Such oscillations emerge at 2 m/s in the “H” trajectory. Of the three shapes, the “H” is the most challenging due to the rapid, abrupt changes in the trajectory. The Lissajous figure is simplest, because the drive voltages on the actuators are smooth and nearly sinusoidal and thus suffer little loss in performance up to 7 m/s.

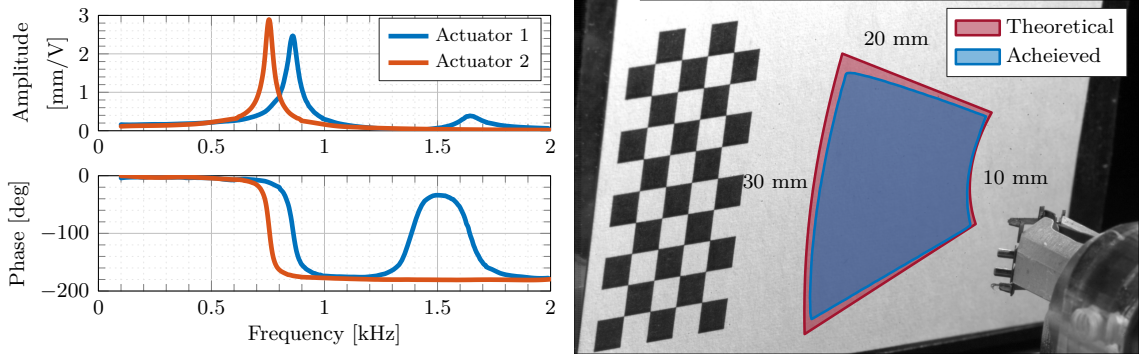


Figure 5.4: (Left) Frequency response of the actuator-transmission-mirror subsystems. Measurements were taken at the tips of the actuators. (Right) Laser spot position tracking setup, as viewed from the high speed camera. Theoretical and achieved field of view from a 20 mm standoff distance are shown.

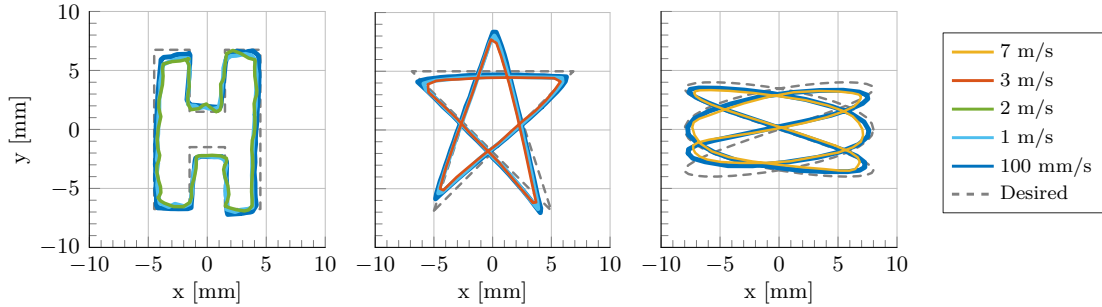


Figure 5.5: Shapes drawn at different speeds demonstrate the open-loop trajectory following capabilities of the laser scanner. The high-speed performance of the system is shown through its repeatability across a range of commanded velocities.

5.7 Discussion

The most significant errors in the trajectory following experiment occurred during vertical motions. Given the orientation of the device during those experiments, these motions were mostly generated by the second mirror. This is consistent with the insight that the second linkage transmission, as conceived in this device, is slightly overconstrained because the linkage joint axes are not orthogonal to the plane in which the actuator tip displacement lies. Thus, the configuration of the linkage is determined by kinetics rather than kinematics. This is ameliorated in the next generation device shown in Chapter 6. Hysteresis is also not compensated for and is certainly a source of error between the commanded and achieved trajectories.

Chapter 6

Robotic Laser Steering: Millimeter-scale Device

6.1 Introduction

This tool builds on the lessons learned in the development of the centimeter-scale tool. Its miniaturization, using the centimeter-scale device as a reference, is enabled by: (1) the use of smaller off-the-shelf optical components and some custom machined parts; (2) parallelized packaging that uses space more efficiently, which makes the device significantly shorter; (3) the use of a fixed mirror, which allows the two controllable mirrors to be placed more closely together. A comparison of the properties and performance of the two devices is shown below in Table 6.1. The millimeter-scale device itself is shown in Figure 6.1

An important contribution of this work is the development of a new modular design approach that allows the device to be easily assembled and disassembled, which allows for rapid testing, debugging, and development. This approach uses rigid stainless steel rails as assembly guides for the optical and mechanical components, which are placed on disks

	Centimeter-scale	Millimeter-scale
Diameter [mm]	15	6
Length [mm]	45	16
Fiber Connection	FC Connector	Ferrule
Collimator type	Plano-convex	GRIN
Focusing lens	OTS plano-convex	In-house plano-convex
Mirror type	Sputtered Al	Sputtered Al
# of mirrors (controllable/fixed)	2/0	2/1
Focal distance [mm]	20	25
Range of motion [mm]	18 x 10	18 x 18
Mechanical bandwidth [Hz]	750	1800

Table 6.1: Comparison of centimeter and millimeter-scale laser steering tools in size, composition, and performance.

that slide onto the rails. Secondary contributions include several advancements in device control: transmission mechanics that enhance device repeatability; hysteresis compensation that improves open-loop trajectory control; and finite jerk profiling of control inputs to improve the smoothness of response.

6.2 Results

Principle of operation A compact collimating lens collects light from a ferrule-terminated optical fiber and directs it into a miniature plano-convex focusing lens. The light is reflected by a 45° angle-of-incidence mirror and into a miniature two-mirror galvanometer. Each mirror is driven by an independent piezoelectric bending actuator acting through a flexible linkage.

Drive scheme The piezoelectric bending actuators are driven in the biased unipolar configuration with a fixed bias voltage of 200 V. Thus, each actuator is controlled by a single time-varying input signal ranging from 0 to 200 V. This input range achieves a large output displacement while ensuring that the tensile strain in the piezoceramic is well below

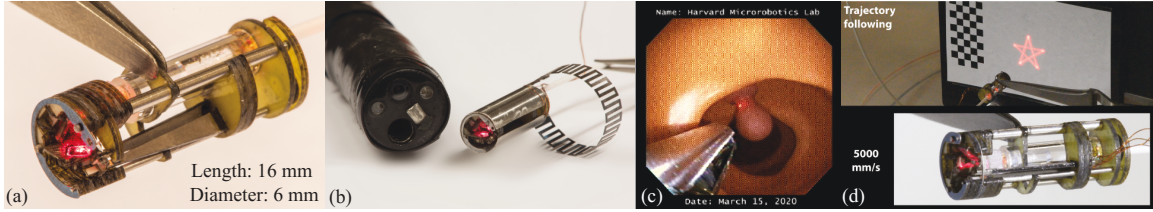


Figure 6.1: Millimeter-scale surgical laser steering system. (a) Close-up of device made from a mix of off-the-shelf and custom fabricated components. (b) Encapsulation of device and attachment to a colonoscope. (c) Scope view inside a colon tissue simulator with laser steering device attached and in view. (d) Long-exposure photograph showing the quality of high-speed trajectory following.

the failure limit. Under these drive conditions, the actuators achieve free displacement of $\pm 200 \mu\text{m}$ and have first resonant frequency of 2.6 kHz.

Kinematics The linkages were designed to achieve at least $\pm 10^\circ$ of motion for each mirror under the chosen input range. There are two key considerations: (1) the transmission ratio of the linkage and (2) the stiffness of the linkage relative to that of the actuators. Based on experience sizing similar mechanical components, I chose a target transmission ratio of $0.1^\circ/\mu\text{m}$ and target stiffness equal to that of the actuators. In the device, I achieved transmission ratios of $0.11^\circ/\mu\text{m}$ and $0.13^\circ/\mu\text{m}$ and stiffnesses of three-fifths and nine-tenth the actuator stiffness, respectively. This yields the ranges of motion -14.5 to 16.5° and -12.0 to 12.0° for the two mirrors, respectively.

Repeatability Open-loop repeatability is an important metric because it describes the fundamental limitations of the device physics to reproduce identical motions. Stiction, plasticity, and other phenomenon ensure that identical inputs do not produce identical outputs. Unidirectional repeatability is a measure of repeatability in which measurement points are only approached from one direction. Measurement results are shown in Figure 6.2. The maximum 2σ standard distance of the sampled points is $200 \mu\text{m}$, which means that one

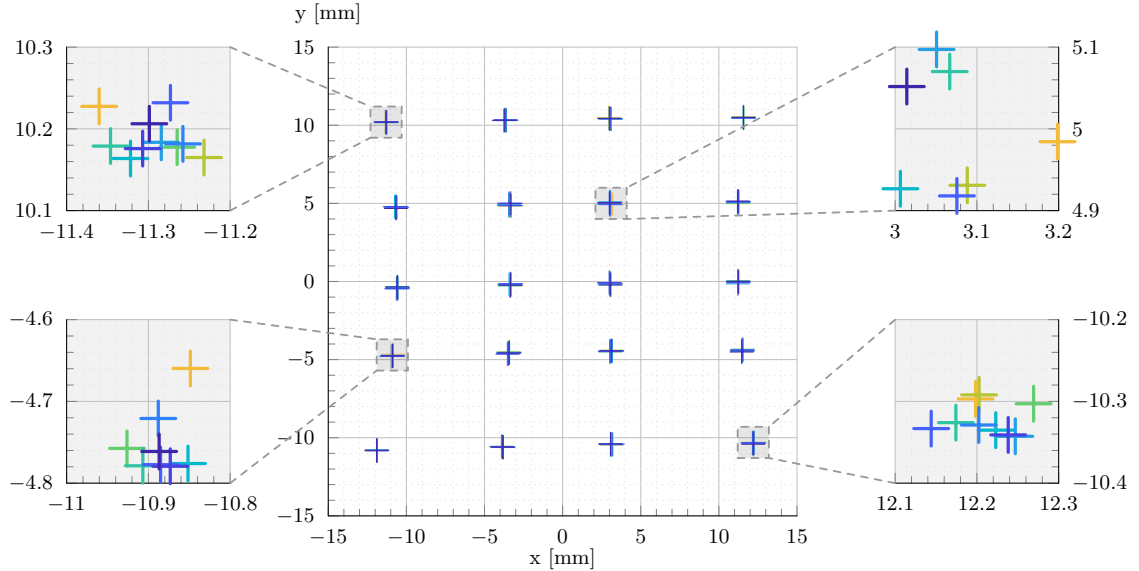


Figure 6.2: Laser position repeatability. Measurements were taken to quantify the unidirectional repeatability of the laser system throughout its workspace. Zoomed-in plots show detail for selected points. The maximum 2σ standard distance of the sampled points is $200\ \mu\text{m}$, which means that there is 95% confidence that a set of repeated inputs will fall within a $200\ \mu\text{m}$ radius of dispersion about the mean.

has 95% confidence that any series of identical movements will fall within a $200\ \mu\text{m}$ radius of dispersion about the mean trajectory.

Calibration Because of the low dimensionality of the workspace and input space and the lack of sensor information, I chose to calibrate the device using a direct model-free mapping between actuator input and laser spot position. I fit third and second degree polynomial surfaces to the the open-loop repeatability measurement data for the first and second mirrors, respectively. These fits were centered around 73 V and 93 V, respectively, which correspond to the actuation inputs that align the output beam along the longitudinal axis of the device.

Workspace By inverting this mapping and applying input commands at 3 mm intervals, I generated the “calibrated workspace” shown in Figure 6.3. The average error between the

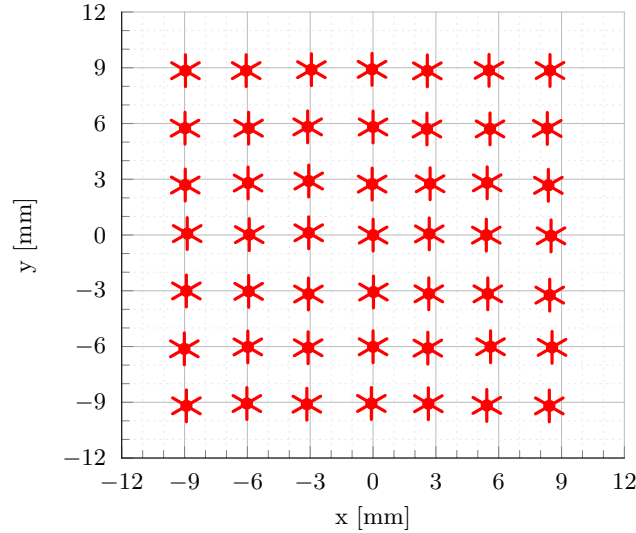


Figure 6.3: Calibrated workspace. This is the open-loop response of the calibrated device to position commands given in 3 mm increments.

commanded inputs and measured points is $300\ \mu\text{m}$, with standard deviation of $250\ \mu\text{m}$.

Hysteresis compensation Hysteresis arises from domain reorientation inside the piezoceramic actuator, the result of which is that the laser position for a single set of control inputs depends on the time history of the input. This is clearly undesirable because it complicates control and makes use of the device unintuitive. To minimize the hysteretic effects, I implemented a feed-forward compensation scheme described at length in Section 6.5. Briefly, I first captured displacement response data for a bare bimorph actuator for two amplitude-rich input conditions as shown in Figure 6.8a-b. This is a standard approach for capturing the effects of hysteresis throughout the input space. By remapping the measured data to the same range as the input space and inverting the relationship, I arrive at a relationship that can be used for feed-forward control. These curves are shown in Figure 6.8c-d. I then commanded the star trajectories shown in Figure 6.4 for uncompensated and compensated inputs. The raw inputs clearly show the effects of path dependence,

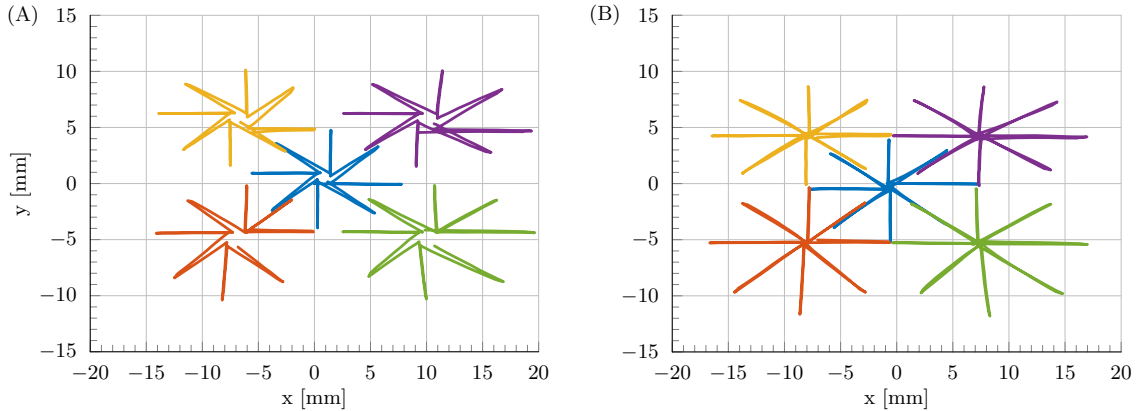


Figure 6.4: Setpoint regulation. (A) Laser spot position is shown without hysteresis compensation. (B) Laser spot position for the same trajectory with the addition of compensation, which yields dramatic improvement in the quality of the control and largely removes the hysteretic effects.

while the corrected inputs show significantly better tracking. Quantitatively, we find that the maximum 2σ standard distance around the setpoints is 2.14 mm without compensation and 0.72 mm with compensation. This is reasonable improvement for feed-forward compensation; further improvement can be achieved with feedback control.

Bandwidth The bandwidth of the system is limited by oscillation of the mirrors at high frequencies. The primary resonant frequencies for the two mirrors are 1.8 kHz and 1.9 kHz, as can be seen in the Bode plots shown in Figure 6.5A-B. Additionally, there is a lower frequency mode at 1.2 kHz on the first mirror. To avoid exciting these modes, we use a finite jerk motion profiling scheme.

High-speed trajectory control The system shows only minor deviation from static trajectories at high speeds, as can be seen in Figure 6.5C-D. There is only 5% deviation between the trajectories followed at low (10 mm/s) and high (5000 mm/s) speeds. Also, because of the two-axis control, the system can trace complex planar trajectories, as shown in Figure 6.5E-F.

Multi-modal control The large bandwidth in the system can also be exploited to generate multi-modal profiles. These are trajectories in which a high frequency input is superimposed onto a low frequency one.

Colonoscope interfacing Because of the low-profile and small mass of the laser steering device, it can be readily interfaced with existing surgical tools. To demonstrate this, we attached it onto the end of a colonoscope and performed a simulated polyp resection task on a benchtop surgical simulator. Snapshots of this are shown in Figure 6.1.

6.3 Design

In order to miniaturize the device, the challenge is to make the distance between the mirrors as small as possible, given the beam size, mirror size, and desired range of motion, while avoiding collisions between the mirrors and unwanted collisions between the reflected beam and previous mirrors in the optical path. These considerations can be visualized with the help of Figure 6.6, first looking at the three-mirror design. If the distance between the first and second mirrors is too small, then the reflected beam from the third mirror will intersect the first mirror, as is almost the case for the left-most sample configuration. If the distance between the second and third mirrors is too small, then those mirrors will collide, as is almost the case for the center sample configuration. Increasing the distance between mirrors not only increases device size, but also means that larger mirrors are needed to collect the reflected light. The three-mirror design shown in Figure 6.6 balances all of these considerations to yield a device with $\pm 10^\circ$ range of motion on each active mirror in a 4 mm diameter footprint. Note that the use of chamfered corners on the mirrors increases the range of motion by preventing collisions in critical locations.

Using fewer mirrors does not, counter-intuitively, lead to a smaller device size,

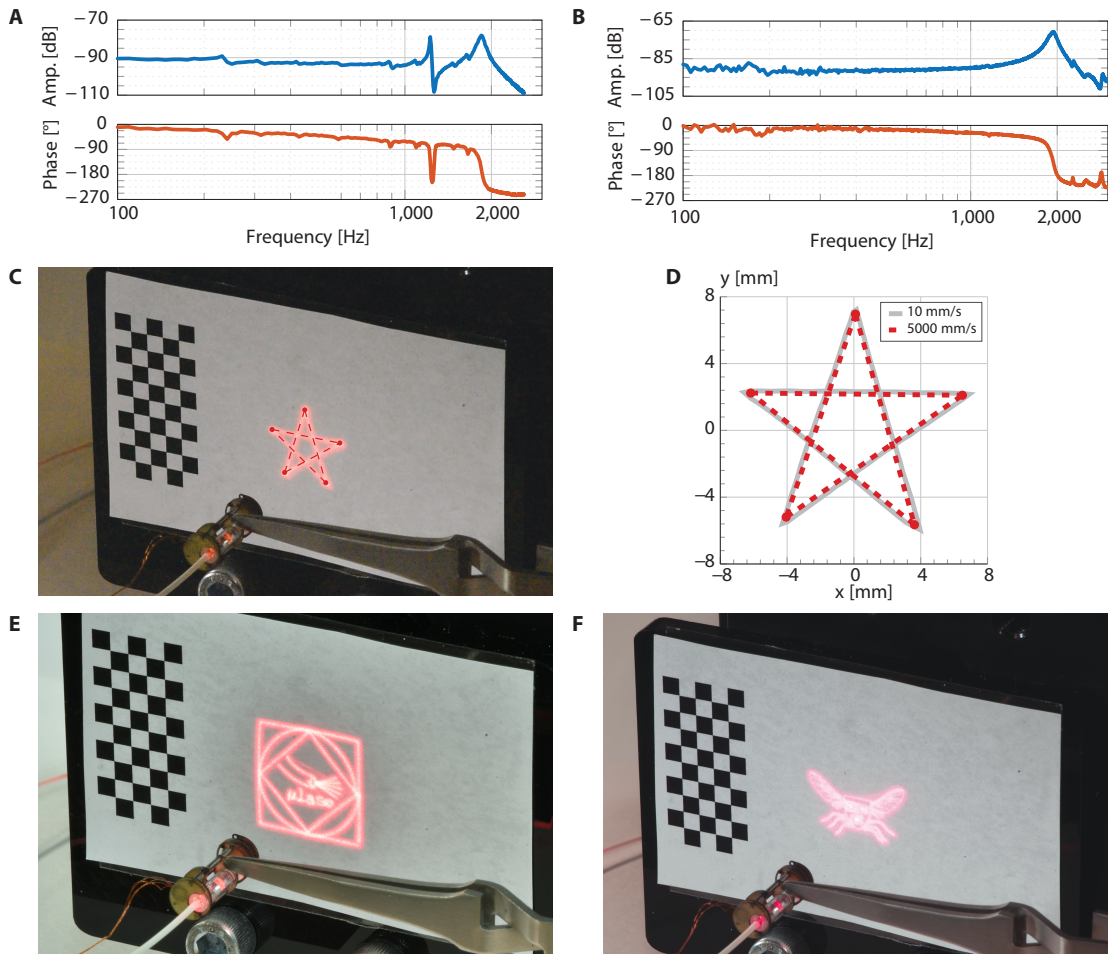


Figure 6.5: **High-speed control.** (A) First mirror frequency response to low-voltage white noise input. (B) Second mirror frequency response. (C) An image created by high-speed motion of the laser steering system. (D) The high-speed image closely matches the trajectory followed by the laser system at low speeds. There is only 5% deviation between the two trajectories, despite a difference in speed of 500 \times . (E-F) Complex images captured through long-exposure photography that demonstrate the system's intricate control capabilities.

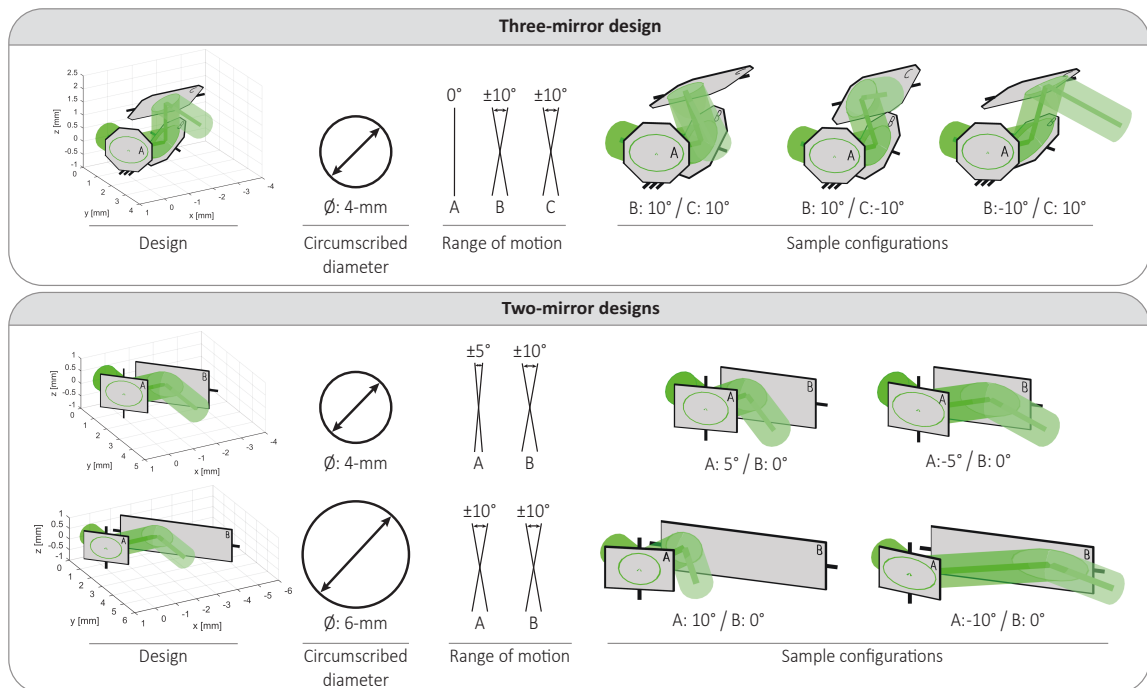


Figure 6.6: Miniature galvanometer design. The three-mirror galvanometer achieves a larger range of motion than a two-mirror design of the same size. A 50% larger two-mirror design is needed to achieve the same range of motion as the three-mirror design. Range of motion is primarily determined by the ability of the mirrors to fully capture and reflect the incident light, but it is limited by the need to avoid collisions between mirrors in addition to collisions between the reflected laser and previous mirrors in the optical path. Sample configurations show the limits of the range of motion at which these collisions are about to occur.

if the same range of motion is desired. The first two-mirror design shown in 6.6 has the same diametral footprint as the three-mirror design but its range of motion is halved on the first mirror axis. An insidious set of trade-offs leads to this result: if the mirrors are too close together, then the beam reflected from the second mirror will intersect the first mirror for large positive rotation angles of the first mirror. This is the case shown in the left-most sample configuration. On the other hand, if the distance between the two mirrors is increased, then the second mirror will have to be very wide to accept the incident light from the first mirror for large negative rotation angles of the first mirror. This leads to the second two-mirror design shown in 6.6. It achieves the same range of motion as the three-mirror design, but at the expense of a 50 % increase in diameter.

Throughout this analysis I assumed a beam diameter of 1 mm. This is somewhat larger than the low-power pointing laser I used for device validation, but it is a reasonable size to assume for a collimated high-power beam, for which this system is ultimately intended to use. For simplicity, I also chose the neutral position of each mirror to yield a 45° angle of incidence with the incoming beam; allowing this to slightly fluctuate might yield slightly different results but would not change the structure of the design tradeoffs. I also assumed that a symmetric range of motion is desired. Once again, if this were not the case, then the resulting design might change slightly, but the nature of the design space would not change. Lastly, it should be emphasized that I have been considering the case of the exiting ray being parallel to the incoming fiber. If one wanted the exiting ray to be perpendicular to the incoming fiber, there would be no reason to use a three-mirror design; a two-mirror design would be perfectly acceptable in terms of miniaturization and range of motion.

Another small point of differentiation between the three and two-mirror designs is the shape of the focal plane. Because the distance the laser travels through the three-mirror design changes very little with mirror angle, the focal plane is nearly symmetric about the

neutral configuration. This is not the case for the two-mirror designs; the distance the laser travels between the mirrors changes drastically from configuration to configuration. This yields a deformed focal plane that is contracted for large negative values of the first mirror rotation angle, as was seen in the workspace of the centimeter-scale design.

6.4 Fabrication

The device consists of a set of modular components placed on disks that are sequentially assembled onto a steel-rod superstructure. These components are made from a mixture of custom-made and off-the-shelf components and primarily formed using laser micromachining. Each component is shown in assembly order in Figure 6.7. Specific details for component constitution, fabrication, and function are as follows:

1. **Steel-rod superstructure.** This superstructure consists of two 500 μm and one 300 μm diameter stainless steel rods (Misumi USA) onto which the remaining components are assembled. The rods are orthogonally located into a FR4 disk using an alignment jig. A spring steel preload spring to compress and hold the assembled components in place is attached to the disk. All components were laser micromachined.
2. **Ferruled fiber and collimating lens.** An off-the-shelf ferrule-terminated optical fiber was assembled with a GRIN collimator and attached to an FR4 support disk.
3. **Piezoelectric bending actuators.** These were made to size using the in-house process described in [6].
4. **Collimator support disk.** This provides lateral stabilization and alignment to the collimator assembly.
5. **Focusing lens.** This was acquired as an off-the-shelf component and ground down

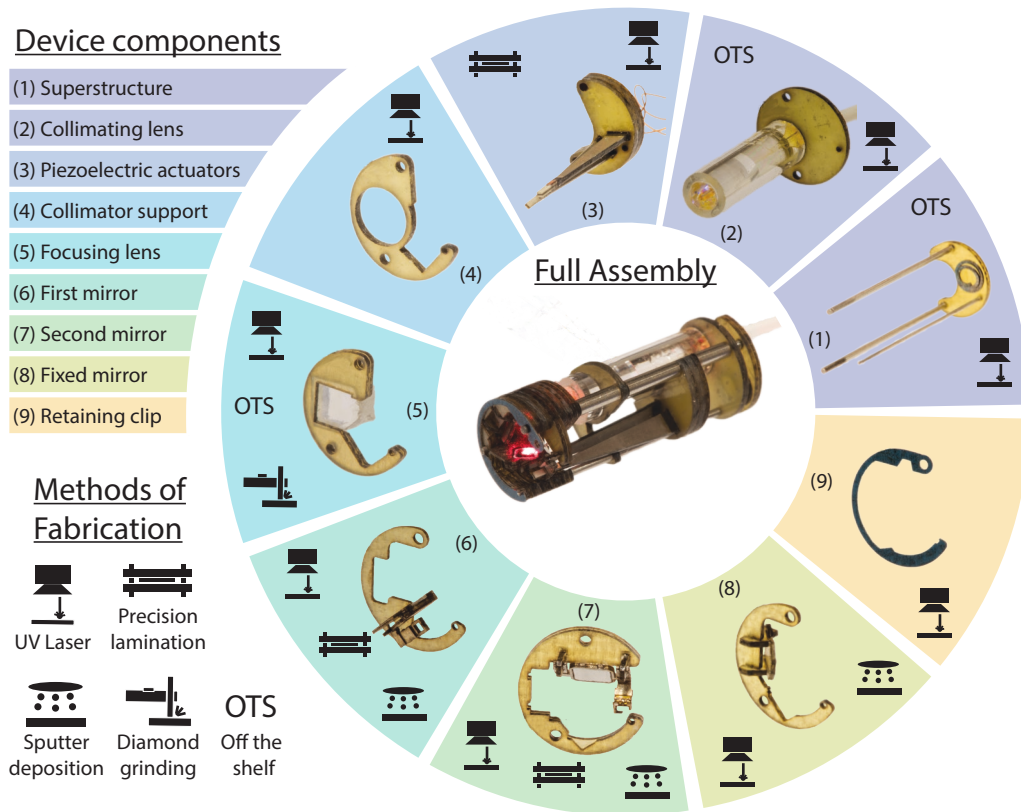


Figure 6.7: Device components and fabrication. The key components of the laser steering device are shown in assembly order from the superstructure to the retaining clip. The icons in each sector show the methods of fabrication used for making each component.

to size using an alignment jig and a diamond cut-off wheel. Registration marks laser pre-engraved into the lens allow alignment of the optical center after grinding.

6. **First articable mirror.** This is a complex assembly of rigid and flexible components fabricated using PC-MEMs. It consists of a four-bar linkage driven by a linearizing connecting rod that interfaces with one of the piezoelectric actuators. The mirror is made from sputtered aluminum on a 100 μm fused silica substrate.
7. **Second articable mirror.** This consists of a four-bar crank-slider linkage. The mirror is located on the crank and the slider interfaces with one of the piezoceramic

actuators. The mirror is also made from sputtered aluminum on fused silica. The mirrors are singulated using a UV laser. The crank interfaces with an FR4 support disk via two alignment blocks that set the neutral angle of the mirror to be at 45° relative to the disks.

8. **Fixed mirror.** This aluminum-sputtered fused silica mirror is fixed at 45° relative to the incident light using two alignment blocks that in turn interface with an FR4 support disk.
9. **Retaining clip.** This spring-steel component fits onto grooves rastered into the stainless steel rods of the superstructure.
10. **Spacer tubes and disks.** The pieces are laser micromachined to ensure proper spacing and alignment between components.

6.5 Hysteresis compensation

Hysteresis is often modeled with the differential Bouc-Wen model, which describes hysteresis as a nonlinear, time-dependent stiffness that is the weighted sum of displacement and a non-observable internal state variable. This internal state variable is governed by a nonlinear ordinary differential equation that incorporates information about the direction of motion and the direction of the input signal. This approach is attractive for its generality in encompassing a wide range of hysteretic behaviors, termed “softening”, “hardening”, “pinching”, etc. It also has several extensions to account for multiple degrees of freedom as well as asymmetry. Hysteresis is also often modeled through the use of a set of polynomial basis functions or through parallelized lumped-parameter units. Regardless of the modeling method chosen, the object is typically the same: to invert the model and use it as a feed-forward correction term to reduce the physical effects of hysteresis in the device.

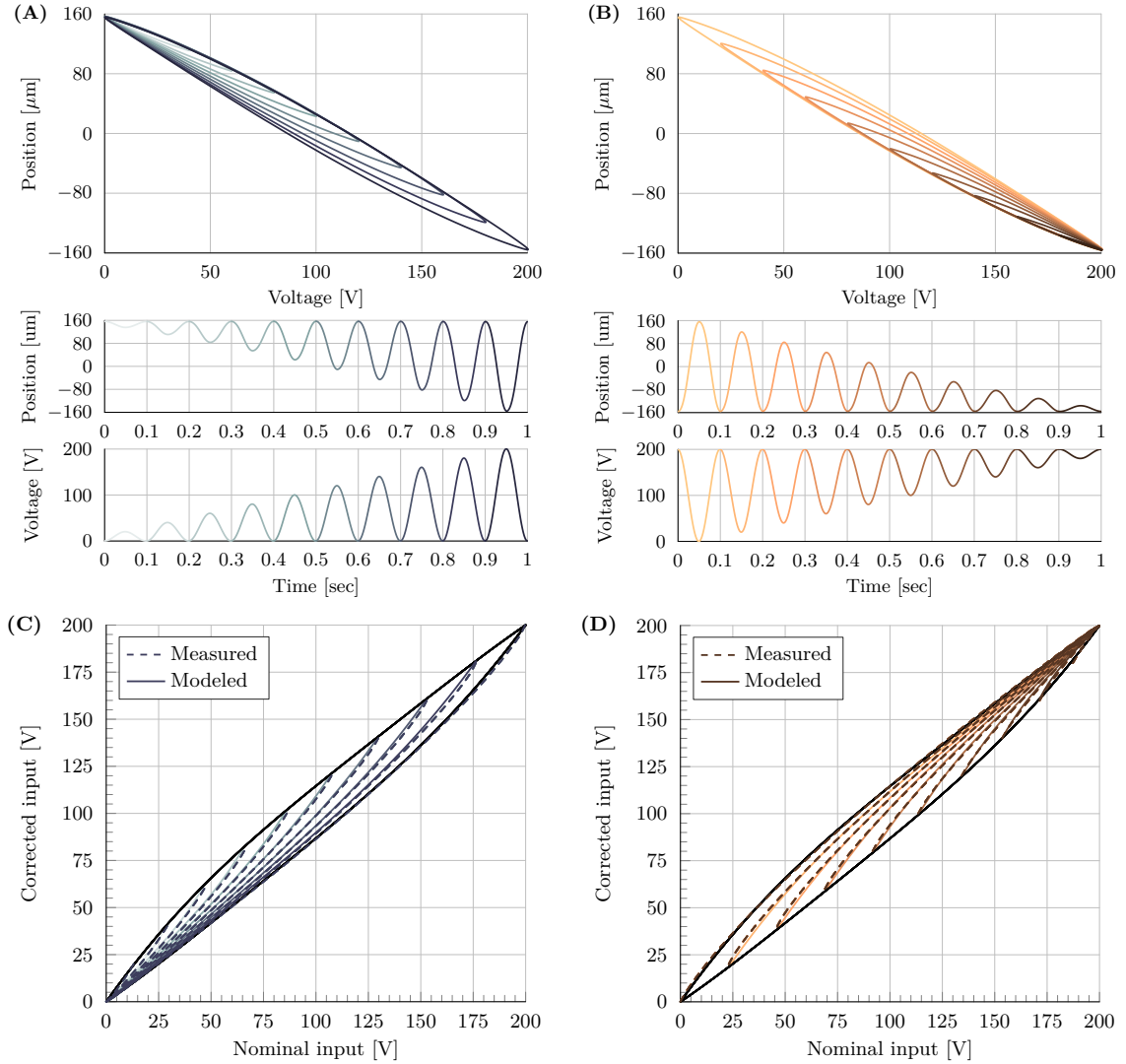


Figure 6.8: Hysteresis measurement and model fitting. (A-B) Actuator position in response to amplitude rich input voltages is measured and plotted. The applied and measured signals are also plotted versus time. These curves are scaled and inverted to yield the solid curves shown in (C-D), which are plotted alongside the modeled behavior on the dashed curves.

From the measurements taken, it is apparent that the hysteresis in our system is mathematically simple— the position to voltage relationship is nearly linear and the internal hysteresis patterns are regular in shape and spacing. This is likely due to the symmetry of the bending actuator structure and the fact that the device is operating at low input fields. Because of the simplicity of the hysteresis shape, I determined the Bouc-Wen model

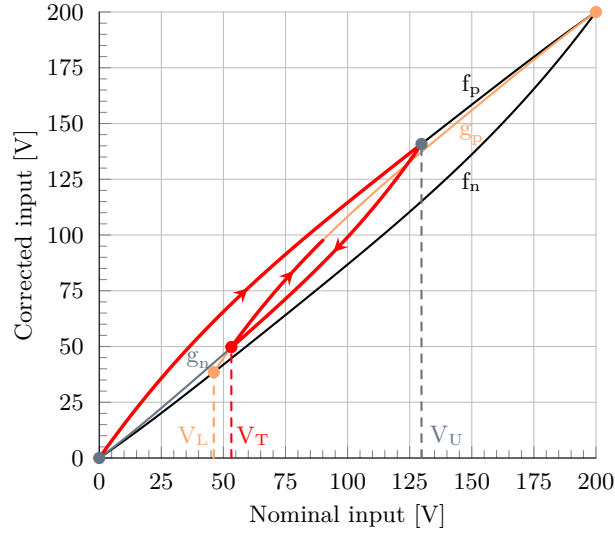


Figure 6.9: Hysteresis modeling with key functions and parameters. The outer envelope is defined by the curves f_p and f_n , and the inner family of curves are defined by g_p and g_n . The subscript denotes the sign of the input rate (positive or negative). A sample input trajectory is shown in red: the nominal input starts at the origin and rises to V_U ; it then reverses direction along the curve g_n defined by the anchor point at V_U ; last, at level V_T the nominal input voltage increases again and starts moving along the curve g_p defined by knot point V_L .

to be overly cumbersome and developed a new low-dimensional hysteresis representation, inspired by existing polynomial basis-function approaches.

My approach is to treat each curve as a quadratic-weighted sine function. The outer curves (the hysteretic envelope) have knot points at 0 and 200 V, and the inner curves have knot points at either 0 or 200 V and at a point on the opposite outer curve. These knot points set the period and amplitude of the sine curve, and the quadratic deforms the sine function to match the measured data. The coefficients of the quadratic can be written for the outer curves and scaled appropriately for the inner curves due to the symmetry in the system. Because of the constraint on amplitude, only two coefficients of each outer curve can be independently chosen. Thus, with this representation, one has four parameters to tune: two each for the positive and negative going curves. For each curve, one parameter

determines the scaling of the curve and the other parameter determines its shape. This approach well-captures the rate-independent hysteretic behavior and is intuitive to implement and tune.

Implementation of this approach is as follows, using Figure 6.9 as a visual guide.

The outer curves f_p and f_n are defined as:

$$f_p(V) = V_{max} (a_p(V - h_p)^2 + k_p) \sin(\pi V / 2V_{max}) \quad (6.1)$$

$$f_n(V) = V_{max} + V_{max} (a_n(V - h_n)^2 + k_n) \sin(\pi (V - V_{max}) / 2V_{max}) \quad (6.2)$$

where V_{max} is the maximum excursion of the input voltage. In our case, $V_{max} = 200$ V, but I will leave the expressions in the more general form. Note that these expressions have knot points at $(0,0)$. To guarantee that they also have knot points at (V_{max}, V_{max}) , one can write a_p as a function of h_p and k_p :

$$a_p = \frac{1 - k_p}{(V_{max} - h_p)^2} \quad a_n = \frac{1 - k_n}{h_n^2} \quad (6.3)$$

Note that k_p and k_n will control the size of the hysteresis loops and h_p and h_n will control the shape. In anticipation of scaling these curves, I rescale h_p and h_n using the relations:

$$h_p = l_p V_{max} \quad h_n = l_n V_{max} \quad (6.4)$$

Now, using the above definitions, the inner curves can be defined as follows:

$$g_p(V, V_L) = f_n(V_L) + V_{amp} (a_p(V - h_p)^2 + k_p) \sin(\pi (V - V_L) / T) \quad (6.5)$$

$$g_n(V, V_U) = f_p(V_U) + V_{amp} (a_n(V - h_n)^2 + k_n) \sin(\pi (V - V_U) / T) \quad (6.6)$$

For g_p , in order to ensure that the inner curves scale appropriately in size and shape, I choose:

$$\begin{aligned} V_{amp} &= V_{max} - f_n(V_L) & T &= 2(V_{max} - V_L) \\ h_p &= l_p V_{max} + (1 - l_p)V_L & a_p &= \frac{1 - k_p}{(V_{max} - h_p)^2} \end{aligned} \quad (6.7)$$

Similarly, for g_n , I choose:

$$\begin{aligned} V_{amp} &= f_p(V_U) & T &= 2V_U \\ h_n &= l_n V_U & a_n &= \frac{1 - k_n}{h_n^2} \end{aligned} \quad (6.8)$$

When the input changes sign, we want to switch from a positive-going curve to a negative one, or vice versa. The transition point between the curves is denoted V_T , and to determine which new curve to transition onto, one solves the nonlinear root-finding problem:

$$g_p(V_T, V_L) - g_n(V_T, V_U) = 0 \quad (6.9)$$

for the unknown variable (either V_L or V_U). In other words, the current value of V_L or V_U tells us which curve we are on, and when we change the sign of the input, our first step is to look for a new V_L or V_U . With this in hand, one can calculate the desired feed-forward correction factor for the current nominal input voltage.

Using this approach, the measured curves are fit to the parameters: ($k_p = 0.81, l_p = 0.5, k_n = 0.80, l_n = 0.53$), as shown in Figure 6.8c-d. In practice, the loading from the hinged transmissions slightly deforms these curves; for *in situ* hysteresis compensation, we used a tuned set of parameters ($k_p = 0.82, l_p = 0.5, k_n = 0.75, l_n = 0.608$).

6.6 Experimental setup and procedures

Laser position measurements Laser position data were collected using a Phantom v710 high-speed camera at 1200 x 800 pixel resolution with an AF Micro-Nikkor 200mm f/4D IF-ED macro lens. The camera has a maximum frame rate of 7500 fps at full resolution. Lighting was provided from two low-flicker LED lights (Zaila, Nila, Inc.). The results of the camera calibration are shown in Figure 6.10. Reprojection errors for the image set are less than 0.2 pixel (10 μm), and the extrinsics estimates reasonably correspond to the physical measurement setup. Sub-pixel reprojection error means that the camera calibration well-captures the physics of the measurement setup and means that camera calibration is an only minor source of measurement error. Larger contributors are likely to be differences in lighting and marker detection. The measurement resolution in the camera orientation used for data collection Figure 6.10 was 46 $\mu\text{m}/\text{px}$ and 51 $\mu\text{m}/\text{px}$ in the world x and y directions, respectively.

Kinematics I measured the relationship between actuator displacement and mirror angle for the entire input space in 20 V increments using a high-zoom inspection camera (Pixel-link). The resolution of the measurement system was 2.5 $\mu\text{m}/\text{px}$.

Repeatability I undertook unidirectional repeatability measurements using the standard for single-axis motion control systems (ISO 230-2). Under these guidelines, I measured 20 different points in the laser workspace 10 times each, for a total of 200 data points. For each measurement, the system was powered off and reset, so as to eliminate the influence of hysteretic effects. A typical data set of 20 points is shown in Figure 6.11; this image contains all 20 sampled points superimposed onto a single image. The centroids of the points were calculated using MATLAB's blob analysis tool.

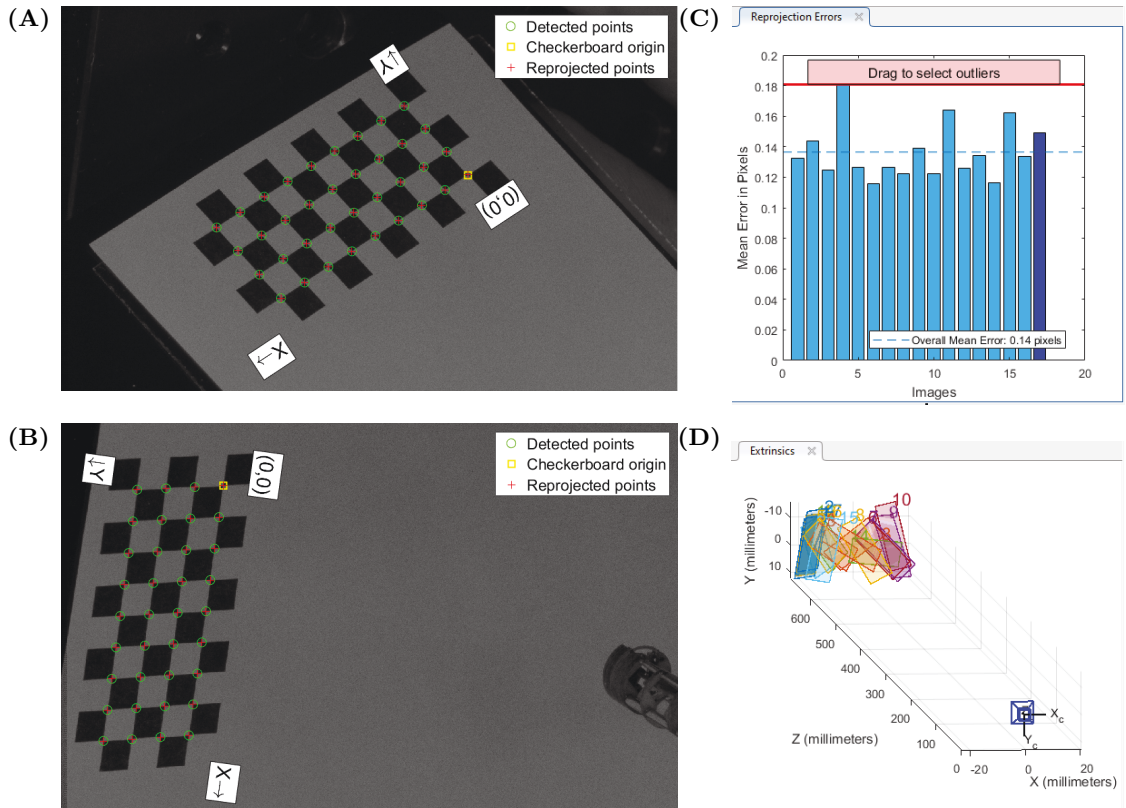


Figure 6.10: Camera calibration inputs and results. A set of 17 images were used for the calibration, two of which are shown in (A) and (B). Reprojection error (C) and extrinsics (D) are also shown.

Bandwidth and actuator performance The frequency responses of the bare actuators and the mirrors in the assembled device were measured using a laser Doppler vibrometer (Polytec PSV-500). The static displacement of the bare actuators were measured using the same system.

6.7 Discussion

The millimeter-scale device represents a substantial improvement over the centimeter-scale version in terms of size, design, and control. This device is small enough to be integrated with existing transoral robotic tools or onto flexible scopes.

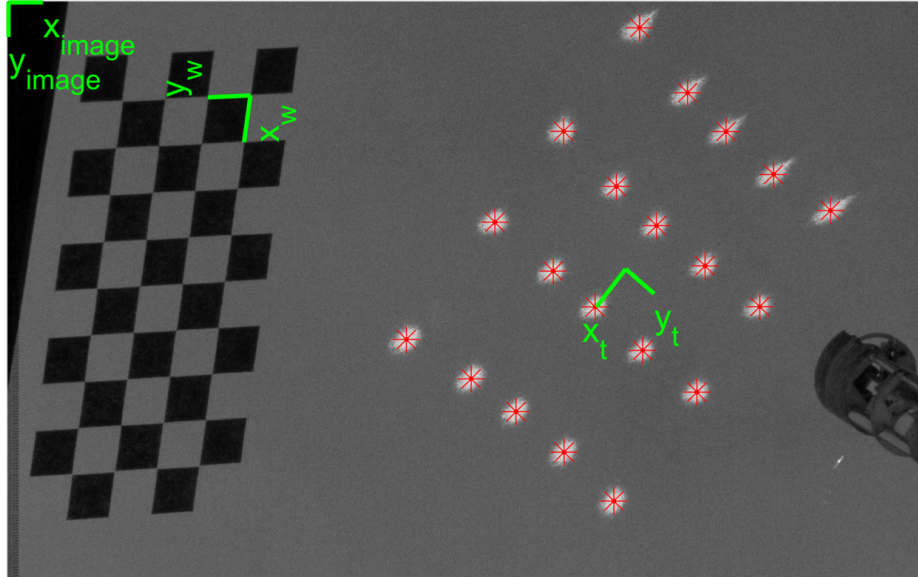


Figure 6.11: **Repeatability measurements.** Measured laser spot positions for twenty points throughout the laser workspace superimposed onto a single image. Ten such data sets were gathered were taken for a total of 200 data points.

To achieve accuracy in line with the repeatability of the device, sensory feedback will need to be incorporated. A simple approach would be to embed strain-gauge sensors within the piezoelectric bending actuators [79] to retrieve actuator position information and sense actuator current to estimate actuator velocity [58]. The mirror position could then be estimated from the transmission kinematics and the laser position from the model of specular reflection described in our prior work [61]. Measuring the mirror position directly would result in a better estimate, but the pathway to a suitable miniature sensing method is not clear. Alternatively, visual feedback could be used for high quality estimates albeit at lower sample rates than achievable with electromechanical sensors. In practice, some fusion blending these different pieces of information is likely the best approach.

Additionally, in order to be integrated with surgical lasers, suitable high-power fibers, lenses, and mirrors will need to be incorporated. The choice of components depends on the wavelength and power of the laser being used. For example, if a CO₂ laser is

being used, gold-sputtered aluminum mirrors and zinc-selenide lenses provide appropriate reflectance and transmission, respectively. Particular attention must be paid to the “laser-induced damage threshold” a measure of the laser power that an optical component can experience before degradation.

Regardless of the laser modality used, the device will need to be encapsulated so as to be robust to the fluids and debris in the surgical environment and allow for sterilization. Clear cleaning and safety protocols will need to be developed for such a complex opto-electro-mechanical device. Because the tips of laser fibers can be damaged after extended use, it may be advantageous to incorporate a method for decoupling the laser fiber from the device. This would allow the independent cleaning and cleaving of the laser fiber, which can significantly expand its lifetime [80].

This laser steering approach also enables new approaches for endoscopic visualization and visual biopsy. In optical coherence tomography and confocal endomicroscopy, laser/tissue interactions are used to visualize sub-surface structures, and scanning allows a large area of tissue to be seen at once. Optical steering can also be used to increase the effective field of view of standard white light imaging tools, through stitching together a set of images acquired through rapid scanning. The scanning system and modular device assembly approach we describe can be adapted to the fabrication of millimeter-sized versions of those systems. Even smaller versions of these systems are built using MEMs techniques [81] that use electrostatic and electrothermal actuators to excite resonant scanning elements. Our approach does not supplant these MEMs devices when absolute miniaturization is desired, but it does present advantages in terms of simplicity of construction and the ability to achieve a large quasi-static range of motion.

We also anticipate that this technology can be adapted for use in other micro-robotic systems, particularly in micro aerial vehicles and satellites for which size and weight

are at a premium [82, 83]. This technology will enable the fabrication of miniature light detection and ranging (LIDAR) sensors used for mapping and navigation [84], as well as laser scanners used for wide-area atmospheric sensing of pollution [85].

Chapter 7

Conclusion

The millimeter scale presents exciting opportunities and challenges for robotics. The challenges of manufacturing and assembly, combined with the difficulty of finding appropriate actuation schemes, makes robotics on this scale a challenge. This work lies at the intersection of those factors, contributing new approaches to millimeter-sized manufacturing and assembly, actuator design and modeling, and medical device creation. I expect that the lessons learned, techniques developed, and devices demonstrated in this work will be broadly useful for the robotics community and hopefully, in some way, the world at large.

Bibliography

- [1] J. P. Whitney, P. S. Sreetharan, K. Y. Ma, and R. J. Wood, “Pop-up book mems,” *Journal of Micromechanics and Microengineering*, vol. 21, no. 11, p. 115021, 2011.
- [2] P. S. Sreetharan, J. P. Whitney, M. D. Strauss, and R. J. Wood, “Monolithic fabrication of millimeter-scale machines,” *Journal of Micromechanics and Microengineering*, vol. 22, no. 5, p. 055027, 2012.
- [3] W. S. Trimmer, “Microrobots and micromechanical systems,” *Sensors and actuators*, vol. 19, no. 3, pp. 267–287, 1989.
- [4] A. M. Streets and Y. Huang, “Chip in a lab: Microfluidics for next generation life science research,” *Biomicrofluidics*, vol. 7, no. 1, p. 011302, 2013.
- [5] J. M. Perkel, “Life science technologies: Microfluidics—bringing new things to life science,” *Science*, vol. 322, no. 5903, pp. 975–977, 2008.
- [6] N. T. Jafferis, M. J. Smith, and R. J. Wood, “Design and manufacturing rules for maximizing the performance of polycrystalline piezoelectric bending actuators,” *Smart Materials and Structures*, vol. 24, no. 6, 2015.
- [7] N. T. Jafferis, M. Lok, N. Winey, G.-Y. Wei, and R. J. Wood, “Multilayer laminated

- piezoelectric bending actuators: design and manufacturing for optimum power density and efficiency,” *Smart Materials and Structures*, vol. 25, no. 5, p. 055033, 2016.
- [8] D. M. Aukes and R. J. Wood, “Algorithms for rapid development of inherently-manufacturable laminate devices,” in *ASME 2014 Conference on Smart Materials, Adaptive Structures and Intelligent Systems*, American Society of Mechanical Engineers Digital Collection, 2014.
- [9] T. Duerig, A. Pelton, and D. Stöckel, “An overview of nitinol medical applications,” *Materials Science and Engineering: A*, vol. 273, pp. 149–160, 1999.
- [10] D. Kapoor, “Nitinol for medical applications: A brief introduction to the properties and processing of nickel titanium shape memory alloys and their use in stents,” *Johnson Matthey Technology Review*, vol. 61, no. 1, pp. 66–76, 2017.
- [11] P. E. Dupont, J. Lock, B. Itkowitz, and E. Butler, “Design and control of concentric-tube robots,” *IEEE Transactions on Robotics*, vol. 26, no. 2, pp. 209–225, 2010.
- [12] N. Simaan, R. Taylor, and P. Flint, “A dexterous system for laryngeal surgery,” *IEEE International Conference on Robotics and Automation*, vol. 1, pp. 351–357, 2004.
- [13] R. J. Hendrick, S. D. Herrell, and R. J. Webster, “A multi-arm hand-held robotic system for transurethral laser prostate surgery,” in *Robotics and Automation (ICRA), 2014 IEEE International Conference on*, pp. 2850–2855, IEEE, 2014.
- [14] W. Sieklicki, M. Zoppi, and R. Molino, “Superelastic compliant mechanisms for needle-scope surgical wrists,” *ASME/IFTOMM International Conference on Reconfigurable Mechanisms and Robots*, pp. 392–399, 2009.
- [15] P. J. Swaney, P. A. York, H. B. Gilbert, J. Burgner-Kahrs, and R. J. Webster, “Design,

- fabrication, and testing of a needle-sized wrist for surgical instruments,” *Journal of medical devices*, vol. 11, no. 1, p. 014501, 2017.
- [16] J. Yan, T. Kaneko, K. Uchida, N. Yoshihara, and T. Kuriyagawa, “Fabricating microgrooves with varied cross-sections by electrodischarge machining,” *The International Journal of Advanced Manufacturing Technology*, vol. 50, no. 9-12, pp. 991–1002, 2010.
- [17] M. Hourmand, A. A. Sarhan, and M. Sayuti, “Micro-electrode fabrication processes for micro-edm drilling and milling: a state-of-the-art review,” *The International Journal of Advanced Manufacturing Technology*, vol. 91, no. 1-4, pp. 1023–1056, 2017.
- [18] M. H. Wu, “Fabrication of nitinol materials and components,” in *Materials Science Forum*, vol. 394, pp. 285–292, Trans Tech Publ, 2002.
- [19] K. Y. Ma, P. Chirarattananon, S. B. Fuller, and R. J. Wood, “Controlled flight of a biologically inspired, insect-scale robot,” *Science*, vol. 340, no. 6132, pp. 603–607, 2013.
- [20] N. Doshi, B. Goldberg, R. Sahai, N. Jafferis, D. Aukes, R. J. Wood, and J. A. Paulson, “Model driven design for flexure-based microrobots,” in *Intelligent Robots and Systems (IROS), 2015 IEEE/RSJ International Conference on*, pp. 4119–4126, IEEE, 2015.
- [21] Y. Zou, W. Zhang, and Z. Zhang, “Liftoff of an electromagnetically driven insect-inspired flapping-wing robot,” *IEEE Transactions on Robotics*, vol. 32, no. 5, pp. 1285–1289, 2016.
- [22] I. Misri, P. Hareesh, S. Yang, and D. DeVoe, “Microfabrication of bulk pzt transducers by dry film photolithography and micro powder blasting,” *Journal of Micromechanics and Microengineering*, vol. 22, no. 8, 2012.
- [23] A. Ghobeity, H. Getu, T. Krajac, J. Spelt, and M. Papini, “Process repeatability in

- abrasive jet micro-machining,” *Journal of materials processing technology*, vol. 190, no. 1-3, pp. 51–60, 2007.
- [24] M. Mahtabi, N. Shamsaei, and M. Mitchell, “Fatigue of nitinol: the state-of-the-art and ongoing challenges,” *journal of the mechanical behavior of biomedical materials*, vol. 50, pp. 228–254, 2015.
- [25] G. Condorelli, A. Bonaccorso, E. Smecca, E. Schäfer, G. Cantatore, and T. Tripi, “Improvement of the fatigue resistance of niti endodontic files by surface and bulk modifications,” *International endodontic journal*, vol. 43, no. 10, pp. 866–873, 2010.
- [26] R. Wood, E. Steltz, and R. Fearing, “Optimal energy density piezoelectric bending actuators,” *Sensors and Actuators A: Physical*, vol. 119, no. 2, pp. 476–488, 2005.
- [27] K.-J. Yoon, K.-H. Park, S.-K. Lee, N.-S. Goo, and H.-C. Park, “Analytical design model for a piezo-composite unimorph actuator and its verification using lightweight piezo-composite curved actuators,” *Smart Materials and Structures*, vol. 13, no. 3, p. 459, 2004.
- [28] D. L. DeVoe and A. P. Pisano, “Modeling and optimal design of piezoelectric cantilever microactuators,” *Journal of Microelectromechanical systems*, vol. 6, no. 3, pp. 266–270, 1997.
- [29] K. R. Oldham, J. S. Pulskamp, R. G. Polcawich, and M. Dubey, “Thin-film pzt lateral actuators with extended stroke,” *Journal of Microelectromechanical Systems*, vol. 17, no. 4, pp. 890–899, 2008.
- [30] R. Newnham, A. Dogan, Q. Xu, K. Onitsuka, and S. Yoshikawa, “Flexensional “moonie” actuators,” in *Ultrasonics Symposium, Proceedings.*, pp. 509–513, IEEE, 1993.

- [31] A. Dogan, K. Uchino, and R. E. Newnham, “Composite piezoelectric transducer with truncated conical endcaps ‘cymbal’,” *Ultrasonics, Ferroelectrics, and Frequency Control, IEEE Transactions on*, vol. 44, no. 3, pp. 597–605, 1997.
- [32] K. L. Poikselkä, M. Leinonen, J. Palosaari, I. Vallivaara, J. Röning, and J. Juuti, “Novel genetically optimised high-displacement piezoelectric actuator with efficient use of active material,” *Smart Materials and Structures*, 2017.
- [33] N. J. Conway, Z. J. Traina, and S.-G. Kim, “A strain amplifying piezoelectric MEMS actuator,” *Journal of Micromechanics and Microengineering*, vol. 17, no. 4, p. 781, 2007.
- [34] Y. H. Seo, D.-S. Choi, J.-H. Lee, T.-J. Je, and K.-H. Whang, “Laterally driven thin film pzt actuator with high-aspect-ratio silicon beam for stroke amplification,” *Sensors and Actuators A: Physical*, vol. 127, no. 2, pp. 302–309, 2006.
- [35] C. Technologies, “Apa30uxs,” November 2014.
- [36] D. M. Neal and H. H. Asada, “Bipolar piezoelectric buckling actuators,” *Mechatronics, IEEE/ASME Transactions on*, vol. 19, no. 1, pp. 9–19, 2014.
- [37] J. Torres and H. H. Asada, “High-gain, high transmissibility PZT displacement amplification using a rolling-contact buckling mechanism and preload compensation springs,” *IEEE Transactions on Robotics*, vol. 30, no. 4, pp. 781–791, 2014.
- [38] J. Ueda, T. W. Secord, and H. H. Asada, “Large effective-strain piezoelectric actuators using nested cellular architecture with exponential strain amplification mechanisms,” *IEEE/ASME Transactions on Mechatronics*, vol. 15, no. 5, pp. 770–782, 2010.
- [39] J. H. Kim, S. H. Kim, and Y. K. Kwak, “Development and optimization of 3-d bridge-

- type hinge mechanisms,” *Sensors and Actuators A: Physical*, vol. 116, no. 3, pp. 530–538, 2004.
- [40] T. Hensel and J. Wallaschek, “Survey of the present state of the art of piezoelectric linear motors,” *Ultrasonics*, vol. 38, no. 1, pp. 37–40, 2000.
- [41] K. Uchino, “Piezoelectric ultrasonic motors: overview,” *Smart materials and structures*, vol. 7, no. 3, p. 273, 1998.
- [42] T. Morita, “Miniature piezoelectric motors,” *Sensors and Actuators A: Physical*, vol. 103, no. 3, pp. 291–300, 2003.
- [43] J. Park, S. Keller, G. Carman, and H. Hahn, “Development of a compact displacement accumulation actuator device for both large force and large displacement,” *Sensors and Actuators A: Physical*, vol. 90, no. 3, pp. 191–202, 2001.
- [44] R. Yoshida, Y. Okamoto, and H. Okada, “Development of smooth impact drive mechanism (2nd report)-optimization of waveform of driving voltage,” *Journal-Japan Society for Precision Engineering*, vol. 68, no. 4, pp. 536–541, 2002.
- [45] D. Henderson, “Simple ceramic motor... inspiring smaller products,” *International Conference on New Actuators*, vol. 50, no. 10, 2006.
- [46] F. Mohammadi, A. Kholkin, B. Jadidian, and A. Safari, “High-displacement spiral piezoelectric actuators,” *Applied Physics Letters*, vol. 75, no. 16, pp. 2488–2490, 1999.
- [47] W. Robbins, D. Polla, T. Tamagawa, D. Glumac, and W. Tjhen, “Design of linear-motion microactuators using piezoelectric thin films,” *Journal of Micromechanics and Microengineering*, vol. 1, no. 4, p. 247, 1991.

- [48] N. T. Jafferis, E. F. Helbling, M. Karpelson, and R. J. Wood, “Untethered flight of an insect-sized flapping-wing microscale aerial vehicle,” *Nature*, vol. 570, no. 7762, p. 491, 2019.
- [49] X. Yang, Y. Chen, L. Chang, A. A. Calderón, and N. O. Pérez-Arancibia, “Bee+: A 95-mg four-winged insect-scale flying robot driven by twinned unimorph actuators,” *Robotics and Automation Letters*, 2019.
- [50] F. Claeysen, R. L. Letty, F. Barillot, and O. Sosnicki, “Amplified piezoelectric actuators: Static & dynamic applications,” *Ferroelectrics*, vol. 351, no. 1, pp. 3–14, 2007.
- [51] P. Jänker, M. Christmann, F. Hermle, T. Lorkowski, and S. Storm, “Mechatronics using piezoelectric actuators,” *Journal of the European Ceramic Society*, vol. 19, no. 6, pp. 1127–1131, 1999.
- [52] M. N. M. Zubir, B. Shirinzadeh, and Y. Tian, “Development of a novel flexure-based microgripper for high precision micro-object manipulation,” *Sensors and Actuators A: Physical*, vol. 150, no. 2, pp. 257–266, 2009.
- [53] J. Feenstra, J. Granstrom, and H. Sodano, “Energy harvesting through a backpack employing a mechanically amplified piezoelectric stack,” *Mechanical Systems and Signal Processing*, vol. 22, no. 3, pp. 721–734, 2008.
- [54] P. Liu, P. Yan, and Z. Zhang, “Design and analysis of an x–y parallel nanopositioner supporting large-stroke servomechanism,” *Proceedings of the Institution of Mechanical Engineers, Part C: Journal of Mechanical Engineering Science*, vol. 229, no. 2, pp. 364–376, 2015.
- [55] H.-J. Lee, H.-C. Kim, H.-Y. Kim, and D.-G. Gweon, “Optimal design and experiment of a three-axis out-of-plane nano positioning stage using a new compact bridge-type

- displacement amplifier,” *Review of Scientific Instruments*, vol. 84, no. 11, p. 115103, 2013.
- [56] K. Budd, S. Dey, and D. Payne, “Sol-gel processing of PbTiO_3 , PbZrO_3 , PZT, and PLZT thin films,” in *British Ceramic Proceedings*, Inst of Ceramics, 1985.
- [57] P. Muralt, “Ferroelectric thin films for micro-sensors and actuators: a review,” *Journal of micromechanics and microengineering*, vol. 10, no. 2, p. 136, 2000.
- [58] K. Jayaram, N. T. Jafferis, N. Doshi, B. Goldberg, and R. J. Wood, “Concomitant sensing and actuation for piezoelectric microrobots,” *Smart Materials and Structures*, vol. 27, no. 6, p. 065028, 2018.
- [59] H. Wei, B. Shirinzadeh, W. Li, L. Clark, J. Pinskiar, and Y. Wang, “Development of piezo-driven compliant bridge mechanisms: general analytical equations and optimization of displacement amplification,” *Micromachines*, vol. 8, no. 8, p. 238, 2017.
- [60] M. Ling, J. Cao, Z. Jiang, and J. Lin, “A semi-analytical modeling method for the static and dynamic analysis of complex compliant mechanism,” *Precision Engineering*, vol. 52, pp. 64–72, 2018.
- [61] S. A. Bothner, P. A. York, P. C. Song, and R. J. Wood, “A compact laser-steering end-effector for transoral robotic surgery,” in *IEEE International Conference on Intelligent Robots and Systems*, 2019.
- [62] R. L. Siegel, K. D. Miller, and A. Jemal, “Cancer statistics, 2018,” *CA: A Cancer Journal for Clinicians*, vol. 68, no. 1, pp. 7–30, 2018.
- [63] B. Ojo, E. M. Genden, M. S. Teng, K. Milbury, K. J. Misiukiewicz, and H. Badr, “A systematic review of head and neck cancer quality of life assessment instruments,” *Oral oncology*, vol. 48, no. 10, pp. 923–937, 2012.

- [64] A. K. Chaturvedi, E. A. Engels, R. M. Pfeiffer, *et al.*, “Human papillomavirus and rising oropharyngeal cancer incidence in the united states,” *Journal of clinical oncology*, vol. 29, no. 32, p. 4294, 2011.
- [65] D. G. Pfister, S. A. Laurie, G. S. Weinstein, *et al.*, “American society of clinical oncology clinical practice guideline for the use of larynx-preservation strategies in the treatment of laryngeal cancer,” *Journal of clinical Oncology*, vol. 24, no. 22, pp. 3693–3704, 2006.
- [66] F. C. Holsinger and R. S. Weber, “Swing of the surgical pendulum: a return to surgery for treatment of head and neck cancer in the 21st century?,” *International Journal of Radiation Oncology Biology Physics*, vol. 69, no. 2, pp. S129–S131, 2007.
- [67] M. S. Strong and G. J. Jako, “Laser surgery in the larynx early clinical experience with continuous CO2 laser,” *Annals of Otolaryngology, Rhinology & Laryngology*, vol. 81, no. 6, pp. 791–798, 1972.
- [68] M. Remacle, G. Lawson, M.-C. Nollevaux, and M. Delos, “Current state of scanning micromanipulator applications with the carbon dioxide laser,” *Annals of Otolaryngology, Rhinology & Laryngology*, vol. 117, no. 4, pp. 239–244, 2008. PMID: 18478831.
- [69] G. S. Weinstein, B. W. O’Malley Jr, and N. G. Hockstein, “Transoral robotic surgery: supraglottic laryngectomy in a canine model,” *The Laryngoscope*, vol. 115, no. 7, pp. 1315–1319, 2005.
- [70] H. Poon, C. Li, W. Gao, H. Ren, and C. M. Lim, “Evolution of robotic systems for transoral head and neck surgery,” *Oral oncology*, vol. 87, pp. 82–88, 2018.
- [71] M. Ansarin, S. Zorzi, M. A. Massaro, M. Tagliabue, M. Proh, G. Giugliano, L. Calabrese, and F. Chiesa, “Transoral robotic surgery vs transoral laser microsurgery for

- resection of supraglottic cancer: a pilot surgery,” *The International Journal of Medical Robotics and Computer Assisted Surgery*, vol. 10, no. 1, pp. 107–112, 2014.
- [72] M. Karaman, T. Gün, B. Temelkuran, E. Aynacı, C. Kaya, and A. M. Tekin, “Comparison of fiber delivered CO₂ laser and electrocautery in transoral robot assisted tongue base surgery,” *European Archives of Oto-Rhino-Laryngology*, vol. 274, no. 5, pp. 2273–2279, 2017.
- [73] M. Zhao, T. J. O. Vrieling, A. A. Kogkas, M. S. Runciman, D. S. Elson, and G. P. Mylonas, “LaryngoTORS: A novel cable-driven parallel robotic system for transoral laser phonosurgery,” *IEEE Robotics and Automation Letters*, vol. 5, no. 2, pp. 1516–1523, 2020.
- [74] A. Acemoglu, D. Pucci, and L. S. Mattos, “Design and control of a magnetic laser scanner for endoscopic microsurgeries,” *IEEE/ASME Transactions on Mechatronics*, vol. 24, no. 2, pp. 527–537, 2019.
- [75] R. Renevier, B. Tamadazte, K. Rabenorosoa, L. Tavernier, and N. Andreff, “Endoscopic laser surgery: design, modeling and control,” *IEEE/ASME Transactions on Mechatronics*, vol. 22, no. 1, pp. 99–106, 2017.
- [76] O. Ferhanoglu, M. Yildirim, K. Subramanian, and A. Ben-Yakar, “A 5-mm piezo-scanning fiber device for high speed ultrafast laser microsurgery,” *Biomedical Optics Express*, vol. 5, no. 7, pp. 2023–2036, 2014.
- [77] S. Patel, M. Rajadhyaksha, S. Kirov, Y. Li, and R. Toledo-Crow, “Endoscopic laser scalpel for head and neck cancer surgery,” in *Photonic Therapeutics and Diagnostics VIII*, vol. 8207, p. 82071S, International Society for Optics and Photonics, 2012.

- [78] N. Yamanaka, H. Yamashita, K. Masamune, T. Chiba, and T. Dohi, “An endoscope with 2 dofs steering of coaxial nd: YAG laser beam for fetal surgery,” *IEEE/ASME Transactions on Mechatronics*, vol. 15, no. 6, pp. 898–905, 2010.
- [79] S. Z. Mansour, R. J. Seethaler, Y. R. Teo, Y. K. Yong, and A. J. Fleming, “Piezoelectric bimorph actuator with integrated strain sensing electrodes,” *IEEE Sensors Journal*, vol. 18, no. 14, pp. 5812–5817, 2018.
- [80] J. M. Vasantachart, M. Lightfoot, A. Yeo, J. Maldonado, R. Li, M. Alsyof, J. Martin, M. Lee, G. Olgin, and D. D. Baldwin, “Laser fiber cleaving techniques: effects on tip morphology and power output,” *Journal of endourology*, vol. 29, no. 1, pp. 84–89, 2015.
- [81] K. Hwang, Y.-H. Seo, and K.-H. Jeong, “Microscanners for optical endomicroscopic applications,” *Micro and Nano Systems Letters*, vol. 5, no. 1, pp. 1–11, 2017.
- [82] N. T. Jafferis, E. F. Helbling, M. Karpelson, and R. J. Wood, “Untethered flight of an insect-sized flapping-wing microscale aerial vehicle,” *Nature*, vol. 570, no. 7762, pp. 491–495, 2019.
- [83] J. Puig-Suari, C. Turner, and W. Ahlgren, “Development of the standard cubesat deployer and a cubesat class picosatellite,” in *2001 IEEE Aerospace Conference Proceedings (Cat. No. 01TH8542)*, vol. 1, pp. 1–347, IEEE, 2001.
- [84] T. Mizuno, T. Kase, T. Shiina, M. Mita, N. Namiki, H. Senshu, R. Yamada, H. Noda, H. Kunimori, N. Hirata, *et al.*, “Development of the laser altimeter (lidar) for hayabusa2,” *Space Science Reviews*, vol. 208, no. 1-4, pp. 33–47, 2017.
- [85] D. Grassani, E. Tagkoudi, H. Guo, C. Herkommer, F. Yang, T. J. Kippenberg, and C.-S. Brès, “Mid infrared gas spectroscopy using efficient fiber laser driven photonic chip-based supercontinuum,” *Nature communications*, vol. 10, no. 1, pp. 1–8, 2019.